Ultra-sensitive YBCO nanoSQUIDs for the investigation of magnetic nanoparticles

Dissertation
der Mathematisch-Naturwissenschaftlichen Fakultät
der Eberhard Karls Universität Tübingen
zur Erlangung des Grades eines
Doktors der Naturwissenschaften
(Dr. rer. nat.)

vorgelegt von
Jianxin Lin
aus Longyan/ China

Tübingen
2020

Gedruckt mit Genehmigung der Mathematisch-Naturwissenschaftlichen Fakultät der Eberhard Karls Universität Tübingen.

Tag der mündl. Qualifikation:	25.08.2020
Dekan:	Prof. Dr. Wolfgang Rosenstiel
1. Berichterstatter:	Prof. Dr. Dieter Kölle
2. Berichterstatter:	Prof. Dr. Reinhold Kleiner

Abstract

Superconducting quantum interference devices (SQUIDs) are used in an impressively large variety of applications requiring sensitive detection of magnetic flux. In recent years, there has been a growing scientific and technological interest in the development of nanoSQUIDs, i.e. strongly miniaturized SQUIDs with lateral size on the sub-micrometer scale, that can be used to detect the magnetization of small spin systems like individual magnetic nanoparticles. The development of nanoSQUIDs is a major research topic at the Physics Institute - Experimental Physics II.

In this thesis, we first review the major achievements obtained so far on the development of sensitive nanoSQUIDs in Tübingen, based on Nb and $YBa_2Cu_3O_7$ (YBCO) as superconductors. This part emphasizes the advantages offered by YBCO nanoSQUIDs, fabricated on bicrystal $SrTiO_3$ (STO) substrates, regarding enhanced ranges of temperature and magnetic field, over which those nanoSQUIDs can be operated.

Regarding the application of YBCO nanoSQUIDs fabricated on STO bicrystal substrates, we have studied the occurrence of magnetic-field-driven nucleation and annihilation of magnetic vortices in individual ultrasmall ferromagnetic Co particles by YBCO nanoSQUID magnetometry. We demonstrate that the Co particles reveal bi-stable magnetization states at zero applied field, with the vortex state being the ground state. This topic is important in order to understand the thermal and temporal stability of noncollinear and other nontrivial spin textures, e.g., vortices or skyrmions, confined in ultra-

small ferromagnets.

Improving the sensitivity and long-time stability of YBCO nanoSQUIDs are in the focus of the research activities presented within this thesis.

A process for the fabrication of YBCO nanoSQUIDs on MgO bicrystal substrates has been developed. The lower dielectric permittivity of MgO, as compared to STO, offers the possibility to realize YBCO nanoSQUIDs without the need of a resistively shunting Au layer on top of the YBCO film. This in turn offers a significant increase of the characteristic voltage of the grain boundary Josephson junctions intersecting the SQUID loop, which should significantly improve the sensitivity of the nanoSQUIDs. We demonstrate that YBCO nanoSQUIDs patterned by focused Ga ion beam (Ga FIB) milling on MgO bicrystals can have non-hysteretic current voltage characteristics (IVCs) at 4.2 K even without Au as shunting layer, which shows the high potential to further improve the flux sensitivity. We further clarify the evolution of the electric transport and noise properties at 4.2 K of YBCO nanoSQUIDs on bicrystal MgO substrates, upon decreasing the thickness of the Au film used as a resistively shunting layer. Moreover, we compare the performance of YBCO nanoSQUIDs fabricated on STO and MgO bicrystals at 77 K and 4.2 K.

A new approach based on heteroepitaxially grown superlattices was implemented in order to improve the flux sensitivity of nanoSQUIDs. We report on the fabrication and characterization of nanopatterned dc SQUIDs with grain boundary Josephson junctions based on heteroepitaxially grown YBCO/STO superlattices on STO bicrys-

tal substrates. Nanopatterning is performed by Ga FIB milling. The electric transport properties and thermal white flux noise of superlattice nanoSQUIDs are comparable to single layer YBCO devices on STO bicrystals. However, we find that the superlattice nanoSQUIDs have more than an order of magnitude smaller low-frequency excess flux noise, with root-mean-square spectral density $S_\Phi^{1/2} \sim 5 - 6\,\mu\Phi_0/\sqrt{\mathrm{Hz}}$ at 1 Hz (Φ_0 is the magnetic flux quantum). We attribute this improvement to an improved microstructure at the grain boundaries forming the Josephson junctions in our YBCO nanoSQUDs.

Last but not least, we developed a novel weak link in YBCO thin films based on an artificial bottom-up technology, i.e., by using Ga FIB milling to prepare nanogrooves in single crystal STO substrates, prior to YBCO thin film growth. This technique combined with cutting edge equipment like extreme ultraviolet lithography could provide a cost-effective and reliable pathway for scaling up superconducting circuits operating at liquid-nitrogen temperature.

Kurzfassung

Supraleitende Quanteninterferenzdetektoren (SQUIDs) werden in vielfältigsten Anwendungsbereichen für die empfindliche Detektion von magnetischem Fluss eingesetzt. In den letzten Jahren hat das wissenschaftliche und technologische Interesse an der Entwicklung von nanoSQUIDs, d. h., stark miniaturisierten SQUIDs mit lateraler Größe im Submikrometerbereich, stetig zugenommen. Mit solchen nanoSQUIDs kann die Magnetisierung kleiner Spinsysteme, wie z. B. einzelner magnetischer Nanopartikel, erfasst werden. Die Entwicklung von nanoSQUIDs ist ein zentrales Forschungsthema am Physikalischen Institut - Experimentalphysik II.

In dieser Arbeit werden zunächst die wichtigsten Ergebnisse zu der in Tübingen erreichten Entwicklung empfindlicher nanoSQUIDs, aus supraleitendem Nb und $YBa_2Cu_3O_7$ (YBCO), zusammengefasst. Dieser Teil betont die Vorteile von YBCO nanoSQUIDs auf bikristallinen $SrTiO_3$ (STO) Substraten, bezüglich der erweiterten Temperatur- und Magnetfeldbereiche, in welchen diese nanoSQUIDs betrieben werden können.

Als eine Anwendung von YBCO nanoSQUIDs auf STO Bikristallsubstraten haben wir die Magnetfeldgetriebene Nukleation und Annihilation von magnetischen Vortizes in einzelnen ultrakleinen ferromagnetischen Co-Partikeln mithilfe der YBCO nanoSQUID-Magnetometrie untersucht. Wir zeigen, dass die Co-Partikel im Nullfeld bistabile Magnetisierungszustände aufweisen, wobei der Vortexzustand der Grundzustand ist. Dieses Thema ist wichtig, um die thermische und

zeitliche Stabilität nichtkollinearer und anderer nichttrivialer Spin-Texturen, z. B. Wirbel oder Skyrmionen, zu verstehen, die in ultrakleinen Ferromagneten auftreten.

Die Verbesserung der Empfindlichkeit und Langzeitstabilität von YBCO nanoSQUIDs steht im Mittelpunkt der in dieser Arbeit vorgestellten Forschungsaktivitäten.

Es wurde ein Prozess zur Herstellung von YBCO nanoSQUIDs auf MgO-Bikristallsubstraten entwickelt. Die im Vergleich zu STO geringere dielektrische Permittivität von MgO bietet die Möglichkeit, YBCO NanoSQUIDs zu realisieren, ohne dass eine resistive Au-Schicht als "Shunt" auf dem YBCO-Film erforderlich ist. Dies ermöglicht wiederum eine signifikante Erhöhung der charakteristischen Spannung der Korngrenzen-Josephson-Kontakte in der SQUID-Schleife, was die Empfindlichkeit der nanoSQUIDs signifikant verbessern sollte. Wir zeigen, dass mittels Ga-Ionenstrahlätzen (Ga FIB) strukturierte YBCO nanoSQUIDs auf MgO-Bikristallen auch ohne Au-Shunt nicht-hysteretische Strom-Spannungs-Kennlinien (IVCs) bei 4,2 K aufweisen können; dies belegt das hohe Potenzial zur weiteren Verbesserung der Flussempfindlichkeit. Weiterhin klären wir die Entwicklung der elektrischen Transport- und Rauscheigenschaften bei 4,2 K von YBCO nanoSQUIDs mit abnehmender Dicke des Au-Films als resistiver Shunt. Darüber hinaus vergleichen wir die Eigenschaften von YBCO nanoSQUIDs auf STO and MgO Bikristallen bei 77 K und 4,2 K.

Ein neuer Ansatz, der auf heteroepitaktisch gewachsenen Übergittern basiert, wurde implementiert, um die Flussempfindlichkeit von nanoSQUIDs zu ver-

bessern. Wir beschreiben die Herstellung und Charakterisierung von nanostrukturierten dc SQUIDs mit Korngrenzen-Josephson-Kontakten basierend auf heteroepitaktisch gewachsenen YBCO/STO-Übergittern auf STO-Bikristallsubstraten. Die Nanostrukturierung erfolgte mit Ga FIB-Ätzen. Die elektrischen Transporteigenschaften und das thermische weiße Flussrauschen von Übergitter-NanoSQUIDs sind vergleichbar mit einlagigen YBCO-Bauelementen auf STO-Bikristallen. Allerdings zeigt sich, dass die Übergitter-NanoSQUIDs ein um mehr als eine Größenordnung geringeres niederfrequentes Exzess-Rauschen aufweisen, mit einer effektiven spektralen Dichte $S_\Phi^{1/2} \sim 5-6\,\mu\Phi_0/\sqrt{\mathrm{Hz}}$ bei 1 Hz (Φ_0 ist das magnetische Flussquant). Wir führen diese Verbesserung auf eine verbesserte Mikrostruktur an den Korngrenzen zurück, die die Josephson-Kontakte in unseren YBCO nanoSQUDs bilden.

Und schließlich haben wir einen neuartigen Josephson-Kontakt-Typ in YBCO Dünnfilmen entwickelt. Dieser basiert auf einer künstlichen "Bottom-up" Technologie, d. h., auf dem Ga FIB-Ätzen zur Herstellung von Nanogräben in einkristallinen STO Substraten, vor dem YBCO Dünnfilm-Wachstum. Diese Technik, in Kombination mit modernster Ausstatttung wie der extremen Ultraviolettlithographie, könnte einen kostengünstigen und zuverlässigen Weg für die Skalierung von supraleitenden Schaltkreisen bieten, die bei Flüssig-Stickstoff-Temperatur betrieben werden.

List of Publications

This is a cumulative thesis based on the four publications listed below.

Publication 1 is a review article, which summarized the development, performance and application of YBCO and Nb nanoSQUIDs for the investigation of magnetization reversal of individual magnetic nanoparticles.

Publication 2 describes the investigation of magnetic vortex nucleation and annihilation in bistable ultra-small ferromagnetic Co particles by using nanoSQUID magnetometry.

Publication 3 describes the successful development of YBCO nanoSQUIDs patterned on MgO bicrystal substrates.

Publication 4 describes the realization and performance of nanoSQUIDs based on $YBa_2Cu_3O_7$ (YBCO)/ $SiTrO_3$ (STO) superlattices that are heteroepitaxially grown on STO bicrystal substrates.

Summaries and descriptions of contributions for all four publications can be found in chapter 2. The publications themselves are appended at the very end of this thesis.

Publication 1
B. Müller, **J. Lin**, J. Linek, M. Karrer, F. Limberger, L. Koch, E. Goldobin, R. Kleiner, D. Koelle, V. Morosh, T. Weimann, O. F. Kieler, J. Sesé, M. J. Martínez-Pérez
$YBa_2Cu_3O_7$ and Nb NanoSQUIDs for the Investigation of Magnetization Reversal of Individual Magnetic Nanoparticles
2019 IEEE International Superconductive Electronics Conference (ISEC) Proceedings, IEEE Xplore (2019);
DOI: 10.1109/ISEC46533.2019.8990906

Publication 2
M. J. Martínez-Pérez, B. Müller,**J. Lin**, L. A. Rodriguez, E. Snoeck, R. Kleiner, J. Sesé, and D. Koelle
Magnetic vortex nucleation and annihilation in bi-stable ultra-small ferromagnetic particles
Nanoscale **12**, 2587-2595 (2020).

Publication 3
J. Lin, B. Müller, J. Linek, M. Karrer, M. Wenzel, M. J. Martínez-Pérez, R. Kleiner, and D. Koelle
$YBa_2Cu_3O_7$ nano superconducting quantum interference devices on MgO bicrystal substrates
Nanoscale **12**, 5658-5668 (2020).

Publication 4
J. Lin, J. Linek, R. Kleiner, and D. Koelle
NanoSQUIDs from $YBa_2Cu_3O_7/SrTiO_3$ superlattices with bicrystal grain boundary Josephson junctions
Submitted to Nanoscale, July 2020; arXiv:2007.11046

Contents

1 Introduction **1**

2 Summary of publications and contributions **13**
2.1 Summary of publication 1 14
2.2 Summary of publication 2 17
2.3 Summary of publication 3 23
2.4 Summary of publication 4 38

3 Unpublished Results **49**
3.1 Comparison of single layer YBCO nanoSQUID characteristics at 4.2 K and 77 K 50
3.2 Variation of transport and noise properties of superlattice nanoSQUIDs in time 62
3.3 YBCO Josephson junctions and microSQUIDs based on Ga-FIB-induced nanogrooves in single crystal STO 67

4 Conclusion and outlook **75**

References **79**

Appended publications **95**

Chapter 1

Introduction

Within the rapidly developing field of nanoscale science and technology, nanomagnetism has emerged as a highly attractive discipline, due to intriguing basic physical phenomena, which are accompanied by a wide range of potential applications. One of the main obstacles in this field is the absence of readily available experimental methods for sensing the tiny magnetic fields of single magnetic nanoparticles (MNPs) [1–3]. Therefore, the development of such ultra-sensitive sensors with high performance at a large magnetic field is highly promising.

MNPs or single molecular magnets (SMMs) [4, 5] are characterized by a permanent magnetic moment and behave as tiny magnets or rather, giant spins. The studies on the properties of MNPs and SMMs have promoted the development of novel magnetic sensors for single particle detection with better per-

formance. Basically, in order to alter the magnetization of small spin systems, the detectors need to cope with quite high magnetic fields. At the same time, the sensitivity of the magnetic sensors should be improved in order to achieve the final goal of being able to detect the flipping of the spin of a single electron [6]. Magneto-optical techniques based on nitrogen vacancy centers in diamond [7] and the use of ferromagnetic-filled carbon nanotubes (CNTs) as spin detectors were developed in the recent few years [7–10]. Miniature magnetometers, based on either micro Hall bars [11] or micro and nano superconducting quantum interference devices (SQUIDs) [12–30] can be used as other alternatives which make the interpretation of the measurement results much more simple and direct.

Unfortunately, the field sensitivity deteriorates dramatically as the size of the Hall sensors is reduced to the submicron range. In this case, high-T_c cuprate superconducting materials could be a good option since they offer the advantages of a high critical superconducting transition temperature T_c around 90 K for $YBa_2Cu_3O_7$ (YBCO) and a high critical field, allowing the operation of nanoSQUIDs in magnetic fields up to well above 1 T.

However, obstacles are the very short superconducting coherence length in these high-T_c materials, typically 2 nm in the a–b plane and 0.2 nm along the c axis, resulting in a strong sensitivity to defects on the atomic scale [31].

Basically, there are two types of SQUIDs: the direct current (dc) [32] and the radio frequency (rf) SQUID [33]. This thesis deals exclusively with the former one, which consists of a superconducting ring in which two Josephson junctions (JJs) [34] are incorporated.

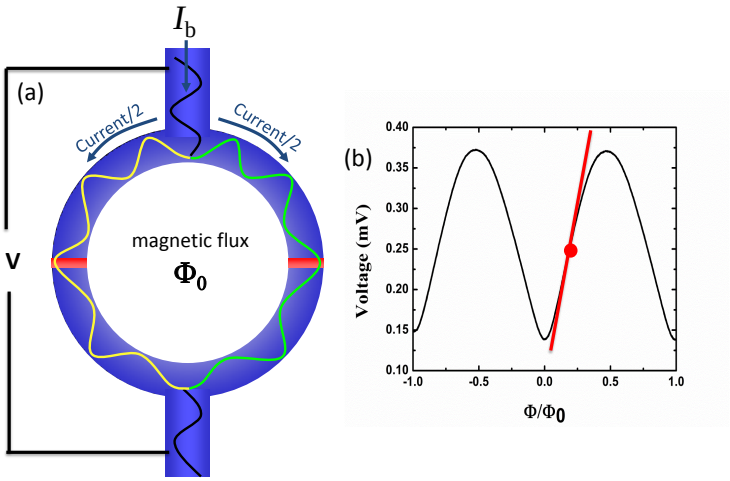

Figure 1.1: (a) schematic of dc SQUID (b) V(Φ)-characteristic of a dc SQUID. The solid red line marks the point of the steepest slope where usually is the SQUID working point. Figure adapted from Ref. [35]

The dc SQUID is sketched in Fig. 1.1(a). It combines quantization of magnetic flux in a superconducting ring and Josephson effect in superconducting weak links. The bias current (I_b) is separated into two junctions . The external magnetic field induces a circulating current (J) also contributing to the total magnetic flux in the SQUID loop. Magnetic flux coupling into

the dc SQUID loop results in a periodic response of the voltage drop V across the device with applied flux Φ, as illustrated in Fig. 1.1(b). The modulation period is one magnetic flux quantum $\Phi_0 = h/(2e) \approx 2.068\,\mathrm{Vs}$. Measurements with highest sensitivity can be performed by biasing the SQUID at the steepest slope of the $V(\Phi)$-characteristics. For typical SQUIDs, a white flux noise with a few $\mu\Phi_0/\sqrt{\mathrm{Hz}}$ can be achieved in a magnetically shielded environment [36].

As can be seen in Fig. 1.1(b), the V-Φ modulation curve and thus the SQUID output signal as a function of applied magnetic flux is nonlinear. To linearize the readout, practical SQUIDs are operated in a flux-locked loop (FLL) [37], in which a feedback loop is included to lock the SQUID at the point with the maximum slope of the V-Φ curve.

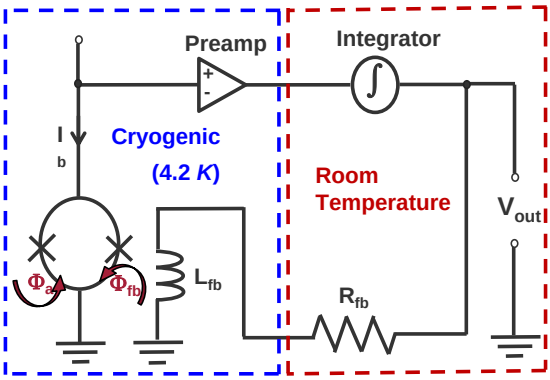

Figure 1.2: Sketch of the FLL SQUID readout circuit. An applied flux signal in the SQUID loop induces a voltage signal across the SQUID, which is amplified, integrated and fed back as a current through the feedback coil to counterbalance the applied flux.

The diagram of such a circuit is shown in Fig. 1.2. Starting from V_ϕ=max($\partial V/\partial\Phi$) , a tiny change in the flux through the SQUID loop will shift the working point away from the original position and result in a large change in the voltage across the SQUID. This voltage change is amplified and fed back as a current through a feedback coil sitting close to the SQUID. A feedback flux is induced to compensate the applied flux and bring the working point back to the original position. Thus, the voltage across the feedback resistor becomes the linearized SQUID output signal.

With respect to YBCO SQUIDs, there are various types of JJs including nanowires, bi-epitaxial, bi-crystal and step-edge grain boundary JJs (GBJJs), grooved dayem nanobridges and beam irradiation based high-T_c junctions [38–45].

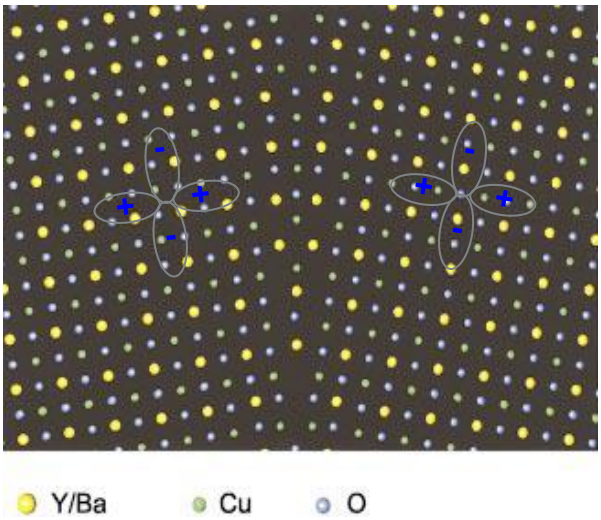

Figure 1.3: Schematic drawing of the (001) surface of a YBCO bicrystal containing a symmetric 16° [001]-tilt grain boundary in YBCO. Figure adapted from Ref. [31]. © 2002 American Physical Society.

Here, we make a brief introduction of the bicrystal technology to form GBJJs. Fig. 1.3, illustrates the (001) sur-

face of a YBCO bicrystal containing a symmetric 16° [001]-tilt grain boundary in YBCO. For weak links fabricated by epitaxial growth of a cuprate superconductor on a bicrystal substrate, the critical current density (J_c) drops exponentially [31, 46–48] with increasing angle of the grain-boundary (GB).

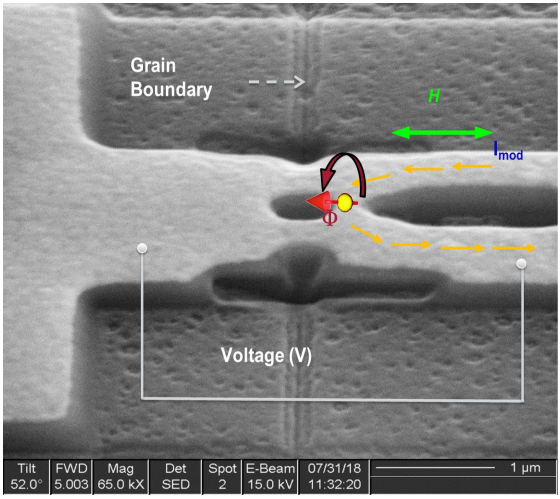

Figure 1.4: SEM image of a YBCO nanoSQUID. Figure adapted from Ref. [40]. The grain boundary runs from top to bottom of the image and intersects the SQUID hole to form two JJs. By applying a modulation current I_{mod} through the constriction (indicated as arrows in Fig. 1.4), the magnetic flux Φ can be modulated.

In our case, $SrTiO_3$ (STO) bicrystals with 24° misorienta-

tion are used to fabricate YBCO nanoSQUIDs [49]. A scanning electron microscopy (SEM) image of such a YBCO nanoSQUID is shown in Fig. 1.4, where the straight vertical line represents the position of the grain-boundary (GB).

An additional constriction is added to the layout, serving as an integrated inductance for flux feedback via a modulation current I_{mod} and as area of maximized coupling factor ϕ_μ (flux Φ coupled to the SQUID by a point-like magnetic dipole divided by the magnetic moment μ of that dipole) for a magnetic nano particle (MNP) [16]. Therefore, the spin sensitivity can be defined by $\sqrt{\mathrm{S}_\mu} = \sqrt{\mathrm{S}_\Phi}/\phi_\mu$, with units $\mu_B/\sqrt{\mathrm{Hz}}$; μ_B is the Bohr magneton. $\sqrt{\mathrm{S}_\mu}$ means the minimum magnetic moment that can be resolved per unit bandwidth. Hence, to minimize the spectral density of flux noise S_Φ while maximizing ϕ_μ is crucial in order to optimizing nanoSQUID performance.

Regarding the magnetization measurement of a MNP, the field is ramped back and forth parallel to the SQUID plane. This is indicated by the horizontal double-arrow in Fig. 1.4.

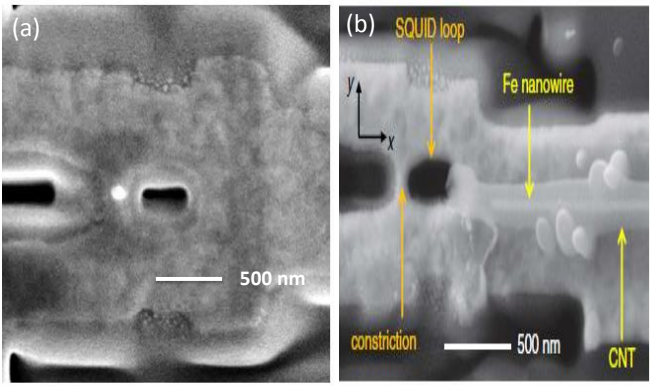

Figure 1.5: (a) Polycrystalline Co nanopillar grown by focused electron-beam-induced deposition (FEBID) on the constriction of a YBCO nanoSQUID. Figure from Ref. [50]. © 2016 IOP Publishing. (b)SEM image of a CNT-encapsulated Fe nanowire positioned close to a YBCO nanoSQUID. Figure from Ref. [3]. © American Physical Society.

We next give two examples of utilizing YBCO nanoSQUIDs to explore ultra-small magnetic nanoparticles or nanowire properties. As we can see in Fig. 1.5, polycrystalline Co nanopillars and Fe wire are located on the constriction of YBCO nanoSQUIDs and the opposite side of consitriction respectively. The Co particles are deposited by scanning a 5 keV, 25 pA focused electron beam over the area desired for the growth, while injecting $CO_2(CO)_8$ precursor gas into the vacuum chamber

[51]. During measurement, the stray field of the magnetic nanoparticles couples into the SQUID hole, allowing to record the magnetization of the object. "The magnetization reversal of an Fe nanowire encapsulated in a carbon nanotube (CNT)" [7–10] has been investigated [3].

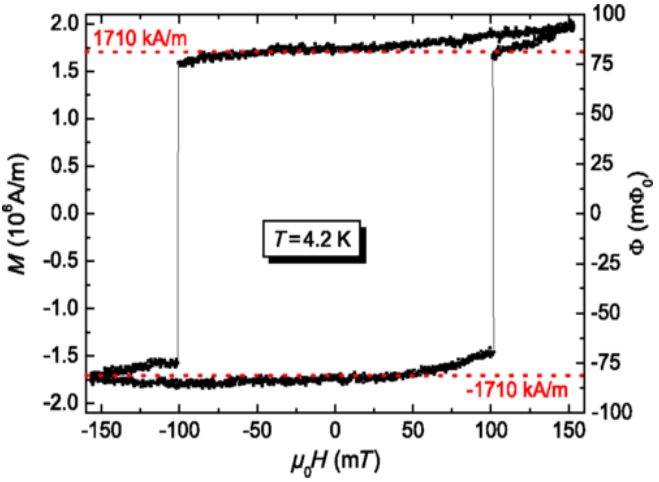

Figure 1.6: Hysteresis loop $\Phi(H)$ of the Fe nanowire detected with the YBCO nanoSQUIDs (operated in FLL dc bias mode with cutoff frequency approximately 190 kHz).Switching of the magnetization occurs at $\pm\mu_0 H_n$=101 mT.The residual field $\pm\mu_0 H_{res}$= 4.0 mT is subtracted.Left axis indicates corresponding magnetization M=Φ/ϕ_M; the dashed lines indicate the literature's value of the saturation magnetization $\pm M_s$. Figure from Ref. [3]. © American Physical Society.

Fig. 1.6 illustrates the flux signal $\Phi(H)$ detected by the YBCO nanoSQUID, while sweeping H, at a rate $\mu_0(\partial H/\partial t)$ $\approx$ 1 mT/s. At the fields $\pm\mu_0 H_n = \pm 101$ mT, abrupt changes by $\Delta\Phi \approx 150$ mΦ_0 clearly indicate magnetization reversal of the Fe nanowire [3]. The shape of the curve indicates magnetization reversal of a single-domain particle.

Chapter 2

Summary of publications and contributions

This chapter gives a summary for each of the appended publications. Each summary is followed by a description of author contributions. A significant part of the text passages and also the images with captions were taken from the 4 publications.

2.1 Summary of publication 1

YBCO and Nb NanoSQUIDs for the investigation of Magnetization Reversal of Individual Magnetic Nanoparticles (© [2019] IEEE. Reproduced from publication 1, with permission from B. Müller et al., 2019 IEEE International Superconductive Electronics Conference (ISEC) Proceedings, IEEE Xplore 2019)

This publication is a review article, in which an overview of the nanoSQUID activities within the group in Tübingen is given. We report on the fabrication, performance and application of sensitive $YBa_2Cu_3O_7$ (YBCO) and Nb nanoSQUIDs to magnetization reversal measurements of individual magnetic nanoparticles. The YBCO SQUIDs are based on grain boundary Josephson junctions and are patterned in a single layer of epitaxially grown YBCO films by Ga focused ion beam milling. The Nb SQUIDs contain sandwich-type Josephson junctions with normal conducting HfTi barriers; they are fabricated with a multilayer technology that includes patterning by e-beam lithography and a combination of milling techniques and chemical-mechanical polishing.

The YBCO and Nb nanoSQUIDs have nonhysteretic current-voltage characteristics (IVCs) at temperature T=4.2 K that are reasonably well described by the resistively and capacitively shunted junction model. Due to the small inductance L of the SQUID loop (in the pH range), the rms flux noise in the thermal white noise region $S_\Phi^{1/2}$ is very low – typically

a few $0.1\,\mu\Phi_0/\sqrt{\text{Hz}}$ (Φ_0 is the magnetic flux quantum). The lowest values obtained so far are $S_\Phi^{1/2}$=$0.045\,\mu\Phi_0/\sqrt{\text{Hz}}$ [3] and $0.11\,\mu\Phi_0/\sqrt{\text{Hz}}$ [16] for our best YBCO and Nb nanoSQUIDs, respectively.

The YBCO nanoSQUIDs offer the advantage of operation over a very wide temperature range, so far from 300 mK up to 80 K [50]. Moreover, due to the huge upper critical field of YBCO, these devices offer the potential for operation up to very strong magnetic fields. So far, we operated devices at 4.2 K up to 3 T, and performed flux noise measurements up to 1 T [52]. The temperature range of operation of the Nb nanoSQUIDs is much more restricted, as compared to the YBCO nanoSQUIDs. Typically our devices operate below 6 K.

Regarding application, we have used YBCO and Nb nanoSQUIDs to perform magnetization reversal measurements of individual magnetic nanoparticles (MNPs) of different geometries: nanopillars, -disks, -wires and -tubes. We have demonstrated the benefit of using YBCO nanoSQUIDs for MNP measurements over a wide temperature range from 300 mK up to 80 K [50]. Nb nanoSQUIDs have been integrated into the torque magnetometer setup of the Poggio group at Univ. Basel to investigate individual Ni, permalloy and CoFeB nanotubes. Combined torque and SQUID measurements on individual Ni nanotubes, supported by micromagnetic simulations of magnetization configurations, suggest reversal via the formation of vortexlike states within the nanotube. Such stray-field free states can have applications for memory and noninvasive sensing.

In summary,YBCO and Nb nanoSQUIDs have been devel-

oped for the investigation of magnetization reversal of individual magnetic nanoparticles. Very small SQUID inductances enable the realization of ultralow flux noise of the nanoSQUIDs in the thermal white noise limit. For MNPs placed in 10 nm distance to the SQUID loop, this translates into spin sensitivities down to only a few Bohr magnetons per unit bandwidth, which is appropriate for many studies on individual MNPs. Apart from further suppression of $1/f$ noise, a key challenge is the development of reliable routines for placing MNPs in a controlled way in close vicinity to the nanoSQUIDs, ideally at variable position and temperature. For YBCO nanoSQUIDs, the recently developed creation of Josephson junctions and SQUIDs by focused He ion irradiation [41, 42] can provide new perspectives for creating advanced nanoscale devices.

This publication summarizes work that was done in collaboration with V. Morosh, T. Weimann and O. F. Kieler from the Physikalisch-Technische Bundesanstalt in Braunschweig, where the Nb nanoSQUIDs were fabricated, and M. J. Martínez-Pérez and J. Sesé from the Aragón Materials Science Institute (Spanish National Research Council and University of Zaragoza), where the deposition of Co nanoparticles and parts of the measurements were done. Benedikt Müller, Max Karrer, Julian Linek and myself contributed to the ideas, sample fabrication, measurements and data analysis on YBCO nanoSQUIDs. Further, I wrote parts of the manuscript.

2.2 Summary of publication 2

Magnetic vortex nucleation and annihilation in bi-stable ultra-small ferromagnetic particles (Reproduced from publication 2 with permission from the Royal Society of Chemistry.)

Publication 2 illustrates the application of YBCO nanoSQUIDs to explore the properties of ultra-small ferromagnetic particles. Cobalt nanoparticles with their size less than 100 nm grown by means of Focused Electron Beam Induced Deposition (FEBID) [53, 54] are explored. Three cobalt nanoparticles (labeled Disc1, Disc2 and Disc3) have been deposited directly on the surface of the three YBCO nanoSQUIDs (SQ1, SQ2 and SQ3).

We studied the vortex-mediated magnetization reversal in individual ultra-small ferromagnetic particles at low temperatures . We confirmed that at zero applied bias field, the flux-closure magnetic state (vortex) and the quasi uniform configuration are bi-stable

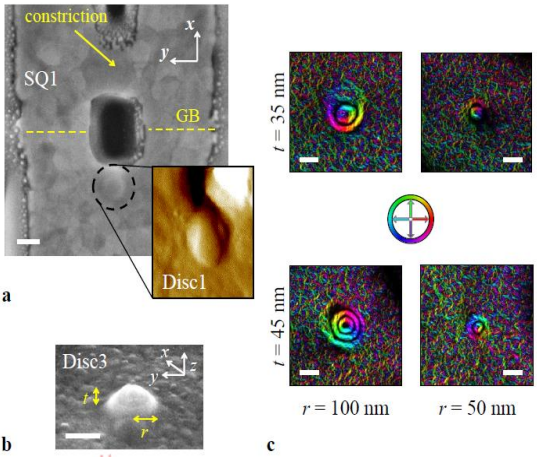

Figure 2.1: a. SEM image of Disc1 deposited on SQ1. The dashed circle highlights the position of the nanoparticle whereas dashed lines indicate the grain boundary (GB). The inset shows the corresponding AFM image of the particle. b. SEM image of Disc3 approximated to a semi-sphere with semi-*a*xis (r; r; t). c. Electron holography images of few representative cobalt nanoparticles showing the presence of flux-closure ground states. The color scale in the middle represents the direction of the magnetic flux. Scale bar is 100 nm in all panels. Figure from appended publication 2. © 2020 The Royal Society of Chemistry.

Disc3 (Fig. 2.1b) is deposited at the constriction where the coupling to the nanoSQUID is maximized. Disc1 and Disc2 are deposited on the opposite side of the nanoloop. A SEM and an Atomic Force Microscopy (AFM) image corresponding to Disc1 can be seen in Fig. 2.1(a). We highlight that Disc1 is fabricated

under the same growth conditions and is, therefore, nominally identical to the particle shown in the upper right panel of Fig. 2.1(c). The external magnetic field is applied along the x direction. r and t are estimated from the SEM and AFM measurements [50]. Fig. 2.1(c) shows flux closure states, that have been imaged by electron holography at room temperature.

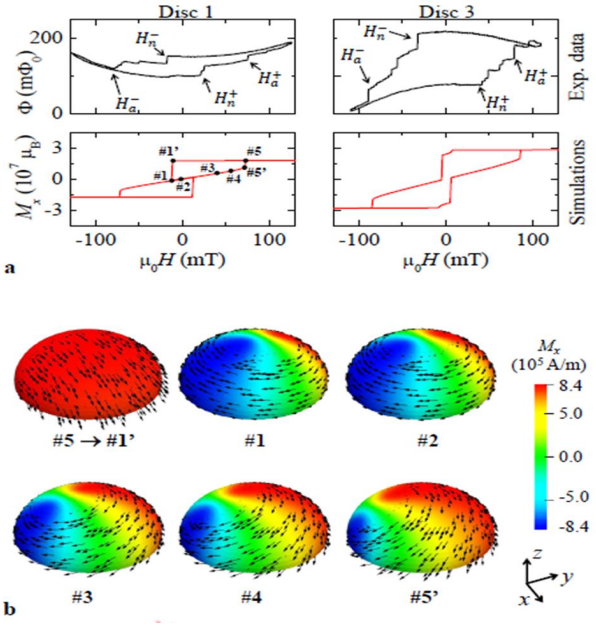

Figure 2.2: Hysteresis loops of Co particles. a: (top) Typical experimental hysteresis loops F(H) measured at $T = 10\ K$ and (bottom) numerical simulations $M_x(H)$ for Disc1 and Disc3. Top panels also show the definitions for the nucleation and annihilation fields. b: Numerically simulated spatially-resolved magnetization for Disc1 at selected applied fields as indicated in panel a (bottom left). Color coding represents the magnetization along x (direction of the applied field) whereas arrows indicate the magnetization direction. Figure from appended publication 2. © 2020 The Royal Society of Chemistry.

Hysteresis curves $\Phi(H)$ are obtained by sweeping the external bias magnetic field H and measuring the flux Φ threading the SQUID nanoloop. Two typical hysteresis curves obtained at T=10 K for Disc1 and Disc3 can be seen in Fig. 2.2(a) (top panels).

Here, we plot the magnetic flux coupled to the nanoSQUIDs in units of the flux quantum Φ_0. The apparent curvature (positive for Disc1 and negative for Disc3) is still under investigation. A similar phenomenon is observed in all devices studied so far and is attributed to the non-perfect alignment of the external magnetic field with respect to the Josephson junction's plane.

In Fig. 2.2(b), we plot a few numerically simulated spatially resolved magnetization maps at selected field values numbered in panel a (bottom left). At large positive magnetic fields the cobalt nanoparticle is in the quasi-single domain (QSD) ground state (#5 in Fig. 2.2). If we decrease the field reaching the nucleation field (#1), the energy barrier for vortex nucleation (U_{n}) becomes zero and the magnetic vortex nucleates (#1'). If we now increase again the magnetic field, the vortex core will move along the y direction as shown in the series #1→#2→#3 in Fig. 2.2(b).

This translates into an increase of U_{n} – i.e., remove parentheses while the energy barrier for annihilation (U_{a}) decreases steadily up to the point at which the QSD and vortex state (VS) [55] are degenerate. If we continue increasing the magnetic field, the particle will remain "trapped" in the metastable VS. Once the annihilation field is reached at #5', the energy barrier for vortex annihilation (U_{a}) will equal zero so that the transition into the QSD state will take place (#5).

In summary, we have studied the occurrence of field-driven vortex nucleation and annihilation [56–58] in individual ultra-small ferromagnetic Co particles by YBCO nanoSQUID magnetometry. We demonstrate that particles are bi-stable at zero applied field, with the vortex state being the ground state. This topic is important in order to understand the thermal and temporal stability of noncollinear and other nontrivial spin textures, e.g., vortices or skyrmions, confined in ultra-small ferromagnets. Controlling and manipulating magnetic units below the 100 nm range is paramount for their integration into nanoscopic spintronic and magnonic devices [59–61].

This work was done in collaboration with M. J. Martínez-Pérez and J. Sesé from the Aragón Materials Science Institute (Spanish National Research Council and University of Zaragoza), and L. A. Rodriguez and E. Snoeck from the Center for Materials Elaboration and Structural Studies in Toulouse. I assisted in the fabrication and pre-patterning of the YBCO films. Benedikt Müller fabricated and prepatterned the YBCO films and assisted in the fabrication of the SQUIDs and building of the measurement setup. Benedikt Müller also performed the AFM measurements and the simulations for calculation of the coupling factors. Further, I assisted in SQUID measurements, data analysis and preparation of the manuscript.

2.3 Summary of publication 3

YBCO superconducting quantum interference devices on MgO bicrystal substrates (Reproduced from publication 3 with permission from the Royal Society of Chemistry.)

YBCO NanoSQUIDs [26, 50, 52, 62] are typically fabricated by epitaxial YBCO film growth on STO bicrystal substrates with a [001]-tilt GB and 24° misorientation angle, and are covered in-situ with an Au layer (with thickness d_{Au}) as a resistively shunting layer in order to obtain non-hysteretic IVCs at 4.2 K. However, the extra Au layer restrains the further improvement of intrinsic flux noise , because the resistive shunt reduces the characteristic voltage of the JJs and hence increases the flux noise [16].

The hysteresis in the IVCs of unshunted YBCO GBJJs on STO at 4.2 K has been attributed to the significant contribution of stray capacitance from the STO substrate due to its very high dielectric permittivity ε [63]. Fig. 2.3(a) shows an IVC of a YBCO nanoSQUID on a STO bicrystal without Au as shunting layer with flux bias adjusted to achieve maximum critical current $I_{c;max}$. Clearly, the IVC shows hysteristic behavior. The hysteresis in the IVC leads also to hysteresis and to switching steps in the $V(\Phi)$ curves, as shown in Fig. 2.3(b). Obviously, one has to avoid such a hysteretic behavior, if one wants to use the conventional SQUID readout.

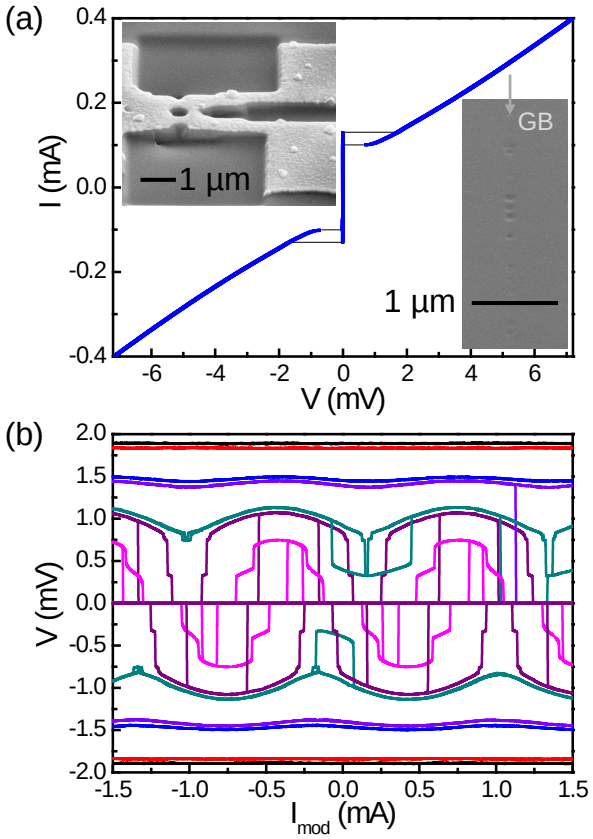

Figure 2.3: Transport characteristics of SQUID S1 (on STO) with d_{Au}=0. (a) Hysteristic IVCs; I_{mod} was adjusted to obtain maximum critical current. Upper left inset: SEM image of the SQUID after FIB milling. Lower right inset: SEM image of nano defects aligned along the GB in STO bicrystal substrate at a location where YBCO has been removed by Ar ion milling. (b) V(I_{mod}) curves, measured with different bias currents. Figure from appended publication 3. © 2020 The Royal Society of Chemistry.

Therefore, it seems to be highly promsing to use an alternative bicrystal substrate material with lower dielectric constant. If such a material also comes with smaller microwave losses than in STO, its use could also be promising for microwave applications. In the following, we show the potential to improve the flux sensitivity by replacing the STO substrate by bicrystal MgO.

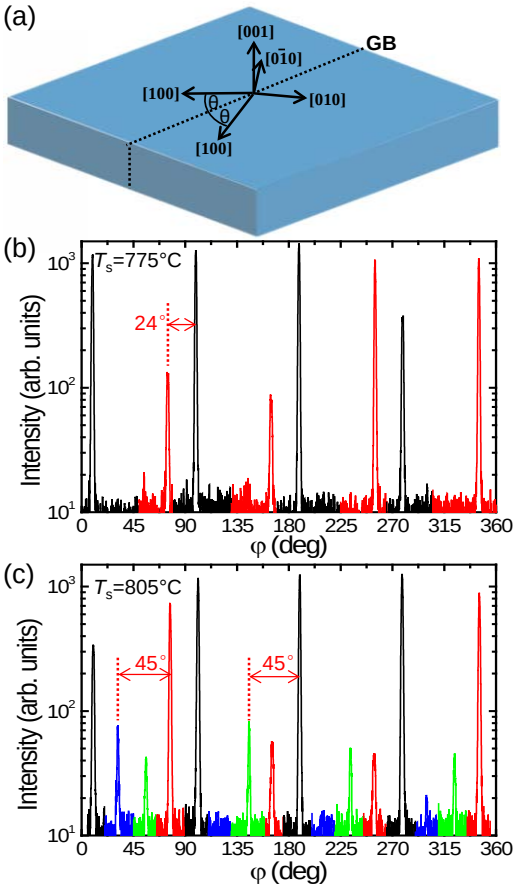

Figure 2.4: On the orientation of YBCO films grown epitaxially on MgO bicrystal substrates: (a) Schematic view of the symmetric [001]-tilt MgO bicrystal substrate with crystallographic orientations. (b) and (c) YBCO (103) plane XRD φ-scans for films deposited at different substrate temperature (T_s). Figure from publication 3. © 2020 The Royal Society of Chemistry.

MgO has a large 9% lattice mismatch with YBCO. Various studies revealed the appearance of 45° in-plane misoriented YBCO grains, depending on surface topology and surface contamination [64–66]. Such an in-plane misorientation can cause a significantly reduced critical current density of the YBCO films and the deterioration of SQUID performance. In order to confirm the in-plane orientation of the YBCO film, YBCO (103) plane X-ray diffraction (XRD) φ-scans were taken.

Fig. 2.4(b) and (c) shows such φ-scans for YBCO films deposited at a substrate temperature T_s = 775°C and 805°C, respectively, by pulsed laser deposition (PLD). For the film deposited at T_s = 775°C [Fig. 2.4(b)], the XRD data yield peaks at 0° ± (θ), 90° ± (θ), 180° ± (θ) and 360° ± (θ), reflecting the fourfold symmetry of the crystal lattice and rotation of the crystallographic axes by ± θ across the GB (see Fig. 2.4(a)). This result shows that YBCO grows in single in-plane orientation with YBCO[100]//MgO[100] on both grains. For comparison, the YBCO film grown at T_s = 805°C [Fig. 2.4(c)] yields additional peaks in the XRD φ-scans that are displaced by 45°. This indicates that at slightly higher T_s a mixed in-plane orientation with 45° grain boundaries appears, i.e., some grains also have the epitaxial relation YBCO[100]//MgO[110]. These results show that with optimized deposition parameters, we can grow *c*-axis oriented YBCO films with single inplane orientation also on MgO bicrystals. For details of the growth process of our YBCO thin films on STO and of their structural and electric transport properties see e.g. Refs. [52, 67, 68].

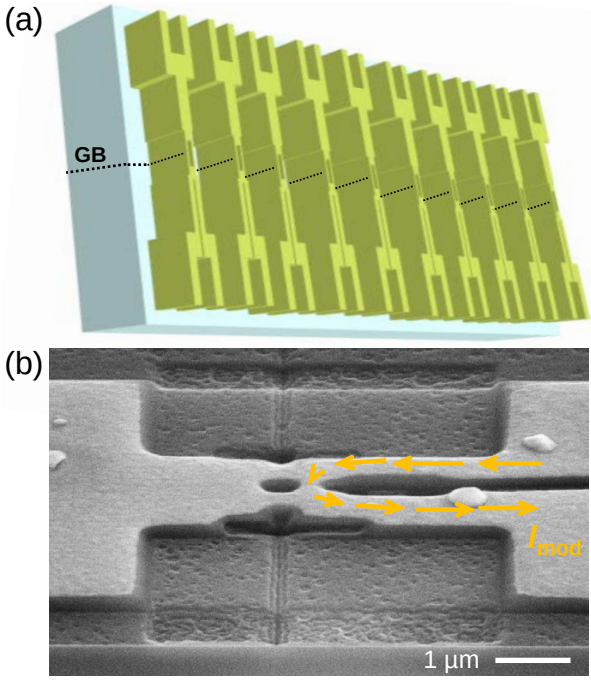

Figure 2.5: (a) Schematic view of the chip layout. (b) SEM image of a YBCO nanoSQUID covered with 65 nm Au on a MgO bicrystal substrate. The arrows indicate the flow of the modulation current. Figure from appended publication 3. © 2020 The Royal Society of Chemistry.

For the fabrication of YBCO nanoSQUIDs on bicrystal MgO, we first grow by PLD epitaxial YBCO films on MgO bicrystal

substrates with 24 ° misorientation angle. The *c*-axis-oriented YBCO films with single inplane orientation on both halfs of the bicrystal substrates have a thickness of 120 nm. After YBCO deposition, a $d_{Au} = 65$ nm thick Au film is deposited by electron-beam evaporation in-situ. For the definition of coarse structures we use photolithography, followed by Ar ion milling (with 300 eV beam energy) to pattern 16 microbridges with 8 μm width as shown in Fig. 2.5 (a), which are straddling the GB, i.e., forming wide JJs. Subsequently, single selected microbridges are patterned into nanoSQUIDs as illustrated in Fig. 2.5 (b) by a focused ion beam (FIB) with 30 keV Ga ions in a dual beam FIB system. [69, 70] The size of the SQUID hole is 220 nm $\times$ 380 nm, the widths of the two GBJJs intersecting the SQUID loop are $W_{J1} = 260$ nm and $W_{J2} = 280$ nm and their length is $L_J = 380$ nm. Furthermore, we use the Ga FIB to cut a slit perpendicular to the GB (from the right in Fig. 2.5) towards the grain-boundary (GB).

With this process step, we define a constriction of width W_c and length L_c in the SQUID loop. By applying a modulation current I_{mod} through this constriction (indicated as arrows in Fig. 2.5(b)), we can modulate the magnetic flux in the SQUID, to ensure operation at the optimum flux bias point and to enable SQUID readout in a flux-locked loop (FLL) [37].

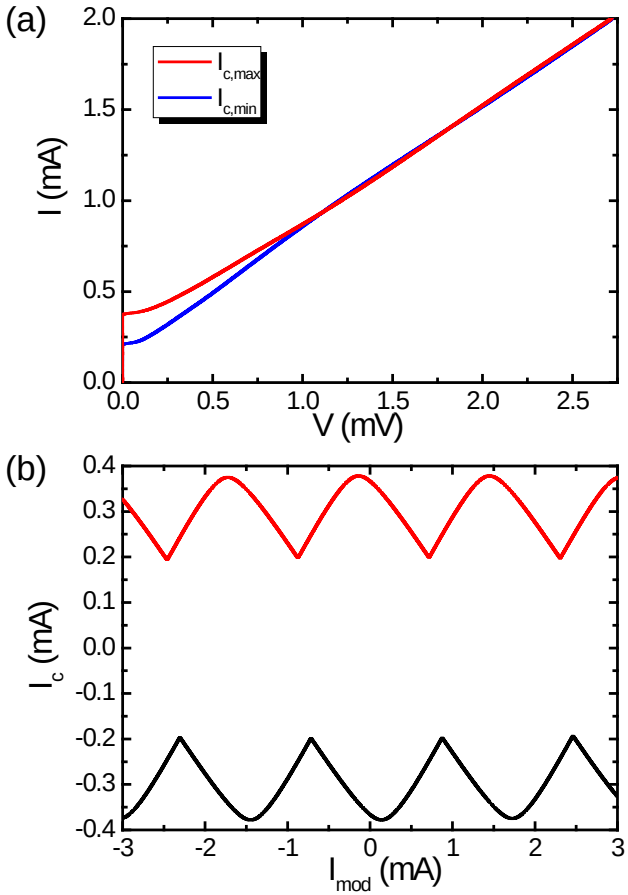

Figure 2.6: Transport characteristics of SQUID 5 (on MgO) with d_{Au} = 65 nm. (a) Non-hysteretic IVCs measured with two values for I_{mod} to obtain maximum and minimum critical current. (b) Critical current I_{c} vs I_{mod} for both bias current polarities. Figure from appended publication 3. © 2020 The Royal Society of Chemistry.

In the following, we present data for four YBCO nanoSQUIDs that have been fabricated on the same MgO bicrystal substrate. Fig. 2.6(a) shows two nonhysteretic IVCs for SQUID 5, with flux bias adjusted to achieve maximum and minimum I_c. Fig. 2.6(b) shows the modulation of the critical current $I_c(I_{mod})$ for SQUID 5. The value of $V_c = 0.57\,\mathrm{mV}$, which we find for this shunted YBCO nanoSQUID on MgO, is well within the range of V_c values that have been obtained for shunted YBCO nanoSQUIDs of comparable geometry and size on STO bicrystals covered with Au [49]. We note that prior to FIB patternig, the device ($8\,\mu$m wide GBJJ) had even a slightly smaller $V_c = 0.50\,\mathrm{mV}$. Moreoever, SQUID 5 has $I_{c;max} = 378\,\mu\mathrm{A}$, corresponding to $j_c = 5.8{\times}10^5\mathrm{A/cm^2}$. The enhanced j_c after FIB nanopatterning is due to the transition from a wide junction with nonhomogeneous current distribution to a short junction with homogeneous current distribution.

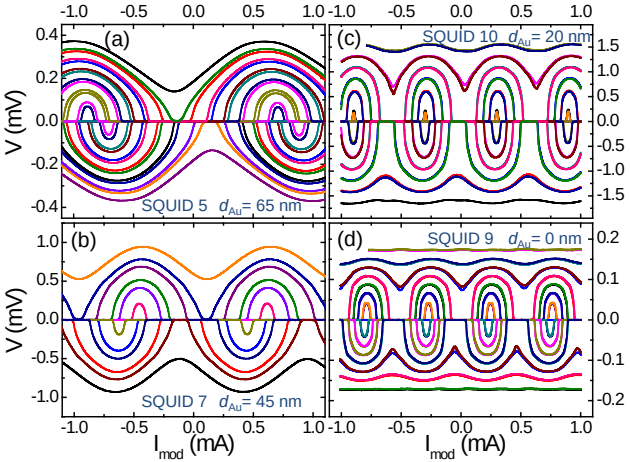

Figure 2.7: $V(I_{\mathrm{mod}})$ oscillations, measured with different bias currents for SQUIDs on MgO (chip 1). With decreasing d_{Au}, the oscillation period is decreasing, i.e., M is increasing. Figure from publication 3. © 2020 The Royal Society of Chemistry.

In order to check the performance of YBCO nanoSQUIDs on bicrystal MgO with decreasing Au thickness, $V(I_{\mathrm{mod}})$ SQUID oscillations (at different I_{b}) of the four YBCO nanoSQUIDs on the same MgO bicrystal substrate (chip 1), with d_{Au} ranging from 65 nm to 0 were measured. To produce nanoSQUIDs with reduced Au layer thickness, we used Ar ion milling to remove Au partially or fully on top of the junctions, prior to Ga FIB nanopatterning the SQUIDs. All four devices show non-hysteretic IVCs and continous $V(I_{\mathrm{mod}})$ oscillations, including

SQUID 9, for which Au has been completely milled away, as shown in Fig. 2.7 (in contrast to SQUID S1 on the STO bicrystal discussed above, which shows hysteretic IVCs).

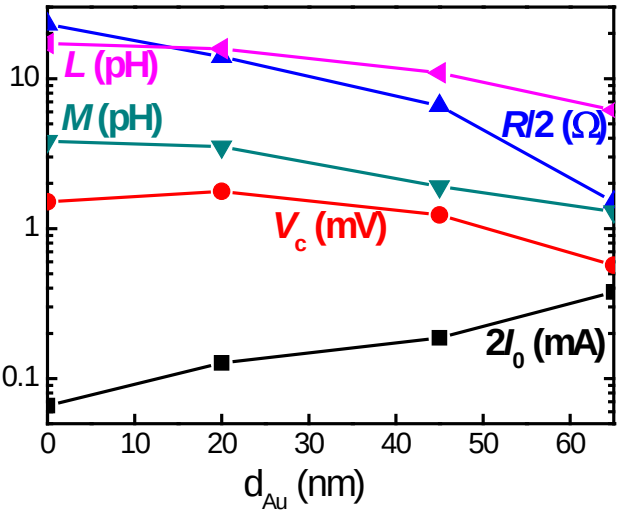

Figure 2.8: Variation of SQUID parameters with Au layer thickness for SQUIDs on MgO (chip 1). Figure from appended publication 3. © 2020 The Royal Society of Chemistry.

As expected, the resistance of the nanoSQUIDs increases strongly (by a factor of 15) upon decreasing d_{Au}. For d_{Au} =0 (SQUID 9) the value R/2=23 Ω is quite comparable to R/2 =22 Ω for SQUID S1 on STO. Unfortunately, the envisioned

improvement of SQUID performance via increasing R is counterbalanced by a concomitant decrease in I_0 (by a factor of 6). Still, V_c increases slightly upon reducing d_{Au}, but only by a factor of 2 to 3. Moreover, with decreasing d_{Au} we find an increase in the SQUID inductance L and the mutual inductance M (by a factor of 3). This increase in inductances indicates a degradation of not only the GBJJs but also of the entire YBCO film forming the SQUID loop. Most likely, this can be attributed to oxygen loss of YBCO during Ar ion milling [71] caused by heating.

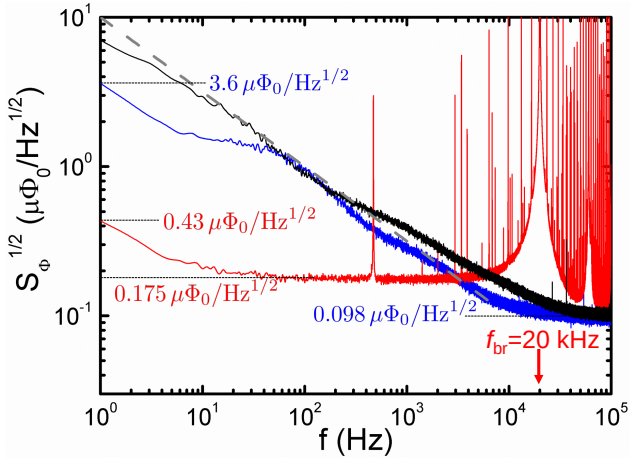

Figure 2.9: Rms spectral density of flux noise $S_\Phi^{1/2}(f)$ measured in FLL mode on SQUID 5 with dc bias (blue) and bias reversal (red) and on SQUID 4 with dc bias (black), both on MgO with $d_{\mathrm{Au}} = 65\,\mathrm{nm}$. The vertical arrow indicates the bias reversal frequency f_{br}. Figure from appended publication 3. © 2020 The Royal Society of Chemistry.

To further characterize the performance of the shunted SQUID, we measured its intrinsic flux noise. Fig. 2.9 shows the rms spectral density of flux noise$S_\Phi^{1/2}(f)$ measured in FLL mode. The blue curve has been measured with dc bias and yields ultra-low thermal white noise $S_\Phi^{1/2} = 0.098\,\mu\Phi_0/\sqrt{\mathrm{Hz}}$, which is the second lowest value we ever measured for a high-T_c nanoSQUID. For frequencies $f \leq 10\,\mathrm{kHz}$, the flux noise increases with decreasing f. For comparison, the dashed lines shows the ubiquitous

$1/f$ noise, i.e., $S \propto 1/f$, which is typically observed for SQUIDs at low frequency. It is well known that the dominant source of $1/f$ noise comes from I_0 fluctations in the JJs due to localized defects in the JJ barrier, and that this is particularly strong for high-T_c SQUIDs [72].

Very roughly, the blue curve follows the $1/f$ noise scaling; however clear deviations (in particular the bump-like feature around 100 Hz) are visible. This is probably not surprising, as only few defects may be present in the small (submicron-sized) JJs, which results in a superposition of a small number of Lorentzians [3]. More surprising is the fact, that the overall level of this low-frequency excess noise is more than an order of magnitude lower than what we typically observe for our YBCO nanoSQUIDs on STO bicrystals.

In summary, we have sucessfully developed a process for the fabrication of YBCO nanoSQUIDs on MgO bicrystal substrates. High-quality YBCO films can be grown expitaxially with single in-plane orientation on each of the two halfs of the substrate. With proper grounding, charging effects during Ga FIB milling can be avoided, which enables nanopatterning of devices with high spatial resolution. We demonstrate the potential of substantially lowering the flux noise by replacing the STO substrate with bicrystal MgO, which has orders of magnitude smaller dielectric permittivity than STO; i.e., one may avoid Au as a resistively shunting layer to reduce the intrinsic white noise of the nanoSQUIDs. Meanwhile, the evolution of YBCO nanoSQUIDs with the decreasing of Au thickness was clarified.

This work was done in collaboration with M. J. Martínez-Pérez from the Aragón Materials Science Institute (Spanish Na-

tional Research Council and University of Zaragoza). I did the fabrication and patterning of all devices, with partial support from Malte Wenzel. Futher,I did all measurements. Noise measurement were done with the help of Julian Linek. Benedikt Müller and Max Karrer gave me support regarding equipment operation. I also wrote most parts of the manuscript.

2.4 Summary of publication 4

Nano SQUIDs from $YBa_2Cu_3O_7/SrTiO_3$ superlattices with bicrystal grain boundary Josephson junctions

A significant drawback for high-T_c cuprate SQUIDs in general is the very large amount of low-frequceny excess noise, typically scaling with frequency f as $S_\Phi \propto 1/f$ ($1/f$ noise) [72]. The dominant source of $1/f$ noise comes from critical current I_0 fluctations due to localized defects in the JJ barrier [73], which can be several orders of magnitude larger than for conventional Nb tunnel junctions [74–76].

For YBCO nanoSQUIDs with ultralow thermal white noise, this excess noise can dominate the spectral density of flux noise up to high frequencies in the MHz range [3, 77]. An established procedure to suppress this $1/f$ noise contribution from I_0 fluctuations in dc SQUIDs is the application of bias reversal schemes (including proper modulation of flux bias), which suppresses $1/f$ noise below the applied bias reversal frequency f_{br} [78].

However, applying such schemes to YBCO nanoSQUIDs is a particular challenge for the SQUID readout electronics and nanoSQUID design, because very large f_{br} is required, and the required modulation of the flux bias points at f_{br} is difficult to achieve due to the small SQUID inductance L and concomitantly small mutual inductance M between nanoSQUID and the flux modulation line.

We further note that the flux noise spectrum of YBCO nanoSQUIDs often shows a superposition of a few Lorentzians

rather than a pure $1/f$ spectrum, which can be explained by the relatively small number of dominating defects in JJs with small size [3, 77].

Obviously, the strong low-frequency excess noise in YBCO nanoSQUIDs based on GBJJs has to be related to the defect structure in the GB barrier. Apart from optimizing thin film growth by introducing suitable buffer or cap layers [39, 79, 80], a possible solution to this problem may be the growth of multilayers (superlattices), involving epitaxially grown interlayers between YBCO films [81], to interrupt the growth of extended defects in YBCO.

Such a multilayer or superlattice approach has been successfully used to significantly enhance the critical current density in YBCO films[82–85], in particular for thick films developed for high-current applications.

However, so far, there is no information on the possible modification (improvement or deterioration) of $1/f$ noise from I_0 fluctuations in YBCO JJs and SQUIDs based on them, induced by the implementation of superlattice structures into the devices.

In this work, we report on the fabrication and properties of YBCO nanoSQUIDs that are based on a heteroepitaxial YBCO/STO superlattice, grown on a STO bicrystal substrate. The comparison with single layer YBCO devices of similar geometry shows, that the superlattice nanoSQUIDs yield comparable electric transport properties and comparable upper bounds to the flux noise in the thermal white noise limit. Regarding low-frequency excess noise, however, we find a strong reduction of the low-frequency noise in the superlattice nanoSQUIDs by

more than one order of magnitude in rms flux noise at 1 Hz.

We used PLD to grow an epitaxial YBCO/STO superlattice on a STO bicrystal substrate with a symmetric ($\pm 12°$) [001]-tilt grain boundary (GB), i.e., with a misorientation angle $2\theta = 24°$ ($\theta = 12°$). The multilayer consists of a stack of four c-axis oriented YBCO layers with $d_Y \approx 30\,\mathrm{nm}$ thickness per layer, separated by three STO interlayers with 3 nm thickness per layer. An in-situ evaporated 65-nm-thick Au layer on top of the YBCO/STO superlattice serves as a resistive shunt to provide nonhysteretic current-voltage characteristics (IVCs) of the grain boundary junctions formed in YBCO and as a protection layer during Ga focused ion beam (FIB) nanopatterning [40, 49].

Fig. 2.10 shows scanning electron microscopy (SEM) images of two YBCO/STO multilayer nanoSQUIDs SQ-14 and SQ-15, nanopatterned into JJ-14 and JJ-15, respectively. At the position where the GB crosses the microbridge, the Ga FIB is used to define two sub-μm-wide GBJJs with width $w_{\mathrm{J}i}$ ($i = 1, 2$) and to mill the SQUID hole with size $\sim \ell_\mathrm{J} \times \ell_\mathrm{c}$. In addition, we use the Ga FIB to cut a slit perpendicular to the GB (from the right in Fig. 2.10) towards the GB, to produce a constriction with width w_c in the SQUID loop. By applying a modulation current I_mod (indicated as arrows in Fig. 2.10) through the constriction, the magnetic flux Φ in the SQUID can be modulated, to ensure SQUID operation at optimum flux bias and to perform SQUID readout in a flux-locked loop (FLL). For measurements of magnetization reversal of individual MNPs, placing the MNP on top of the constriction also provides optimum coupling of signal to the nanoSQUID [16, 50].

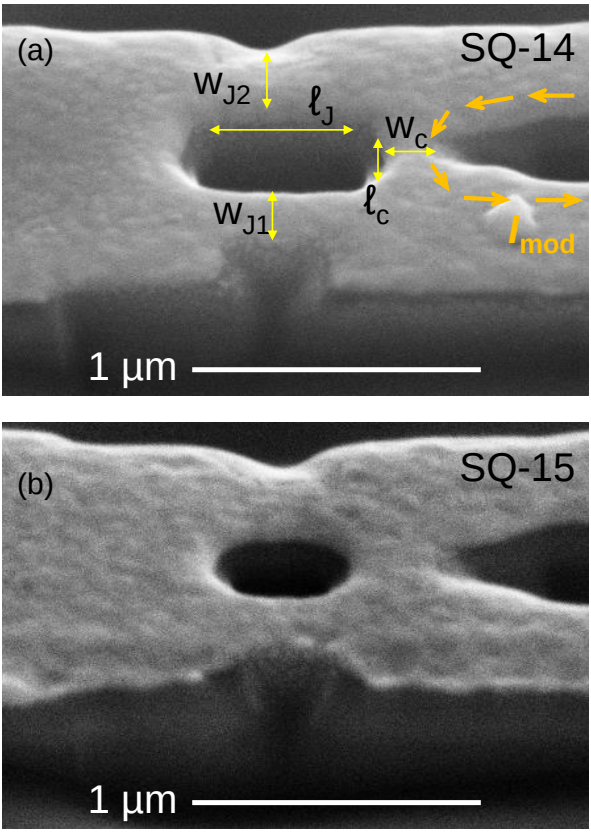

Figure 2.10: SEM images of YBCO/STO superlattice nanoSQUIDs, covered with Au. The grain boundary (not visible) runs from top to bottom and intersects the SQUID hole to form two JJs ($\sim 250 - 320$ nm wide). Figure from appended publication 4.

We present and discuss electric transport and noise properties measured in liquid Helium at $T = 4.2\,\mathrm{K}$ in an electrically and magnetically shielded environment. We focus on two fabricated YBCO/STO superlattice nanoSQUIDs, SQ-14 and SQ-15, which were FIB-patterned from JJ-14 and JJ-15, respectively. We also show data for a single layer (SL) 120 nm-thick YBCO nanoSQUID (SQ-SL), also with a 65 nm-thick Au layer on top, with comparable lateral geometry.

Fig. 2.11 shows IVCs of superlatttice nanoSQUIDs SQ-14 and SQ-15 and, for comparison, the IVC of the single layer nanoSQUID SQ-SL with comparable geometry. For those measurements, I_{mod} has been adjusted to yield maximum critical current $I_{\mathrm{c,max}}$ (solid lines) and minimum critical current $I_{\mathrm{c,min}}$ (dashed lines) on the positive branches.

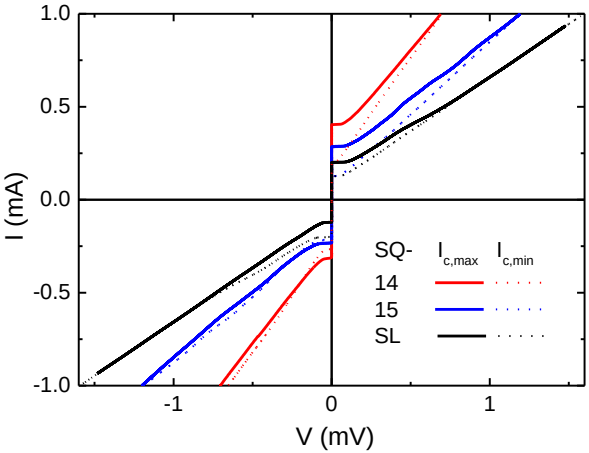

Figure 2.11: IVCs of superlattice SQUIDs (SQ-14 and SQ-15) and single layer SQUID (SQ-SL). Solid (dashed) lines are recorded with I_{mod} adjusted to obtain maximum (minimum) critical current $I_{\mathrm{c,max}}$ for $I > 0$. Figure from appended publication 4.

We find nonhysteretic RCSJ-type IVCs, with values for $I_{\mathrm{c,max}}$, R_{n} and V_{c} which are comparable to GBJJ nanoSQUIDs from single layer YBCO films with similar geometry [40]. We note that we observe for all nanoSQUIDs slightly larger j_{c} and V_{c} values, as compared to those obtained from the 8 μm-wide JJs. This is typical for all our YBCO nanoSQUIDs [49], and we attribute this to the fact the inhomogeneity of the GB (e.g. due to faceting [31]) is slightly reduced upon reducing the JJ width to the deep sub-μm regime.

Fig. 2.12 shows critical current I_c vs I_{mod} oscillations of all three nanoSQUIDs. From the modulation period $I_{mod,0}$ we determine the mutual inductance $M = \Phi_0/I_{mod,0}$. Obviously, the mutual inductance for SQ-14 is more than a factor of two larger than for SQ-15, while SQ-SL has a value of M inbetween.

We find that a narrower constriction yields a larger M. This is also supported by inductance calculations based on simulations of the supercurrrent density distribution in our nanoSQUIDs via the software 3D-MLSI, which solves the London equation in 2-dimensional current sheets [26, 86, 87].

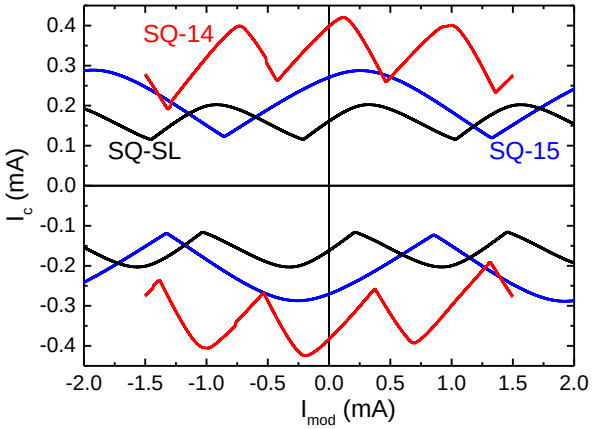

Figure 2.12: Critical current I_c vs. I_{mod} of multilayer SQUIDs (SQ-14 and SQ-15) and single layer SQUID (SQ-SL) for both bias current polarities. Figure from appended publication 4.

Finally, we discuss the flux noise of the superlattice YBCO nanoSQUIDs, which has been measured in FLL mode. Fig. 2.13(a) shows the root-mean-square (rms) spectral density of flux noise $S_\Phi^{1/2}(f)$ of SQ14 and SQ-15 measured with dc bias and with bias reversal at frequency $f_{\rm br} = 20\,{\rm kHz}$. We note that we do not reach the thermal white noise regime even at the highest frequency of 100 kHz up to which we performed measurements. Hence the rms flux noise values $S_\Phi^{1/2}(100\,{\rm kHz}) = 244\,{\rm n}\Phi_0/{\rm Hz}^{1/2}$ for SQ-14 and $104\,{\rm n}\Phi_0/{\rm Hz}^{1/2}$ for SQ-15 (with dc bias readout) are upper bounds for the thermal white noise limit. Those are comparable to the best values for the flux noise at high frequencies obtained for YBCO nanoSQUIDs based on GBJJs in single layer devices [3, 40].

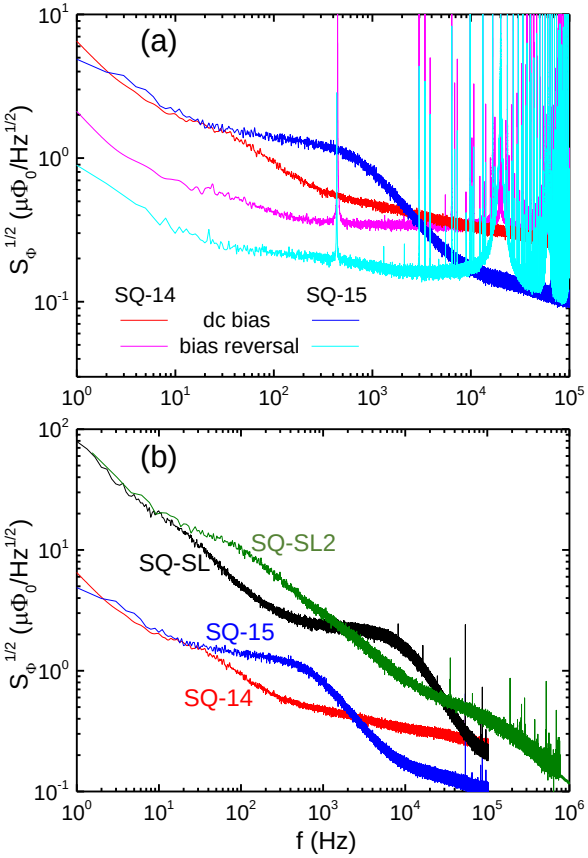

Figure 2.13: Rms spectral density of flux noise $S_\Phi^{1/2}(f)$ measured in FLL mode: (a) data for SQ-14 and SQ-15, measured with dc bias and bias reversal ($f_{\mathrm{br}} = 20\,\mathrm{kHz}$). (b) dc bias readout data of SQ-14, SQ-15, together with SQ-SL and SQ-SL2 on an expanded scale for $S_\Phi^{1/2}$ and f. Figure from appended publication 4.

Most importantly, with dc bias readout we obtain at $f = 1\,\mathrm{Hz}$ values $S_\Phi^{1/2}(1\,\mathrm{Hz}) = 6.5\,\mu\Phi_0/\mathrm{Hz}^{1/2}$ for SQ-14 and $4.9\,\mu\Phi_0/\mathrm{Hz}^{1/2}$ for SQ-15. Those values are more than an order of magnitude lower than what we obtained so far for single layer YBCO nanoSQUIDs on STO bicrystal substrates, and they are comparable to the values for single layer YBCO nanoSQUIDs on MgO bicrystal substrates, as reported very recently [40].

To illustrate this observation, we show in Fig. 2.13(b) again the rms flux noise measured in dc bias mode for SQ-14 and SQ-15, now together with noise data for the single layer devices SQ-SL and SQ-SL2. The latter has also been fabricated on an STO bicrystal substrate with an Au layer on top.

SQ-SL2 has been reported earlier to show the so far lowest flux noise of $\sim 45\,\mathrm{n}\Phi_0/\mathrm{Hz}^{1/2}$ in the thermal white noise limit (at very high frequency $> 7\,\mathrm{MHz}$) for any of our YBCO nanoSQUIDs. This observation shows, that the use of YBCO/STO superlattices instead of YBCO single layer films can significantly reduce $1/f$ noise in YBCO nanoSQUIDs based on GBJJs. Hence, we conclude that the significantly reduced low-frequency excess noise in the YBCO/STO superlattice nanoSQUIDs is most likely due to an improved quality of the grain boundary, as compared to single layer YBCO nanoSQUIDs.

This work was done in Tübingen, without external collaborators. I did the fabrication and patterning of all devices. Futher, I did all measurements, with the help of Julian Linek on noise measurements. Benedikt Müller, Julian Linek and Max Karrer gave me support regarding equipment operation.

Chapter 3

Unpublished Results

This chapter describes unpublished results with respect to the comparison of the performance of YBCO nanoSQUIDs on MgO and STO bicrystal substrates at operation temperatures of 4.2 K versus 77 K, variation of transport and noise properties of superlattices nanoSQUIDs, and the development of a novel weak link based on Ga-FIB-induced nanogrooves in single crystal STO.

3.1 Comparison of single layer YBCO nanoSQUID characteristics at 4.2 K and 77 K

Although the critical temperature T_c of YBCO is above 77 K, our YBCO nanoSQUIDs are presently operated in most cases well below 77 K. Here we compare the transport properties of YBCO nanoSQUIDs operating at 4.2 K and 77 K in order to study the feasibility of the application of the YBCO nanoSQUIDs operated at the temperature of liquid nitrogen.

The nanoSQUIDs are fabricated by epitaxial growth of 120 nm thick YBCO films via pulsed laser deposition on MgO and STO bicrystal substrates with 24 degree misorientation angle. YBCO films are covered in-situ with an Au layer (with thickness 65 nm) as a resistively shunting layer. The transport properties of 8 μm wide (W_d) junctions on bicrystal STO and MgO were analyzed at 4.2 K and 77 K. After nanopatterning with a Ga focused ion beam (FIB), the performance of nanoSQUIDs was measured at 4.2 K and 77 K in a magnetically shielded environment.

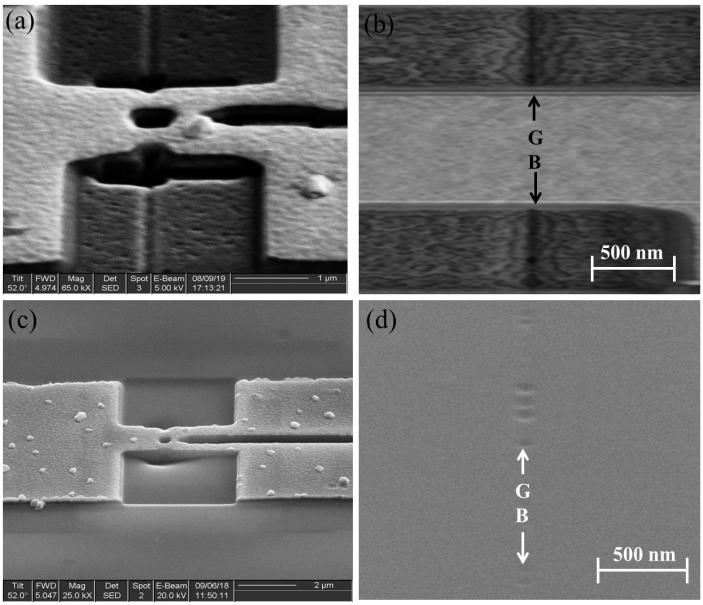

Figure 3.1: SEM images of (a) a YBCO nanoSQUID on bicrystal MgO, (b) Grain-boundary position of bicrystal MgO, (c) SEM image of a YBCO nanoSQUID on bicrystal STO, and (d) Grain-boundary position of bicrystal STO.

Fig. 3.1 (a) shows the SEM image of a YBCO nanoSQUID on a bicrystal MgO substrate. The vertical line indicates the position of the grain boundary intersecting the two SQUID arms.

The loop size $(580\times360)\,\mathrm{nm}^2$ is given by the length L_J of the bridges straddling the grain boundary and by the length L_c of the constriction. The YBCO nanoSQUID has junction widths $W_{\mathrm{J}1}$ around 230 nm and $W_{\mathrm{J}2}$ around 250 nm and a constriction width W_c about 300 nm.

For bicrystal MgO, the grain-boundary position is clearly visible after milling part of YBCO film away with the gallium ion beam as shown in Fig. 3.1(b). A similar structure of YBCO nanoSQUIDs on bicrystal STO with $W_{\mathrm{J}1}$ around 230 nm and $W_{\mathrm{J}2}$ around 240 nm and a constriction width W_c about 250 nm is illustrated in Fig. 3.10(c). For this substrate the grain-boundary position is visible via nano defects aligned along the grain boundary, rather than being a vertical line, as shown in Fig. 3.1(d).

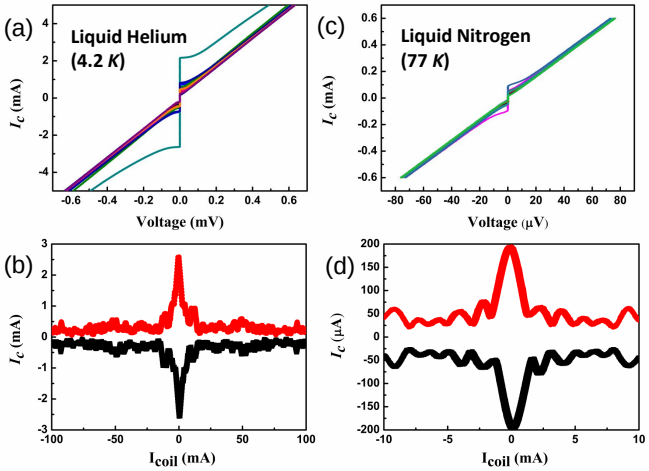

Figure 3.2: (a) IVCs of YBCO junction on bicrystal MgO at liquid helium (4.2 K) under different coil currents. (b) Critical current vs coil current of YBCO junction on bicrystal MgO at 4.2 K. (c) IVCs of YBCO junction on bicrystal MgO at liquid nitrogen 77 K under different coil currents. (d) Critical current vs coil current of the YBCO junction on bicrystal MgO at 77 K.

Figs. 3.2 shows the transport characteristics of YBCO 8 μm-wide junctions on bicrystal MgO at 4.2 K and 77 K. Fig. 3.2(a) illustrates the IVCs under different coil current. The coil is mounted under the sample, and induces a magnetic field perpendicular to the SQUID plane.

The critical current and resistance are 2.6 mA and 0.148 Ω respectively, which can be extraced from the curve. The Josephson length [88] is related with the magnetic London penetration depth [89, 90] and critical current density(j_c), the 8 μm-wide junctions under at 4.2 K are out of the range of the short junction limit. In this case, a non-Fraunhofer-like pattern can be observed as shown in Fig. 3.2(b).

However, at 77 K the critical current drops more than one order of magnitude while the resistance almost keeps the same value. As illustrated, the critical current and the resistance at 77 K are 0.19 mA and 0.148 Ω, respectively. As a result, the more rounded, Fraunhofer-like pattern can be observed in Fig. 3.2(d).

Table 3.1: Summary of geometric and electric YBCO on MgO bicrystal junctions parameters as defined in the text.

Junction 6	d_{YBCO} (nm)	d_{Au} (nm)	I_c (mA)	R (Ω)	V_{c} (mV)	W_d (μm)
(4.2 K)	120 nm	65	2.60	0.148	0.385	8
Junction 6	d_{YBCO} (nm)	d_{Au} (nm)	I_c (mA)	R (Ω)	V_{c} (mV)	W_d (μm)
(77 K)	120 nm	65	0.19	0.148	0.03	8

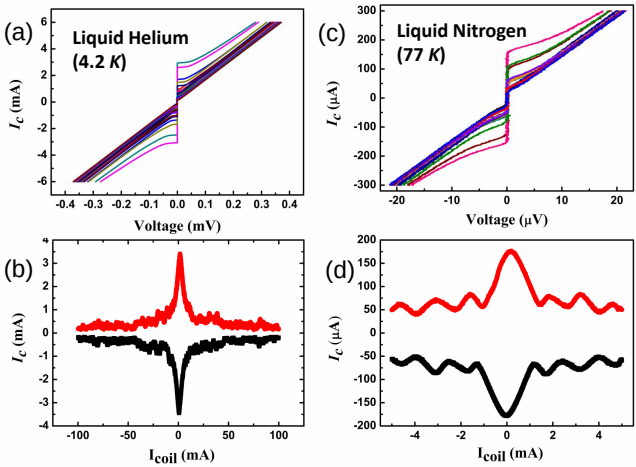

Figure 3.3: (a) IVCs of 8 μm-wide YBCO junction on bicrystal STO at liquid helium (4.2 K) under different coil currents. (b) Critical current vs coil current of 8 μm-wide YBCO junction on bicrystal STO at 4.2 K. (c) IVCs of YBCO junction on bicrystal STO at liquid nitrogen (77 K) under different coil currents. (d) Critical current vs coil current of the YBCO junction on bicrystal STO at 77 K.

.

Figs. 3.3 shows the transport characteristics of YBCO 8μm junctions on bicrystal STO at 4.2 K and 77 K respectively. The critical current for YBCO 8 μm-wide junctions on bicrystal STO at 4.2 K and 77 K are 3.2 mA and 0.18 mA. The critical current

changes between 2.6 mA and 3.5 mA either on bicrystal STO or MgO at 4.2 K.

At this point, there is no big difference for the critical current. However, the resistance of YBCO 8μm wide junctions on bicrystal STO at 4.2 K is much lower compared with YBCO 8 μm-wide junctions on bicrystal MgO at 4.2 K. The resistance of YBCO 8μm junctions on bi-crystal STO at 4.2 K is 0.07 Ω, which means that the characteristic voltage V_c of the junction is almost half compared with 8μm junctions on bicrystal MgO at 4.2 K.

Table 3.2: Summary of geometric and electric YBCO junction parameters as defined in the text.

Junction 6	d_{YBCO} (nm)	d_{Au} (nm)	I_c (mA)	R (Ω)	V_c (mV)	W_d (μm)
(4.2 K)	120 nm	65	3.2	0.07	0.22	8
Junction 6	d_{YBCO} (nm)	d_{Au} (nm)	I_c (mA)	R (Ω)	V_c (mV)	W_d (μm)
(77 K)	120 nm	65	0.18	0.07	0.013	8

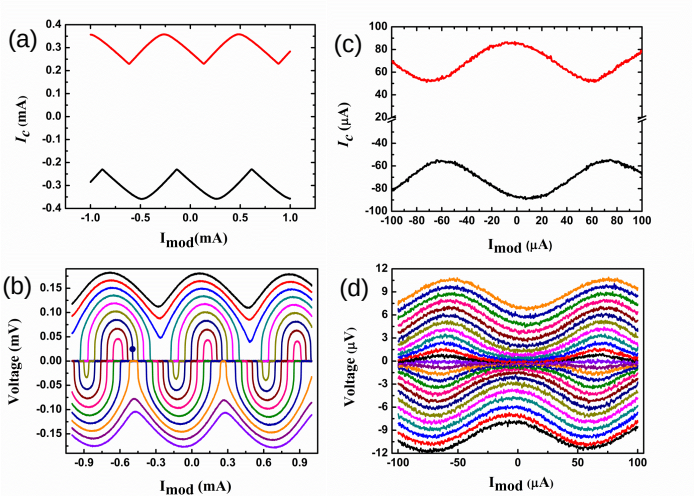

Figure 3.4: Electric transport characteristics of a YBCO nanoSQUID on bicrystal STO. (a) Critical current modulation at $T = 4.2\,\mathrm{K}$ as a function of the applied current through the constriction. (b) Measured voltage vs modulation current with different bias current at 4.2 K. (c) Critical current modulation at $T = 77\,\mathrm{K}$ as a function of the applied current through constriction. (d) Measured voltage vs modulation current with different bias current at 77 K. All curves in (a-d) were traced out in both sweep directions.

Fig. 3.4 shows the electric transport characteristics of a YBCO nanoSQUID on bicrystal STO.Fig. 3.4(a) shows the modulation of the critical current $I_c(I_{\mathrm{mod}})$. The critical current and resistance are 0.36 mA and 0.77 Ω respectively, which

means that a characteristic voltage 0.28 mV can be achieved. From the modulation period, we find for the magnetic flux Φ coupled to the SQUID by I_{mod} the mutual inductance $M = \Phi_0/I_{\mathrm{mod},0}$=2.77 pH. From the modulation depth, we obtain for the screening parameter $\beta_{\mathrm{L}}=I_{\mathrm{c}}L/\Phi_0$=1.77, which yields a SQUID inductance L= 10.2 pH. The value of M, β_{L}, L are 15.9 pH,1.53 and 37.26 pH for the YBCO nanoSQUID working at 77 K.

Regarding transfer function , the values are 9.35 mV/Φ_0 and 0.014 mV/Φ_0 at 4.2 K and 77 K respectively. It is clear that the screening parameter β_{L} does not change a lot compared with YBCO nanoSQUID working at 77 K and 4.2 K. However, the other parameters like M, L increase a lot at 77 K compared with 4.2 K. A lot of parameters need to be optimized if we would like to pursue high flux senstivity of YBCO nanoSQUID working at 77 K.

Table 3.3: Summary of geometric and electric nanoSQUID on STO bicrystal parameters as defined in the text.

SQUID 6	β_L	$2I_0$ (mA)	$R/2$ (Ω)	V_{c} (mV)	M (pH)	L (pH)	W_{J1} (nm)	W_{J2} (nm)	W_{c} (nm)
(4.2 K)	1.77	0.36	0.77	0.28	2.77	10.2	230	240	250
SQUID (6)	β_L	$2I_0$ (mA)	$R/2$ (Ω)	V_{c} (mV)	M (pH)	L (pH)	W_{J1} (nm)	W_{J2} (nm)	W_{c} (nm)
(77 K)	1.53	0.086	0.78	0.067	15.9	37.26	230	240	250

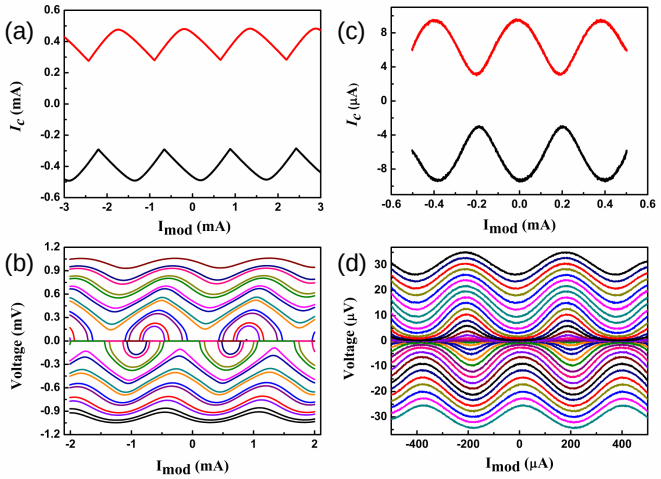

Figure 3.5: Electric transport characteristics of a YBCO nanoSQUID on bicrystal MgO (a) Critical current modulation at T= 4.2 K as a function of the applied current through constriction. (b) Measured voltage vs modulation current with different bias current at 4.2 K. (c) Critical current modulation at T =77 K as a function of the applied current through constriction. (d) Measured voltage vs modulation current with different bias current at 77 K. All curves in (a-d) were traced out in both sweep directions.

Fig. 3.5 shows the electric transport characteristics of a YBCO nanoSQUID on bicrystal MgO. Fig. 3.5(a) shows the modulation of the critical current $I_c(I_{mod})$ at 4.2 K. The critical current and resistance of the YBCO nanoSQUID are 0.48 mA

and 1.88 Ω respectively. As a result, a characteristic voltage of 0.9 mV can be achieved, which is more than three times higher than the characteristic voltage achieved on bicrystal STO at 4.2 K. From the modulation period, we find for the magnetic flux Φ coupled to the SQUID by I_{mod} the mutual inductance $M{=}\Phi_0/I_{\mathrm{mod},0}{=}1.33$ pH. From the modulation depth, we obtain for the screening parameter $\beta_{\mathrm{L}}{=}I_{\mathrm{c}}L/\Phi_0{=}1.4$, which yields a SQUID inductance $L{=}$ 6 pH. The value of M, β_{L}, L are 5.3 pH, 0.5 and 108.9 pH for the YBCO nanoSQUID working at 77 K.

Regarding the transfer function , the values are $3\,\mathrm{mV}/\Phi_0$ and $0.039\,\mathrm{mV}/\Phi_0$ at 4.2 K and 77 K, respectively. It is obvious that the transfer function decreases a lot for the YBCO nanoSQUID working at 77 K either on bi-crystal STO or MgO compared with working at 4.2 K.

Table 3.4: Summary of geometric and electric nanoSQUID on MgO bicrystal parameters as defined in the text.

SQUID (6)	β_L	$2I_0$ (mA)	$R/2$ (Ω)	V_{c} (mV)	M (pH)	L (pH)	W_{J1} (nm)	W_{J2} (nm)	W_{c} (nm)
(4.2 K)	1.4	0.48	1.88	0.90	1.33	6	230	250	300
SQUID (6)	β_L	$2I_0$ (mA)	$R/2$ (Ω)	V_{c} (mV)	M (pH)	L (pH)	W_{J1} (nm)	W_{J2} (nm)	W_{c} (nm)
(77 K)	0.5	0.0095	1.9	0.018	5.3	108.9	230	250	300

In summary, we have successfully fabricated various high-T_{c} nanoSQUIDs on MgO and STO bicrystal substrates with 24° misorientation angle. The disadvantages and advantages of STO vs MgO are illustrated. The transport properties of 8 μm-

wide junctions on bicrystal STO and MgO at 4.2 K and 77 K were analyzed. Subsequently, the performance of nanoSQUIDs patterned on either STO or MgO bicrystals was measured at 4.2 K and 77 K in a magnetically shielded environment.

3.2 Variation of transport and noise properties of superlattice nanoSQUIDs in time

The degradation of the devices hamper production efficiency and a more widespread use of our nanoSQUIDs, e.g., if we want to send them to other groups for placing magnetic nanoparticles (MNPs) on top of our nanoSQUIDs. Long-term sensor stability is a requirement for various applications of high-T_c nanoSQUIDs.

Based on publication 4, we further studied the variation of transport and noise properties of superlattice nanoSQUIDs in time. Fig. 3.6 shows IVCs of multilayer SQUIDs SQ-14 and SQ-15 recorded at different times t, given in days (d) after FIB patterning. Fig. 3.6(b) for the multilayer SQUID 15 shows that the critical current drops within the first 39 days and then stays constant in time. A similar trend is also observed for the multilayer SQUID 14, as shown in Fig. 3.6(a). For both devices we find that the critical current drops within the first ~ 40 days by roughly 50 % and then stays constant in time. Actually, we checked several single-layer SQUIDs (with $d_Y = 120\,\text{nm}$) and none of them showed a finite critical currrent after 350 days.

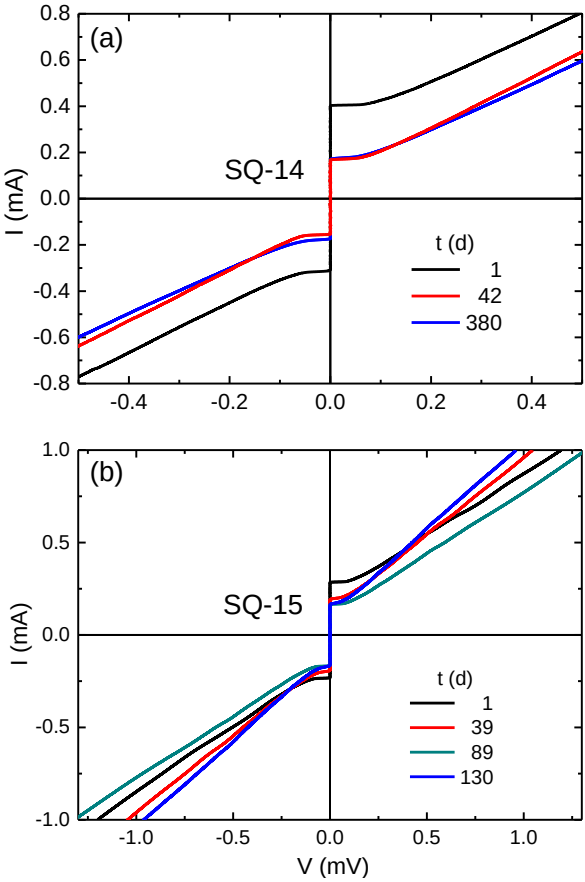

Figure 3.6: IVCs of multilayer SQUIDs SQ-14 (a) and SQ-15 (b) recorded at different times.

Fig. 3.7 shows critical current I_c vs I_{mod}, recorded at different times t (from $t = 1$ to 213 days). From the modulation period $I_{mod,0} = 2.18\,\mathrm{mA}$, we find the mutual inductance $M = \Phi/I_{mod} = \Phi_0/I_{mod,0} = 0.95\,\mathrm{pH}$ at $t = 1\,\mathrm{d}$. After 39 days, the critical current drops by $\sim 30\,\%$ from 287 μA to 200 μA. The drecrease of I_c with t slows down, as shown by further measurements at $t = 89$, 130 and 213 d.

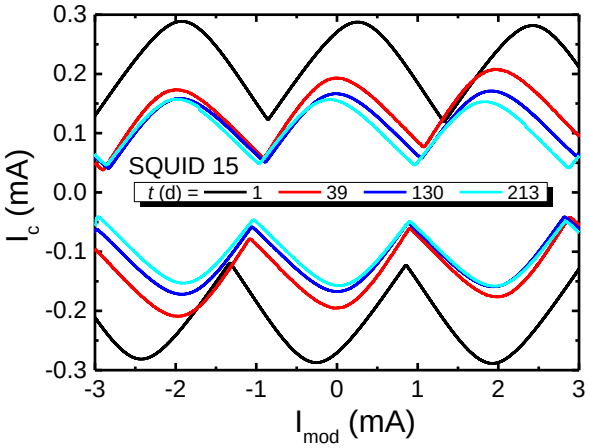

Figure 3.7: Critical current I_c vs. I_{mod} of SQ-15 for both bias current polarities, measured at different times t.

Fig. 3.8 shows V(I_{mod}) oscillations of SQUID 15, measured at different bias currents at $t = 1$, 39, 130 and 213 days. From the modulation period $I_{mod,0} = 2.18\,\mathrm{mA}$, we find the mutual

inductance $M = \Phi/I_{\mathrm{mod}} = \Phi_0/I_{\mathrm{mod},0} = 0.95\,\mathrm{pH}$. We find that M shows only a small increase with time.

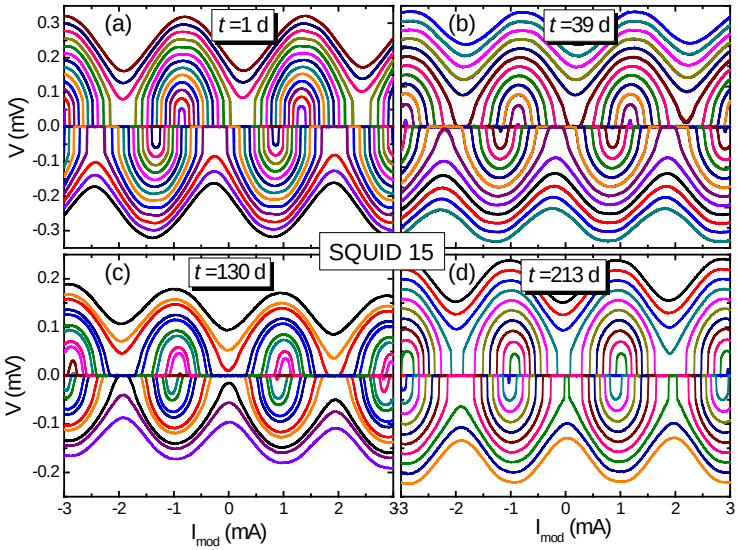

Figure 3.8: (a-d) Voltage-flux characteristics, V-I_{mod}, of SQUID 15 at different bias currents I_{b} measured at different times t.

Fig. 3.9 shows the rms spectral density of flux noise $S_{\Phi}^{1/2}(f)$ of SQ-15 measured at different times (t = 1, 39 and 89 d). Clearly, we do see no degradation of the low-frequency excess noise (at 1 Hz) even after 89 days. Moreover, we find that the mulitlayer nanoSQUIDs have about an order of magni-

tude smaller low-frequency excess flux noise (compared to similar single layer devices) with root-mean-square spetrcal density $S_\Phi^{1/2} \sim 5 - 6\,\mu\Phi_0/\sqrt{\text{Hz}}$ at 1 Hz.

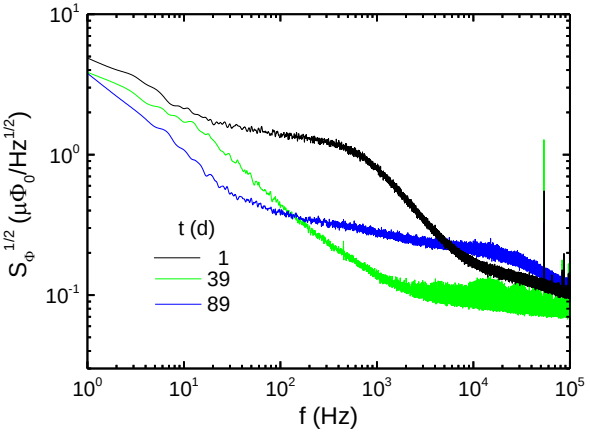

Figure 3.9: Rms spectral density of flux noise $S_\Phi^{1/2}(f)$ measured in FLL mode. SQ-15 measured with dc bias at different times t.

In summary, we have studied the time dependence of the electric transport and noise properties of YBCO/STO nanoSQUIDs on bi-crystal STO substrate with 24 ° misorientation angle over a time span of more than one year. We confirm that long-time stable and high-performance YBCO nanoSQUIDs can be realized in this YBCO/STO periodic structure.

3.3 YBCO Josephson junctions and microSQUIDs based on Ga-FIB-induced nanogrooves in single crystal STO

During the last decades, tremendous efforts have been devoted to achieve high-quality high-T_c weak links. However, until now, it is a challenging job to achieve high-quality and cost-effective weak links in high-T_c superconducting materials due to the intrinsic material properties.

Here, we report on the realization of such novel weak links and microSQUIDs based on them with an artificial bottom-up technology in YBCO thin films on STO single crystal substrates. One first forms nanoslits by irradiating a single crystal STO substrate with different doses of gallium ion beam. Subsequently, a YBCO film with thickness of 120 nm is deposited on the irradiated single STO substrate at 800 °C. An Au layer with thickness of 50 nm is deposited in-situ by electron beam evaporation on top of the YBCO film. After that, photolithography and argon milling process are implemented to create 8 μm wide junctions across the nanoslits. Ga FIB is subsequently used to fabricate YBCO micro SQUIDs.

The Φ_0-periodic response of the critical current versus applied magnetic flux (via a modulation current) coupled into the SQUID hole is observed at 4.2 K. This technique could provide a cost-effective and reliable way for scaling up superconducting circuits operating at liquid-nitrogen temperature.

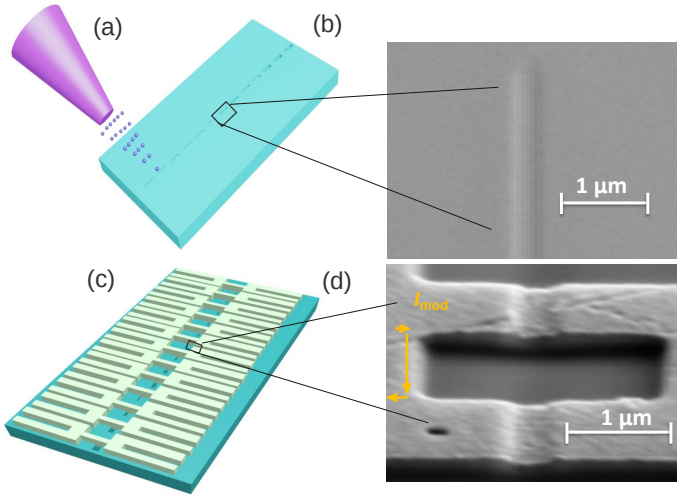

Figure 3.10: (a) STO substrate irradiated with different dose of gallium ion beam. (b) SEM image of STO substrate irradiated by Ga FIB. (c) Schematic illustration of 8 μm wide junctions on STO substrate. (d) SEM image of a YBCO SQUID patterned on irradiated STO substrate.

Fig. 3.10 schematically illustrates the basic idea of artificial bottom-up engineering of a novel JJ-type in high-T_c cuprate superconductors. One first forms nanoslits by irradiating a STO substrate with different doses of gallium ion beam. The energy of the Ga beam is 30 kV and the beam currrent is 50 pA during the irradiation process on a single crystal STO substrate. Both

line scan and defined rectangular area with width between 30 nm and 100 nm are used to fabricate nanoslits. Some experiments still need to be done in order to determine the real irradiation depth for STO substrates after ion irradiation.

After defining the nanoslits on a single crystal STO substrate via Ga FIB. Subsequently, a 120 nm YBCO film is deposited on the irradiated STO substrate at 800 °C. Then, the Au layer with thickness of 50 nm is deposited on the YBCO film via electron beam co-evaporation. SEM images of the STO substrate after ion irradiation are shown in the insets of Fig. 3.10.

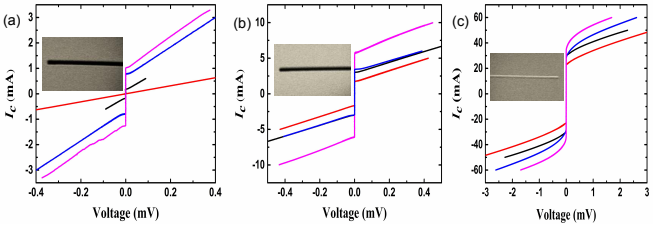

Figure 3.11: Electric-transport characteristics of YBCO junctions at 4.2 K on STO substrates irradiated with different doses of a gallium ion beam. Graphs (a-c) are for high doses, medium doses, and low doses of the gallium ion beam respectively.

Fig. 3.11 shows electric-transport characteristics of 8 μm-wide YBCO junctions fabricated on STO substrates using different doses of the gallium ion beam. With increasing irradiation dose, the critical current of the junctions decreases from

around 40 mA down to 0 mA as shown in Fig. 3.11(a-c).

The irradiation depth changes between 0.05 μm and 0.6 μm with 0.05 μm for each step. Specifically, the irradiation depths range between 0.45 μm and 0.6 μm for Fig. 3.11(a). The irradiation depth for the insert image is 0.6 μm. In Fig. 3.11(b), the irradiation depths range between 0.25 μm and 0.4 μm and the irradiation depths for the insert image is 0.4 μm. In Fig. 3.11(c), the irradiation depths range between 0.05 μm and 0.2 μm and the irradiation depths for the insert image is 0.2 μm.

It is obvious that the IVCs are very different. In Fig. 3.11(c) the I-V curves are more or less of the flux-flow-type [91–93] IVCs. In order to produce high-quality junctions, the irradiated region should be narrow, down to a few nanometer. In this case, the helium ion microscope [94, 95] with a spatial resolution below 1 nm can solve this issue.

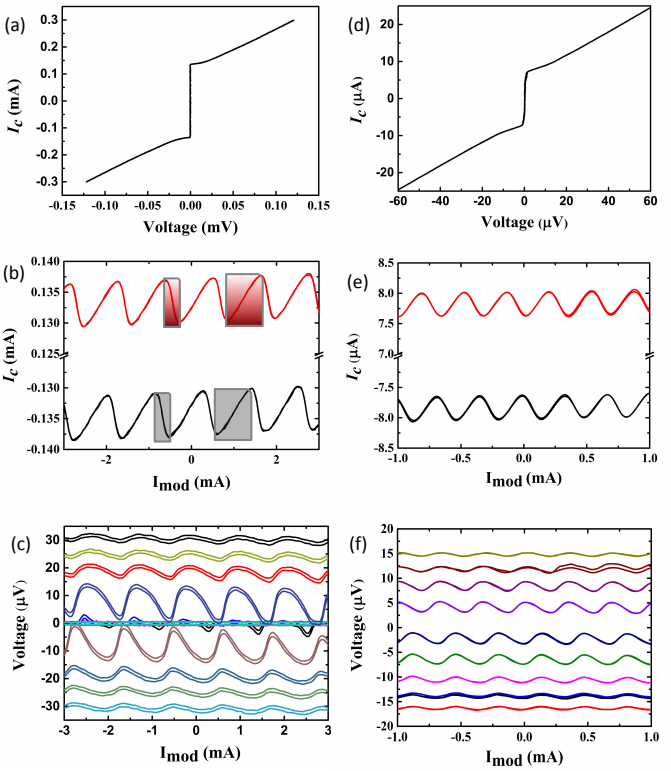

Figure 3.12: Electric-transport characteristics of bottom-up YBCO micro nanoSQUIDs. (a,d)IVC,(b,e)critical current versus modulation current and (c,f) SQUID voltage dependence on modulation current for different bias currents. (a-c) are for chip 1 SQUID 14 and (d-f) for chip2 SQUID 4.

Regarding the fabrication of YBCO SQUIDs, Ga FIB is used in order to cut 8 μm-wide junctions into micro SQUIDs with junction widths (W_J) around 450 nm and SQUID hole's dimension about (500×400) nm^2 . Furthermore, we use the Ga FIB to cut a slit perpendicular to the GB towards the Grain-Boundary. With this process step, we define a constriction of width (W_c) around 150 nm and length L_c in the SQUID loop.

Fig. 3.12 shows the electric transport properties, i.e., IVCs (a,d), $I_c(I_{mod})$ (b,e) and $V(I_{mod})$ (c,f) at 4.2 K, for chip 1 SQUID 14 and chip 2 SQUID 4 respectively. The critical current and resistance for chip 1 SQUID 14 are I_c=137 μA and R_n=0.65 Ω respectively, which corresponds to a characteristic voltage $V_c = I_c R_n = 90\,\mu$V. At $T = 4.2$ K, we typically obtain $V_c \approx 0.1 - 1$ mV for YBCO GBJJs on STO bicrystals with 24° misorientation angle, if they are covered with ~ 60 nm thick Au. So, the characteristic voltage is smaller than the typical value we obtained from YBCO GBJJs on STO bicrystals with 24° misorientation angle covered with ~ 60 nm thick Au.

For chip 1 SQUID 14, we determine the modulation period $I_{\mathrm{mod},0}$ from the $I_c(I_{\mathrm{mod}})$ curves and from this the mutual inductance M=$\Phi_0/I_{\mathrm{mod},0}$=1.88 pH. From the modulation depth of $I_c(I_{\mathrm{mod}})$ oscillations, we could estimate the screening parameter $\beta_L \equiv 2I_0L/\Phi_0 = 17.3$ via the approximate relation $(I_{c,\max} - I_{c,\min})/I_{c,\max} \approx 1/(1+\beta_L)$. Based on the estimated β_L, together with the measured $I_{c,\max}$, we determine L to be equal to 260.9 pH. The value of L is large, which may be due to the asymmetry of the two junctions and a strongly nonsinusoidal current-phase relation. The skewness of I_c vs I_{mod} as marked with red and gray rectangles may arise from a non-sinusoidal

current phase relation of the weak link and needs further investigation.

The periodic curves $I_c(I_{mod})$ and $V(I_{mod})$ of both SQUIDs as shown in Fig. 3.12 demonstrate that the weak links operate as Josephson junctions.

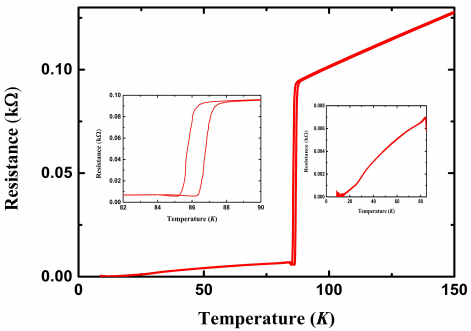

Figure 3.13: R(T) dependence of YBCO nanoSQUIDs on chip 1. The insets show zooms of the R(T) curve.

Fig. 3.13 shows the resistance R (at constant bias current I_b=10 μA) versus temperature T of SQUID 14 on chip 1. It is clear to see that the critical temperature of the YBCO film is around 86 K without gallium ion beam irradiation. For the YBCO film grown on the irradiated STO substrate area, the decrease in resistance as the temperature is lowered indicates

that the irradiated area is normal conducting.

In summary, we demonstrate the realization of a novel weak link in YBCO thin films, produced with an artificial bottom-up technology. The observed SQUID oscillations, show that Josephson junctions have been realized. This technique could provide a cost-effective and reliable pathway for scaling up superconducting circuits.

Chapter 4

Conclusion and outlook

In this thesis first review the major achievements obtained so far on the development of sensitive nanoSQUIDs in Tübingen, based on Nb and $YBa_2Cu_3O_7$ (YBCO) as superconductors. This part emphasizes the advantages offered by YBCO nanoSQUIDs, fabricated on bicrystal $SrTiO_3$ (STO) substrates, regarding enhanced ranges of temperature and magnetic field, over which those nanoSQUIDs can be operated.

Regarding the application of YBCO nanoSQUIDs fabricated on STO bicrystal substrates, we have studied the occurrence of field-driven nucleation and annihilation of magnetic vortices in individual ultra-small ferromagnetic Co particles by YBCO nanoSQUID magnetometry. We demonstrate that the Co particles reveal bi-stable magnetization states at zero applied field, with the vortex state being the ground state. This topic is im-

portant in order to understand the thermal and temporal stability of noncollinear and other nontrivial spin textures, e.g., vortices or skyrmions, confined in ultra-small ferromagnets.

To improve the sensitivity and long-time stability of our magnetic sensors are the main research motivations in this thesis. We demonstrate that YBCO nanoSQUIDs patterned on MgO bicrystals can have non-hysteretic IVCs at 4.2 K even without Au as shunting layer due to a much smaller dielectric permittivity than $SrTiO_3$ (STO), which shows the high potential of further improvements in the flux sensitivity. We have studied the transport properties of YBCO nanoSQUID based on bicrystal MgO with the decreasing of Au film as shunting layer.

However, the results show that the decrease of Au film thickness by Argon milling is accompanied by the decrease of critical current, which poses restrictions on the further improvement of the flux sensitivity. At this point, we propose to deposit a 30 nm Au film directly as protection layer without Argon milling process or a 30 nm STO film as protection layer during the cutting process.

More importantly, we note that by using an optimized process for removing the Au layer after FIB milling, as demonstrated very recently, and/or starting the fabrication process with a thinner Au/STO layer on top of YBCO, it still seems possible to improve the sensitivity of such devices down to the level of single spin sensitivity.

Furthermore, we report on the fabrication and characterization of nanopatterned dc SQUIDs with grain boundary Josephson junctions based on heteroepitaxially grown $YBa_2Cu_3O_{7-\delta}$ (YBCO)/ $SiTrO_3$ (STO) superlattices on STO bicrystal sub-

strates. Nanopatterning is performed by Ga focused ion beam milling. The electric transport properties and thermal white flux noise of superlattice nanoSQUIDs are comparable to single layer YBCO devices on STO bicrystals.

However, we find that the superlattice nanoSQUIDs have more than an order of magnitude smaller low-frequency excess flux noise, with root-mean-square spectral density $S_\Phi^{1/2} \sim 5 - 6\,\mu\Phi_0/\sqrt{\mathrm{Hz}}$ at 1 Hz (Φ_0 is the magnetic flux quantum). We attribute this improvement to an improved microstructure at the grain boundaries forming the Josephson junctions in our YBCO nanoSQUDs. Furthermore, we confirm that longtime stable YBCO nanoSQUIDs can be achieved based on heteroepitaxially grown $YBa_2Cu_3O_{7-\delta}$ (YBCO)/ $SiTrO_3$ (STO) superlattices on STO bicrystal substrates.

Last but not least, we developed the novel weak link based on artificial bottom-up technology in high-T_c material and illustrate the nanoSQUIDs performance towards at 77 K. This technique combining with the cutting edge equipment like Extreme Ultraviolet Lithography could provide a cost-effective and reliable pathway for scaling up [96–99] superconducting circuits operating at liquid-nitrogen temperature.

References

[1]Q. Pankhurst, N. Thanh, S. Jones, and J. Dobson, "Progress in applications of magnetic nanoparticles in biomedicine", Journal of Physics D: Applied Physics **42**, 224001 (2009).

[2]W. T. Coffey and Y. P. Kalmykov, "Thermal fluctuations of magnetic nanoparticles: Fifty years after Brown", Journal of Applied Physics **112**, 121301 (2012).

[3]T. Schwarz, R. Wölbing, C. F. Reiche, B. Müller, M.-J. Martínez-Pérez, T. Mühl, B. Büchner, R. Kleiner, and D. Koelle, "Low-noise $YBa_2Cu_3O_7$ nanoSQUIDs for performing magnetization-reversal measurements on magnetic nanoparticles", Physical Review Applied **3**, 044011 (2015).

[4]L. Bogani and W. Wernsdorfer, "Molecular spintronics using single-molecule magnets", Nature materials **7**, 179–186 (2008).

[5]M. N. Leuenberger, F. Meier, and D. Loss, "Quantum spin dynamics in molecular magnets", in *Molecular Magnets Recent Highlights* (Springer, 2002), pp. 101–117.

[6]J. Gallop, "SQUIDs: some limits to measurement", Superconductor Science and Technology **16**, 1575 (2003).

[7]T. Mühl, J. Körner, S. Philippi, C. Reiche, A. Leonhardt, and B. Büchner, "Magnetic force microscopy sensors providing in-plane and perpendicular sensitivity", Applied Physics Letters **101**, 112401 (2012).

[8]A. Winkler, T. Mühl, S. Menzel, R. Kozhuharova-Koseva, S. Hampel, A. Leonhardt, and B. Büchner, "Magnetic force microscopy sensors using iron-filled carbon nanotubes", Journal of Applied Physics **99**, 104905 (2006).

[9]A. Leonhardt, S. Hampel, C. Mueller, I. Moench, R. Koseva, M. Ritschel, D. Elefant, K. Biedermann, and B. Buechner, "Synthesis, Properties, and Applications of Ferromagnetic-Filled Carbon Nanotubes", Chemical vapor deposition **12**, 380–387 (2006).

[10]K. Lipert, S. Bahr, F. Wolny, P. Atkinson, U. Weißker, T. Mühl, O. Schmidt, B. Büchner, and R. Klingeler, "An individual iron nanowire-filled carbon nanotube probed by micro-Hall magnetometry", Applied Physics Letters **97**, 212503 (2010).

[11]G. Mihajlović, K. Aledealat, P. Xiong, S. Von Molnar, M. Field, and G. J. Sullivan, "Magnetic characterization of a single superparamagnetic bead by phase-sensitive micro-Hall magnetometry", Applied Physics Letters **91**, 172518 (2007).

[12]D. Koelle, "Magnetic sensors: A tip for better sensing", Nature nanotechnology **8**, 617–618 (2013).

[13]W. Wernsdorfer, "Classical and quantum magnetization reversal studied in nanometer-sized particles and clusters", in *Handbook of Advanced Magnetic Materials* (Springer, 2006), pp. 77–127.

[14]A. G. Troeman, H. Derking, B. Borger, J. Pleikies, D. Veldhuis, and H. Hilgenkamp, "NanoSQUIDs based on niobium constrictions", Nano Letters **7**, 2152–2156 (2007).

[15]A. Finkler, Y. Segev, Y. Myasoedov, M. L. Rappaport, L. Ne'eman, D. Vasyukov, E. Zeldov, M. E. Huber, J. Martin, and A. Yacoby, "Self-aligned nanoscale SQUID on a tip", Nano letters **10**, 1046–1049 (2010).

[16]M. J. Martínez-Pérez and D. Koelle, "NanoSQUIDs: Basics & recent advances", Physical Sciences Reviews **2**, 20175001 (2017).

[17]C. H. Wu, Y. T. Chou, W. C. Kuo, J. H. Chen, L. M. Wang, J. C. Chen, K. L. Chen, U. C. Sou, H. C. Yang, and J. T. Jeng, "Fabrication and characterization of high-T_c $YBa_2Cu_3O_{7-x}$ nanoSQUIDs made by focused ion beam milling", Nanotechnology **19**, 315304 (2008).

[18]K. Hasselbach, C. Ladam, V. Dolocan, D. Hykel, T. Crozes, K. Schuster, and D. Mailly, "High resolution magnetic imaging: MicroSQUID force microscopy", in Journal of Physics: Conference Series, Vol. 97, 1 (IOP Publishing, 2008), p. 012330.

[19]L. Hao and C. Granata, "Recent trends and perspectives of nanoSQUIDs: introduction to 'Focus on nanoSQUIDs and their applications'", Superconductor Science and Technology **30**, 050301 (2017).

[20]W. Wernsdorfer, "From micro-to nano-SQUIDs: applications to nanomagnetism", Superconductor Science and Technology **22**, 064013 (2009).

[21]T. Schurig, "Making SQUIDs a practical tool for quantum detection and material characterization in the micro-and nanoscale", in Journal of Physics: Conference Series, Vol. 568, 3 (IOP Publishing, 2014), p. 032015.

[22]P. Vohralik and S. Lam, "NanoSQUID detection of magnetization from ferritin nanoparticles", Superconductor Science and Technology **22**, 064007 (2009).

[23]A. Vettoliere, C. Granata, P. Walke, E. Esposito, B. Ruggiero, and M. Russo, "SQUID Sensors for High Spatial Resolution Magnetic Imaging and for Nanoscale Applications", in *Sensors and Microsystems* (Springer, 2010), pp. 251–255.

[24]J. Clarke and A. I. Braginski, *The SQUID handbook: Applications of SQUIDs and SQUID systems* (John Wiley & Sons, 2006).

[25]C. Veauvy, K. Hasselbach, and D. Mailly, "Micro-SQUID microscopy of vortices in a perforated superconducting Al film", Physical Review B **70**, 214513 (2004).

[26]R. Wölbing, T. Schwarz, B. Müller, J. Nagel, M. Kemmler, R. Kleiner, and D. Koelle, "Optimizing the spin sensitivity of grain boundary junction nanoSQUIDs—towards detection of small spin systems with single-spin resolution", Superconductor Science and Technology **27**, 125007 (2014).

[27]M. J. Martínez-Pérez, D. Gella, B. Müller, V. Morosh, R. Wölbing, J. Sesé, O. Kieler, R. Kleiner, and D. Koelle, "Three-axis vector nano superconducting quantum interference device", ACS nano **10**, 8308–8315 (2016).

[28]M. Martínez-Pérez, J. Pablo-Navarro, B. Müller, R. Kleiner, C. Magén, D. Koelle, J. De Teresa, and J. Sesé, "NanoSQUID magnetometry on individual as-grown and annealed Co nanowires at variable temperature", Nano letters **18**, 7674–7682 (2018).

[29]S. Mandal, T. Bautze, O. A. Williams, C. Naud, É. Bustarret, F. Omnes, P. Rodiere, T. Meunier, C. Bäuerle, and L. Saminadayar, "The diamond superconducting quantum interference device", ACS nano **5**, 7144–7148 (2011).

[30]C. Granata and A. Vettoliere, "Nano superconducting quantum interference device: A powerful tool for nanoscale investigations", Physics Reports **614**, 1–69 (2016).

[31]H. Hilgenkamp and J. Mannhart, "Grain boundaries in high-T_c superconductors", Reviews of Modern Physics **74**, 485 (2002).

[32]R. Jaklevic, J. Lambe, A. Silver, and J. Mercereau, "Quantum interference effects in Josephson tunneling", Physical Review Letters **12**, 159 (1964).

[33]J. Zimmerman, P. Thiene, and J. Harding, "Design and operation of stable rf-biased superconducting point-contact quantum devices, and a note on the properties of perfectly clean metal contacts", Journal of Applied Physics **41**, 1572–1580 (1970).

[34]B. D. Josephson, "The discovery of tunnelling supercurrents", Reviews of Modern Physics **46**, 251 (1974).

[35]D. Koell, "Lecture Notes, Univ.Tübingen", Moderne Physik B – Festkörperphysik (2020).

[36]R. Kleiner, D. Koelle, F. Ludwig, and J. Clarke, "Superconducting quantum interference devices: State of the art and applications", Proceedings of the IEEE **92**, 1534–1548 (2004).

[37]D. Drung, "High-T_c and low-T_c dc SQUID electronics", Superconductor science and technology **16**, 1320 (2003).

[38]R. Arpaia, M. Arzeo, S. Nawaz, S. Charpentier, F. Lombardi, and T. Bauch, "Ultra low noise $YBa_2Cu_3O_{7-\delta}$ nano superconducting quantum interference devices implementing nanowires", Applied Physics Letters **104**, 072603 (2014).

[39]M. Faley, J. Dammers, Y. Maslennikov, J. Schneiderman, D. Winkler, V. Koshelets, N. Shah, and R. Dunin-Borkowski, "High-T_c SQUID biomagnetometers", Superconductor Science and Technology **30**, 083001 (2017).

[40]J. Lin, B. Müller, J. Linek, M. Karrer, M. Wenzel, M. J. Martínez-Pérez, R. Kleiner, and D. Koelle, "$YBa_2Cu_3O_7$ nano superconducting quantum interference devices on MgO bicrystal substrates", Nanoscale **12**, 5658–5668 (2020).

[41]B. Müller, M. Karrer, F. Limberger, M. Becker, B. Schröppel, C. Burkhardt, R. Kleiner, E. Goldobin, and D. Koelle, "Josephson Junctions and SQUIDs Created by Focused Helium-Ion-Beam Irradiation of $YBa_2Cu_3O_7$", Physical Review Applied **11**, 044082 (2019).

[42]S. A. Cybart, E. Cho, T. Wong, B. H. Wehlin, M. K. Ma, C. Huynh, and R. Dynes, "Nano Josephson superconducting tunnel junctions in $YBa_2Cu_3O_{7-\delta}$ directly patterned with a focused helium ion beam", Nature nanotechnology **10**, 598 (2015).

[43]D. Stornaiuolo, G. Rotoli, D. Massarotti, F. Carillo, L. Longobardi, F. Beltram, and F. Tafuri, "Resolving the effects of frequency-dependent damping and quantum phase diffusion in $YBa_2Cu_3O_{7-x}$ Josephson junctions", Physical Review B **87**, 134517 (2013).

[44]E. Trabaldo, C. Pfeiffer, E. Andersson, R. Arpaia, A. Kalaboukhov, D. Winkler, F. Lombardi, and T. Bauch, "Grooved Dayem nanobridges as building blocks of high-performance $YBa_2Cu_3O_{7-\delta}$ SQUID magnetometers", Nano letters **19**, 1902–1907 (2019).

[45]S. K. Lam and S. Gnanarajan, "Transport properties of bi-epitaxial $YBa_2Cu_3O_{7-\delta}$ grain boundary Josephson junctions: Experimental evidence of a subdominant superconducting phase", Physical Review B **78**, 094521 (2008).

[46]N. Browning, J. Buban, P. Nellist, D. Norton, M. Chisholm, and S. Pennycook, "The atomic origins of reduced critical currents at [001] tilt grain boundaries in $YBa_2Cu_3O_{7-\delta}$ thin films", Physica C: Superconductivity **294**, 183–193 (1998).

[47]T. Amrein, L. Schultz, B. Kabius, and K. Urban, "Orientation dependence of grain-boundary critical current densities in high-T_c bicrystals", Physical Review B **51**, 6792 (1995).

[48]F. Herbstritt, T. Kemen, L. Alff, A. Marx, and R. Gross, "Transport and noise characteristics of submicron high-temperature superconductor grain-boundary junctions", Applied Physics Letters **78**, 955–957 (2001).

[49]J. Nagel, K. Konovalenko, M. Kemmler, M. Turad, R. Werner, E. Kleisz, S. Menzel, R. Klingeler, B. Büchner, R. Kleiner, et al., "Resistively shunted $YBa_2Cu_3O_7$ grain boundary junctions and low-noise SQUIDs patterned by a focused ion beam down to 80 nm linewidth", Superconductor Science and Technology **24**, 015015 (2010).

[50]M. Martínez-Pérez, B. Müller, D. Schwebius, D. Korinski, R. Kleiner, J. Sesé, and D. Koelle, "NanoSQUID magnetometry of individual cobalt nanoparticles grown by focused electron beam induced deposition", Superconductor Science and Technology **30**, 024003 (2016).

[51]R. Córdoba, J. Sesé, J. De Teresa, and M. R. Ibarra, "High-purity cobalt nanostructures grown by focused-electron-beam-induced deposition at low current", Microelectronic Engineering **87**, 1550–1553 (2010).

[52]T. Schwarz, J. Nagel, R. Wölbing, M. Kemmler, R. Kleiner, and D. Koelle, "Low-noise nano superconducting quantum interference device operating in tesla magnetic fields", ACS nano **7**, 844–850 (2013).

[53]M. Huth, F. Porrati, C. Schwalb, M. Winhold, R. Sachser, M. Dukic, J. Adams, and G. Fantner, "Focused electron beam induced deposition: A perspective", Beilstein journal of nanotechnology **3**, 597–619 (2012).

[54]J. De Teresa, A. Fernández-Pacheco, R. Córdoba, L. Serrano-Ramón, S. Sangiao, and M. R. Ibarra, "Review of magnetic nanostructures grown by focused electron beam induced deposition (FEBID)", Journal of Physics D: Applied Physics **49**, 243003 (2016).

[55]T. Shinjo, T. Okuno, R. Hassdorf, K. Shigeto, and T. Ono, "Magnetic vortex core observation in circular dots of permalloy", Science **289**, 930–932 (2000).

[56]M. Goiriena-Goikoetxea, K. Guslienko, M. Rouco, I. Orue, E. Berganza, M. Jaafar, A. Asenjo, M. Fernández-Gubieda, L. F. Barquín, and A. Garcıéa-Arribas, "Magnetization reversal in circular vortex dots of small radius", Nanoscale **9**, 11269–11278 (2017).

[57]J. Mejıéa-López, D. Altbir, P. Landeros, J. Escrig, A. Romero, I. V. Roshchin, C.-P. Li, M. Fitzsimmons, X. Batlle, and I. K. Schuller, "Development of vortex state in circular magnetic nanodots: Theory and experiment", Physical Review B **81**, 184417 (2010).

[58]R. K. Dumas, K. Liu, C.-P. Li, I. V. Roshchin, and I. K. Schuller, "Temperature induced single domain–vortex state transition in sub-100 nm Fe nanodots", Applied Physics Letters **91**, 202501 (2007).

[59]S. Wintz, V. Tiberkevich, M. Weigand, J. Raabe, J. Lindner, A. Erbe, A. Slavin, and J. Fassbender, "Magnetic vortex cores as tunable spin-wave emitters", Nature nanotechnology **11**, 948–953 (2016).

[60]V. Pribiag, I. Krivorotov, G. Fuchs, P. Braganca, O. Ozatay, J. Sankey, D. Ralph, and R. Buhrman, "Magnetic vortex oscillator driven by dc spin-polarized current", Nature Physics **3**, 498–503 (2007).

[61]K. Schultheiss, R. Verba, F. Wehrmann, K. Wagner, L. Körber, T. Hula, T. Hache, A. Kákay, A. Awad, V. Tiberkevich, et al., "Excitation of whispering gallery magnons in a magnetic vortex", Physical review letters **122**, 097202 (2019).

[62]T. Schwarz, "nanoSQUIDs for the detection of small spin systems in strong magnetic fields", PhD thesis (Universität Tübingen, 2015).

[63]A. Beck, A. Stenzel, O. Froehlich, R. Gerber, R. Gerdemann, L. Alff, B. Mayer, R. Gross, A. Marx, J. Villegier, et al., "Fabrication and superconducting transport properties of bicrystal grain boundary Josephson junctions on different substrates", IEEE Transactions on Applied Superconductivity **5**, 2192–2195 (1995).

[64]H. Suzuki, Y. Fujiwara, Y. Hirotsu, T. Yamashita, and T. Oikawa, "In-plane orientations and grain boundaries of $YBa_2Cu_3O_{7-x}$ thin films on (001) MgO substrates grown by metalorganic chemical vapor deposition", Japanese journal of applied physics **32**, 1601 (1993).

[65]J. Du, S. Gnanarajan, and A. Bendavid, "Influence of MgO surface conditions on the in-plane crystal orientation and critical current density of epitaxial YBCO films", Physica C: Superconductivity **400**, 143–152 (2004).

[66]J. Du, S. Gnanarajan, and A. Bendavid, "Characterization of MgO substrates for growth of epitaxial YBCO thin films", Superconductor Science and Technology **18**, 1035 (2005).

[67]R. Werner, C. Raisch, A. Ruosi, B. Davidson, P. Nagel, M. Merz, S. Schuppler, M. Glaser, J. Fujii, T. Chassé, et al., "$YBa_2Cu_3O_7/La_{0.7}Ca_{0.3}MnO_3$ bilayers: Interface coupling and electric transport properties", Physical Review B **82**, 224509 (2010).

[68]S. Scharinger, M. Turad, A. Stöhr, V. Leca, E. Goldobin, R. Mints, D. Koelle, and R. Kleiner, "Magnetic field dependence of the critical current in $YBa_2Cu_3O_{7-\delta}$/Au/Nb ramp-zigzag Josephson junctions", Physical Review B **86**, 144531 (2012).

[69]I. Jin, C. Chen, S. Pai, B. Ming, D. Kang, T. Venkatesan, F. Machalett, K. Edinger, J. Orloff, and J. Melngailis, "Fabrication of HTS Josephson junctions on substrates prepared by focused ion beam system", IEEE transactions on applied superconductivity **9**, 2894–2897 (1999).

[70]C. Neumann, K. Yamaguchi, Y. Ando, K. Hayashi, S. Fujino, T. Takenaka, K. Suzuki, and Y. Enomoto, "YBCO-Josephson-Junctions on MgO Fabricated by a Focused Ion Beam", in *Advances in Superconductivity V* (Springer, 1993), pp. 1091–1094.

[71]H. Sasaki, T. Matsuda, T. Kato, T. Muroga, Y. Iijima, T. Saitoh, F. Iwase, Y. Yamada, T. Izumi, Y. Shiohara, et al., "Specimen preparation for high-resolution transmission electron microscopy using focused ion beam and Ar ion milling", Microscopy **53**, 497–500 (2004).

[72]D. Koelle, R. Kleiner, F. Ludwig, E. Dantsker, and J. Clarke, "High-transition-temperature superconducting quantum interference devices", Reviews of Modern Physics **71**, 631 (1999).

[73]C. Rogers and R. Buhrman, "Composition of 1/f Noise in Metal-Insulator-Metal Tunnel Junctions", Physical review letters **53**, 1272 (1984).

[74]V. Foglietti, W. Gallagher, M. Ketchen, A. Kleinsasser, R. Koch, S. Raider, and R. Sandstrom, "Low-frequency noise in low 1/f noise dc SQUID's", Applied physics letters **49**, 1393–1395 (1986).

[75]B. Savo, F. C. Wellstood, and J. Clarke, "Low-frequency excess noise in Nb-Al_2O_3-Nb Josephson tunnel junctions", Applied physics letters **50**, 1757–1759 (1987).

[76]A. Marx and R. Gross, "Scaling behavior of 1/f noise in high-temperature superconductor Josephson junctions", Applied physics letters **70**, 120–122 (1997).

[77]R. Arpaia, M. Arzeo, R. Baghdadi, E. Trabaldo, F. Lombardi, and T. Bauch, "Improved noise performance of ultrathin YBCO Dayem bridge nanoSQUIDs", Superconductor Science and Technology **30**, 014008 (2016).

[78]R. H. Koch, J. Clarke, W. Goubau, J. M. Martinis, C. Pegrum, and D. J. Van Harlingen, "Flicker (1/f) noise in tunnel junction dc SQUIDs", Journal of low temperature physics **51**, 207–224 (1983).

[79]F. Ludwig, D. Koelle, E. Dantsker, D. Nemeth, A. Miklich, J. Clarke, and R. Thomson, "Low noise $YBa_2Cu_3O_{7-x}$–$SrTiO_3$–$YBa_2Cu_3O_{7-x}$ multilayers for improved superconducting magnetometers", Applied physics letters **66**, 373–375 (1995).

[80]M. Faley, S. Mi, A. Petraru, C. Jia, U. Poppe, and K. Urban, "Multilayer buffer for high-temperature superconductor devices on MgO", Applied physics letters **89**, 082507 (2006).

[81]J.-M. Triscone and Ø. Fischer, "Superlattices of high-temperature superconductors: synthetically modulated structures, critical temperatures and vortex dynamics", Reports on Progress in Physics **60**, 1673 (1997).

[82]R. Gross, A. Gupta, E. Olsson, A. Segmüller, and G. Koren, "Critical current density of strained multilayer thin films of $Nd_{1.83}Ce_{0.17}CuO_x/YBa_2Cu_3O_{7-x}$", Applied physics letters **57**, 203–205 (1990).

[83]S. Foltyn, H. Wang, L. Civale, Q. Jia, P. Arendt, B. Maiorov, Y. Li, M. Maley, and J. MacManus-Driscoll, "Overcoming the barrier to 1000 A/cm width superconducting coatings", Applied Physics Letters **87**, 162505 (2005).

[84]A. V. Pan, S. Pysarenko, and S. X. Dou, "Drastic improvement of surface structure and current-carrying ability in $YBa_2Cu_3O_7$ films by introducing multilayered structure", Applied Physics Letters **88**, 232506 (2006).

[85]S. Foltyn, L. Civale, J. MacManus-Driscoll, Q. Jia, B. Maiorov, H. Wang, and M. Maley, "Materials science challenges for

high-temperature superconducting wire", Nature materials **6**, 631–642 (2007).

[86]M. Khapaev, M. Y. Kupriyanov, E. Goldobin, and M. Siegel, "Current distribution simulation for superconducting multilayered structures", Superconductor Science and Technology **16**, 24 (2002).

[87]J. Nagel, O. Kieler, T. Weimann, R. Wölbing, J. Kohlmann, A. Zorin, R. Kleiner, D. Koelle, and M. Kemmler, "Superconducting quantum interference devices with submicron Nb/HfTi/Nb junctions for investigation of small magnetic particles", Applied Physics Letters **99**, 032506 (2011).

[88]M. Moshe, V. Kogan, and R. Mints, "Edge-type Josephson junctions in narrow thin-film strips", Physical Review B **78**, 020510 (2008).

[89]L. Thiel, D. Rohner, M. Ganzhorn, P. Appel, E. Neu, B. Müller, R. Kleiner, D. Koelle, and P. Maletinsky, "Quantitative nanoscale vortex imaging using a cryogenic quantum magnetometer", Nature nanotechnology **11**, 677 (2016).

[90]D. Rohner, L. Thiel, B. Müller, M. Kasperczyk, R. Kleiner, D. Koelle, and P. Maletinsky, "Real-space probing of the local magnetic response of thin-film superconductors using single spin magnetometry", Sensors **18**, 3790 (2018).

[91]J. Schneider, H. Kohlstedt, and R. Wördenweber, "Nanobridges of optimized $YBa_2Cu_3O_7$ thin films for superconducting flux-flow type devices", Applied physics letters **63**, 2426–2428 (1993).

[92]M. Asim and S. Hasanain, "Modified flux flow in polycrystalline YBCO: temperature and current dependence", Superconductor Science and Technology **9**, 461 (1996).

[93]S. Tinchev, "Properties of YBCO weak links prepared by local oxygen-ion induced modification", Physica C: Superconductivity **256**, 191–198 (1996).

[94]B. Ward, J. A. Notte, and N. Economou, "Helium ion microscope: A new tool for nanoscale microscopy and metrology", Journal of Vacuum Science & Technology B: Microelectronics and Nanometer Structures Processing, Measurement, and Phenomena **24**, 2871–2874 (2006).

[95]J. Morgan, J. Notte, R. Hill, and B. Ward, "An introduction to the helium ion microscope", Microscopy today **14**, 24–31 (2006).

[96]W. Mallison, S. Berkowitz, A. Hirahara, M. Neal, and K. Char, "A multilayer $YBa_2Cu_3O_x$ Josephson junction process for digital circuit applications", Applied physics letters **68**, 3808–3810 (1996).

[97]T. Wolf, N. Bergeal, J. Lesueur, C. J. Fourie, G. Faini, C. Ulysse, and P. Febvre, "YBCO Josephson junctions and striplines for RSFQ circuits made by ion irradiation", IEEE Transactions on applied superconductivity **23**, 1101205–1101205 (2013).

[98]R. Simon, J. Burch, K. Daly, W. Dozier, R. Hu, A. Lee, J. Luine, H. Manasevit, C. Platt, S. Schwarzbek, et al., "Progress towards a YBCO circuit process", in *Science and Technology*

of Thin Film Superconductors 2 (Springer, 1990), pp. 549–559.

[99]B. D. Hunt, M. G. Forrester, J. Talvacchio, and R. M. Young, "High-resistance HTS edge junctions for digital circuits", IEEE transactions on applied superconductivity **9**, 3362–3365 (1999).

Appended publications

Publication 1

Reproduced with permission from B. Müller et al., 2019 IEEE International Superconductive Electronics Conference (ISEC) Proceedings, IEEE Xplore (2019); DOI: 10.1109/ISEC46533.2019.8990906.
© 2019 IEEE.

IEEE International Superconductive Electronics Conference (ISEC), Riverside, CA, USA;
published by IEEE Xplore; DOI: 10.1109/ISEC46533.2019.8990906

$YBa_2Cu_3O_7$ and Nb NanoSQUIDs for the Investigation of Magnetization Reversal of Individual Magnetic Nanoparticles

B. Müller, J. Lin, J. Linek, M. Karrer, F. Limberger, L. Koch, E. Goldobin, R. Kleiner, D. Koelle
Physikalisches Institut and CQ in LISA+
Universität Tübingen
Tübingen, Germany

V. Morosh, T. Weimann, O. F. Kieler
Fachbereich 2.4 Quantenelektronik
Physikalisch Technische Bundesanstalt (PTB)
Braunschweig, Germany

J. Sesé, M. J. Martínez-Pérez
Instituto de Nanociencia de Aragón (INA)
Universidad de Zaragoza - CSIC
Zaragoza, Spain

***Abstract*—We report on the fabrication, performance and application of sensitive $YBa_2Cu_3O_7$ (YBCO) and Nb nanoSQUIDs to magnetization reversal measurements of individual magnetic nanoparticles. The YBCO SQUIDs are based on grain boundary Josephson junctions and are patterned in a single layer of epitaxially grown YBCO films by Ga focused ion beam milling. The Nb SQUIDs contain sandwich-type Josephson junctions with normal conducting HfTi barriers; they are fabricated with a multilayer technology that includes patterning by e-beam lithography and a combination of milling techniques and chemical-mechanical polishing. Due to the small inductance of the SQUID loops, ultralow white flux noise at 4.2 K can be achieved, which yields spin sensitivities of down to a few Bohr magnetons per unit bandwidth for a magnetic nanoparticle placed at 10 nm distance to the SQUID loop.**

Keywords—nanoSQUID; YBCO; Nb; focused ion beam milling; flux noise; magnetic nanoparticle

I. Introduction

Magnetic properties of micro- and nanoscale objects, are currently a topic of intensive research. Their investigation requires the development of appropriate tools, e.g. for detection of the magnetization reversal of individual magnetic nanoparticles (MNPs) [1, 2]. Promising candidates for this task are strongly miniaturized superconducting quantum interference devices (SQUIDs) – so-called nanoSQUIDs [3, 4]. The magnetization hysteresis loop of a ferromagnetic nanoparticle can be detected via the induced change of stray magnetic field coupled to a nanoSQUID by a MNP that is placed in close vicinity to the SQUID loop. The figure of merit for this kind of SQUID application is the spin sensitivity $S_\mu^{1/2}$, defined as the rms flux noise $S_\Phi^{1/2}$ of the nanoSQUID divided by the coupling factor $\phi_\mu=\Phi/\mu$ (flux Φ coupled to the SQUID per magnetic moment μ of the MNP).

B. Müller acknowledges funding by the German Academic Scholarship Foundation. J. Lin acknowledges funding by the Chinese Research Council (CRC). This work was supported by the Deutsche Forschungsgemeinschaft (DFG), via KO 1303/13-1, -2, KI 698/3-1, -2 and GO 1106/6-1, and by the COST action NANOCOHYBRI (CA 16218).

II. Device Fabrication

A. YBCO nanoSQUIDs

We fabricate devices from thin films of $YBa_2Cu_3O_7$ (YBCO), epitaxially grown by pulsed laser deposition on bicrystal $SrTiO_3$ (STO) or MgO substrates, with 24° misorientation angle of the grain boundary. The grain boundary formed in the YBCO film (typically 120 nm thick) acts as a Josephson junction [5]. Subsequently, we deposit in-situ by sputtering or electron beam evaporation 50-70 nm thick Au on top of YBCO. The Au film serves as a protection layer and for providing electrical contacts. Next, we pattern 4-8 µm wide bridges straddling the grain boundary by photolithography and Ar ion milling. As a final patterning step, we use Ga focused ion beam (FIB) milling to pattern the SQUID loop, to define the width of the grain boundary junctions and to pattern a narrow constriction (100-300 nm wide) into the SQUID loop [6-9]. The constriction in the SQUID loop provides the location of highest sensitivity to the stray field produced by a MNP placed on top of the constriction [9]. Moreover, by sending a current I_{mod} through the constriction, the flux coupled to the SQUID can be controlled and modulated. This feature can be conveniently used for on-chip flux modulation of the nanoSQUIDs and for their operation in flux-locked loop readout [8].

B. Nb nanoSQUIDs

The Nb SQUIDs are fabricated by a multilayer process, involving in-situ sputtering of a Nb/HfTi/Nb trilayer plus ex-situ sputtered SiO_2 insulating and Nb wiring layer and a combination of electron beam lithography, various etching steps and chemical-mechanical polishing. The Nb films are typically 160-200 nm thick, and the normal conducting HfTi barriers have typical thicknesses ranging from 17 to 25 nm. For

978-1-7281-1196-4/19/$31.00 ©2019 IEEE

details of the fabrication process and superconductor-normal metal-superconductor (SNS) Josephson junction characteristics see [10-13]. The typical nanoSQUID geometry of our devices is of a microstrip-type: two Nb lines (typically 150-250 nm wide) are patterned on top of each other (separated by SiO_2) and are vertically connected by two trilayer Nb/HfTi/Nb Josephson junctions. The lateral spacing of the two junctions is a few μm down to ~100 nm, and the vertical spacing of the two Nb lines is ~200 nm; both quantities together define the size of the SQUID loop with a loop plane that is perpendicular to the substrate surface. This microstrip geometry allows us to conveniently control and modulate magnetic flux coupled to the SQUID loop via a modulation current I_{mod}, which is flowing along one of the two Nb lines [13].

III. NanoSQUID Performance

The YBCO and Nb nanoSQUIDs have nonhysteretic current-voltage characteristics (IVCs) at temperature T=4.2 K that are reasonably well described by the resistively and capacitively shunted junction model. Due to the small inductance L of the SQUID loop (in the pH range), the rms flux noise in the thermal white noise region $S_{\Phi,w}^{1/2}$ is very low – typically a few 100 $n\Phi_0/Hz^{1/2}$ (Φ_0 is the magnetic flux quantum). The lowest values obtained so far are $S_{\Phi,w}^{1/2}$=45 $n\Phi_0/Hz^{1/2}$ [8] and 110 $n\Phi_0/Hz^{1/2}$ [4] for our best YBCO and Nb nanoSQUIDs, respectively. For a MNP placed at 10 nm distance from the SQUID loop, this corresponds to spin sensitivities $S_\mu^{1/2}$~4 $\mu_B/Hz^{1/2}$ and ~10 $\mu_B/Hz^{1/2}$, respectively (μ_B is the Bohr magneton). For the determination of $S_\mu^{1/2}$, we calculate the coupling factor by numerical simulation of the supercurrents flowing in the SQUID loop, for any given planar SQUID geometry. For these simulations we use 3D-MLSI [14], a finite-element-based software, solving the London equations in 2D sheets; this takes into account the thickness of the superconducting films forming the SQUID loop and the value of the London penetration depth [4, 6, 9, 15].

The YBCO nanoSQUIDs offer the advantage of operation over a very wide temperature range, so far from 300 mK up to 80 K [9]. Moreover, due to the huge upper critical field of YBCO, these devices offer the potential for operation up to very strong magnetic fields. So far, we operated devices at 4.2 K up to 3 T, and performed flux noise measurements up to 1 T [7]. A major drawback of the YBCO nanoSQUIDs is their strong low-frequency excess noise, scaling approximately as $S_\Phi \sim 1/f$ (f is the frequency) [8]. This is due to strong critical current fluctuations, as typically observed for SQUIDs based on cuprate superconductors [16]. Moreover, $1/f$ noise may further increase upon applying strong magnetic fields, unless the entry of Abrikosov vortices can be avoided [17].

The temperature range of operation of the Nb nanoSQUIDs is much more restricted, as compared to the YBCO nanoSQUIDs. Typically our devices operate below ~6 K. Upon cooling to below 4.2 K, the devices start to develop hysteresis in their IVCs which can be attributed to Joule heating in the junctions. The temperature below which hysteresis appears increases with increasing critical current density and area of the junctions [18]. Operation in strong magnetic fields, although restricted to below ~1 T is also possible, in particular for devices with strongly reduced linewidths, for which operation up to ~0.5 T has been demonstrated [12].

The mature multilayer technology for Nb nanoSQUID fabrication offers the possibility to develop quite complex device layouts which can be used e.g. to develop gradiometric designs for operation in strong homogeneous magnetic fields. One promising approach is the development of 3D vector nanoSQUIDs that have been realized recently [19]. This device combines two orthogonal microstrip-type Nb nanoSQUIDs (loop normal along the x- and y-axis) with a gradiometric nanoSQUID with loop normal along the z-axis. For a MNP placed in the center of one of the gradiometer loops, the switching of its magnetic moment upon applying a magnetic field in z-direction can then be traced by all three orthogonal nanoSQUIDs, to record simultaneously all three vector components of the magnetic moment of the MNP. This approach shall be particularly useful for studies of the magnetic anisotropy of individual MNPs.

IV. Applications of nanoSQUIDs to Magnetization Reversal Measurements of Magnetic Nanoparticles

We have used YBCO and Nb nanoSQUIDs to perform magnetization reversal measurements of individual MNPs of different geometries: nanopillars, -disks, -wires and -tubes.

A. MNP measurements with YBCO nanoSQUIDs

A Fe nanowire, embedded in a carbon nanotube, has been placed on top of a YBCO nanoSQUID with ~300 nm distance from the SQUID loop (on the side opposite to the constriction in the loop). A magnetic field was applied along the wire axis (the easy axis of magnetization). While sweeping the magnetic field, the flux coupled to the SQUID was recorded, yielding an almost ideal rectangular-shaped magnetization hysteresis curve at 4.2 K, as expected for a single-domain state [8]. The detected flux change of ±82.5 $m\Phi_0$ in the saturated states was in very good agreement with the calculated signal (from the simulated coupling factor integrated over the volume of the Fe wire), assuming the literature value for the saturation magnetization of Fe. The observed switching field ~100 mT was ten times smaller than predicted from a simple Stoner-Wohlfarth reversal mechanism. This low switching field, however, was in very good agreement with estimates based on magnetization reversal via curling mode [8].

We note that further measurements with similar YBCO nanoSQUIDs have been performed on Co nanowires grown by focused-electron-beam-induced deposition (FEBID), as reported in [20]. In this case, the nanowires were suspended above the nanoSQUIDs. These measurements clearly showed improved performance of the nanowires that had been annealed after FEBID growth [21].

In a further series of measurements, we have demonstrated the benefit of using YBCO nanoSQUIDs for MNP measurements over a wide temperature range [9]. In this case, Co nanopillars and nanodisks were grown by FEBID directly on top of the constriction in the SQUID loop. For the Co MNPs that revealed single-domain states, we recorded hysteresis loops from 300 mK up to 80 K. The observed T-dependence of the switching fields was shown to be in very good agreement

with predictions from a model for thermally induced magnetization reversal [9].

B. MNP measurements with Nb nanoSQUIDs

Nb nanoSQUIDs have been integrated into the torque magnetometer setup of the Poggio group at Univ. Basel to investigate individual Ni, permalloy and CoFeB nanotubes. The combined system enables simultaneous measurements of the integral magnetization by dynamic cantilever torque magnetometry and local magnetization by nanoSQUID magnetometry [13]. Combined torque and SQUID measurements on individual Ni nanotubes, supported by micromagnetic simulations of magnetization configurations, suggest reversal via the formation of vortexlike states within the nanotube [22]. Such stray-field free states can have applications for memory and noninvasive sensing.

CONCLUSIONS AND OUTLOOK

YBCO and Nb nanoSQUIDs have been developed for the investigation of magnetization reversal of individual magnetic nanoparticles. Very small SQUID inductances enable the realization of ultralow flux noise of the nanoSQUIDs in the thermal white noise limit. For MNPs placed in 10 nm distance to the SQUID loop, this translates into spin sensitivities down to only a few Bohr magnetons per unit bandwidth, which is appropriate for many studies on individual MNPs. Apart from further suppression of $1/f$ noise, a key challenge is the development of reliable routines for placing MNPs in a controlled way in close vicinity to the nanoSQUIDs, ideally at variable position and temperature. For YBCO nanoSQUIDs, the recently developed creation of Josephson junctions and SQUIDs by focused He ion irradiation [23, 24] can provide new perspectives for creating advanced nanoscale devices

REFERENCES

[1] W. Wernsdorfer, K. Hasselbach, D. Mailly, B. Barbara, A. Benoit, L. Thomas, and G. Suran, "DC-SQUID magnetization measurements of single magnetic particles," J. Magn. Magn. Mater., vol. 145, pp. 33-39, 1995.

[2] W. Wernsdorfer, "Classical and quantum magnetization reversal studied in nanometersized particles and clusters," Adv. Chem. Phys., vol. 118, pp. 99-190, 2001.

[3] C. Granata, and A. Vettoliere, "Nano superconducting quantum interference device: A powerful tool for nanoscale investigations," Phys. Rep., vol. 614, pp. 1-69, 2016.

[4] M. J. Martínez-Pérez, and D. Koelle, "NanoSQUIDs: Basics & recent advances," Phys. Sci. Rev., vol. 2, 20175001, 2017.

[5] H. Hilgenkamp, and J. Mannhart, "Grain boundaries in high-T_c superconductors," Rev. Mod. Phys., vol. 74, pp. 485-549, 2002.

[6] J. Nagel, K. B. Konovalenko, M. Kemmler, M. Turad, R. Werner, E. Kleisz, S. Menzel, R. Klingeler, B. Büchner, R. Kleiner, and D. Koelle, "Resistively shunted $YBa_2Cu_3O_7$ grain boundary junctions and low-noise SQUIDs patterned by a focused ion beam down to 80 nm linewidth," Supercond. Sci. Technol., vol. 24, 015015, 2011.

[7] T. Schwarz, J. Nagel, R. Wölbing, M. Kemmler, R. Kleiner, and D. Koelle, "Low-noise superconducting quantum interference device operating in tesla magnetic fields," ACS Nano, vol. 7, pp. 844-850, 2013.

[8] T. Schwarz, R. Wölbing, C. F. Reiche, B. Müller, M. J. Martínez-Pérez, T. Mühl, B. Büchner, R. Kleiner and D. Koelle, "Low-noise $YBa_2Cu_3O_7$ nano-SQUIDs for performing magnetization reversal measurements on magnetic nanoparticles," Phys. Rev. Applied, vol. 3, 044001, 2015.

[9] M. J. Martínez-Pérez, B. Müller, D. Korinski, R. Kleiner, J. Sesé, and D. Koelle, "NanoSQUID magnetometry of individual cobalt nanoparticles grown by focused electron beam induced deposition," Supercond. Sci. Technol., vol. 30, 024003, 2017.

[10] D. Hagedorn, O. Kieler, R. Dolata, R. Behr, F. Müller, J. Kohlmann, and J. Niemeyer, "Modified fabrication of planar sub-µm superconductor–normal metal–superconductor Josephson junctions for use in a Josephson arbitrary waveform synthesizer," Supercond. Sci. Technol., vol. 19, pp. 294-298, 2006.

[11] J. Nagel, O. F. Kieler, T. Weimann, R. Wölbing, J. Kohlmann, A. B. Zorin, R. Kleiner, D. Koelle, and M. Kemmler, "Superconducting quantum interference devices with submicron Nb/HfTi/Nb junctions for investigation of small magnetic particles," Appl. Phys. Lett., vol. 99, 032506, 2011.

[12] R. Wölbing, J. Nagel, T. Schwarz, O. Kieler, T. Weimann, J. Kohlmann, A. B. Zorin, M. Kemmler, R. Kleiner, and D. Koelle, "Nb nano superconducting quantum interference devices with high spin sensitivity for operation in magnetic fields up to 0.5 T," Appl. Phys. Lett., vol. 102, 192601, 2013.

[13] J. Nagel *et al.*, "Nanoscale multifunctional sensor formed by a Ni nanotube and a scanning Nb nanoSQUID," Phys. Rev. B, vol. 88, 064425, 2013.

[14] M. M. Khapaev, M. Yu. Kupriyanov, E. Goldobin, and M Siegel, "Current distribution simulation for superconducting multi-layered structures," Supercond. Sci. Technol., vol. 16, pp. 24-27, 2003.

[15] R. Wölbing, T. Schwarz, B. Müller, J. Nagel, M. Kemmler, R. Kleiner, and D. Koelle, "Optimizing the spin sensitivity of grain boundary junction nanoSQUIDs—towards detection of small spin systems with single-spin resolution," Supercond. Sci. Technol., vol. 27, 125007, 2014.

[16] D. Koelle, R. Kleiner, F. Ludwig, E. Dantsker, and J. Clarke, "High-transition-temperature superconducting quantum interference devices," Rev. Mod. Phys., vol. 71, pp. 631-686, 1999.

[17] A. H. Miklich, D. Koelle, T. J. Shaw, F. Ludwig, D. T. Nemeth, E. Dantsker, J. Clarke, N. McN Alford, and T. W. Button, "Low-frequency excess noise in $YBa_2Cu_3O_{7-x}$ dc superconducting quantum interference devices cooled in static magnetic fields," Appl. Phys. Lett., vol. 64, pp. 3494-3496, 1994.

[18] V. Morosh *et al.*, "Transport and noise properties of sub-100 nm planar Josephson junctions with metallic barrier for nanoSQUID applications," unpublished.

[19] M. J. Martínez-Pérez, D. Gella, B. Müller, V. Morosh, R. Wölbing, J. Sesé, O. Kieler, R. Kleiner, and D. Koelle, "Three-axis vector vector nano superconducting quantum interference device," ACS Nano, vol. 10, pp. 8308-8315, 2016.

[20] M. J. Martínez-Pérez, J. Pablo-Navarro, B. Müller, R. Kleiner, C. Magén, D. Koelle, J. M. de Teresa, and J. Sesé, "NanoSQUID magnetometry on individual as-grown and annealed Co nanowires at variable temperature," Nano Lett., vol. 18, 7674-7682, 2018.

[21] J. Pablo-Navarro, C. Magén, and J. M. de Teresa, "Purified and crystalline three-dimensional electron-beam-induced deposits: The successful case of cobalt for high performance magnetic nanowires," ACS Appl. Nano Mater., vol. 1, pp. 38-46, 2018.

[22] A. Buchter *et al.*, "Reversal mechanism of an individual Ni nanotube simultaneously studied by torque and SQUID magnetometry," Phys. Rev. Lett., vol. 111, 067202, 2013.

[23] S. A. Cybart, E. Y. Cho, J. T. Wong, B. H. Wehlin, M. K. Ma, C. Huynh, and R. C. Dynes, "Nano Josephson superconducting tunnel junctions in $YBa_2Cu_3O_{7-\delta}$ directly patterned with a focused helium ion beam," Nature Nanotechnol., vol. 10, pp. 598-602, 2015.

[24] B. Müller, M. Karrer, F. Limberger, M. Becker, B. Schröppel, C. J. Burkhadt, R. Kleiner, E. Goldobin, and D. Koelle, "Josephson junctions and SQUIDs created by focused helium-ion-beam irradiation of $YBa_2Cu_3O_7$," Phys. Rev. Applied, vol. 11, 044082, 2019.

Publication 2

Reproduced with permission from M. J. Martínez-Pérez et al., Nanoscale 12, 2587-2595 (2020). © 2020 The Royal Society of Chemistry.

Nanoscale

PAPER

View Article Online
View Journal | View Issue

Published on 07 January 2020. Downloaded by UNIVERSITAET TUEBINGEN on 6/21/2020 5:53:58 AM.

Check for updates

Cite this: *Nanoscale*, 2020, **12**, 2587

Magnetic vortex nucleation and annihilation in bi-stable ultra-small ferromagnetic particles

M. J. Martínez-Pérez, ⋆[a,b] B. Müller,[c] J. Lin,[c] L. A. Rodriguez,[d,e] E. Snoeck,[f] R. Kleiner,[c] J. Sesé [a,g] and D. Koelle [c]

Received 5th October 2019,
Accepted 3rd January 2020

DOI: 10.1039/c9nr08557b

rsc.li/nanoscale

Vortex-mediated magnetization reversal in *individual ultra-small* (~100 nm) ferromagnetic particles at low temperatures is studied by nanoSQUID magnetometry. At zero applied bias field, the flux-closure magnetic state (vortex) and the quasi uniform configuration are bi-stable. This stems from the extremely small size of the nanoparticles that lies very close to the limit of single-domain formation. The analysis of the temperature-dependent (from 0.3 to 70 K) hysteresis of the magnetization allows us to infer the nature of the ground state magnetization configuration. The latter corresponds to a vortex state as also confirmed by electron holography experiments. Based on the simultaneous analysis of the vortex nucleation and annihilation data, we estimate the magnitude of the energy barriers separating the quasi single-domain and the vortex state and their field dependence. For this purpose, we use a modified power-law scaling of the energy barriers as a function of the applied bias field. These studies are essential to test the thermal and temporal stability of flux-closure states stabilized in ultra-small ferromagnets.

Mesoscopic magnetic objects exhibit a number of possible (meta)stable magnetization configurations, *e.g.*, single-domain or non-homogeneous states including domain walls or flux-closure states like the archetypal magnetic vortex.[1] The latter is relevant for a number of applications going from electronics[2] and information technologies[3] up to cancer therapy.[4] Attempts are being made in order to reduce the size of magnetic units hosting vortices below the 100 nm range to favour their use in spintronic nanodevices and biomedical applications.[5,6]

Flat magnetic discs having radii in the few hundreds of nanometers to several micrometers range are prominent examples of bi-stability.[7,8] Their ground state configuration usually corresponds to a flux-closure vortex state (VS).[9] However, the quasi-single domain (QSD) state is metastable in ultra-small discs with radius $r \lesssim 100$ nm and thickness $t \sim 10$ nm.[7,10] If the size of the nanodisc is further reduced reaching $r \lesssim 50$ nm and t of few nm the QSD state becomes the ground state whereas the vortex is metastable at zero field. The transition probability between these states is governed by the height of the energy barriers between them, the temperature and the waiting time.[11,12] Energy barriers have been extensively studied both theoretically and experimentally in the case of uniformly magnetized particles reversing their magnetization *M via*, *e.g.*, coherent rotation, curling or domain wall nucleation and motion.[8,13–16] However, there are no theories allowing to compute the magnitude of energy barriers and their dependence on the applied bias field H in the case of nonuniform magnetization reversal. This is a problem of utmost importance as it determines ultimately the thermal and temporal stability of a given magnetic configuration.

In this work, we will focus on the energy barriers for vortex nucleation (U_n) and annihilation (U_a) in ultra-small ferromagnetic nanoparticles. Such problem has been analyzed theoretically in ref. 10 where U_n was calculated within the so-called rigid vortex model (at zero bias field). The latter usually results in energy barriers substantially larger than those found experimentally.[17,18] The rigid vortex model was extended in ref. 6 to account for small radius nanodots, where the vortex core occupies an important fraction of the total volume of the particle. Most experimental studies assume that, around the critical fields H_n^0 and H_a^0, the energy barriers follow a power-law scaling as a function of the bias field: $U_{a/n} = U_{a/n}^0(1 - H/H_{a/n}^0)^\alpha$. This is usually accepted for QSD particles, where the theory of coherent magnetization reversal predicts $1 < \alpha < 2$, approaching 2 when the field is applied along the easy axis of

[a]*Instituto de Ciencia de Materiales de Aragón and Departamento de Física de la Materia Condensada, CSIC-Universidad de Zaragoza, 50009 Zaragoza, Spain. E-mail: pemar@unizar.es*
[b]*Fundación ARAID, Avda. de Ranillas, 50018 Zaragoza, Spain*
[c]*Physikalisches Institut – Experimentalphysik II and Center for Quantum Science (CQ) in LISA⁺, Universität Tübingen, Auf der Morgenstelle 14, D-72076 Tübingen, Germany*
[d]*Departamento de Física, Universidad del Valle, A.A. 25360, Cali, Colombia*
[e]*Center of Excellence on Novel Materials - CENM, Universidad del Valle, A.A. 25360, Cali, Colombia*
[f]*CEMES-CNRS 29, rue Jeanne Marvig, B.P. 94347, F-31055 Toulouse Cedex, France*
[g]*Laboratorio de Microscopías Avanzadas (LMA), Instituto de Nanociencia de Aragón (INA), Universidad de Zaragoza, 50018 Zaragoza, Spain*

Published on 07 January 2020. Downloaded by UNIVERSITAET TUEBINGEN on 6/21/2020 5:53:58 AM.

the particle.[13] In practice, $\alpha < 2$ is typically found in processes involving domain wall nucleation and propagation.[19]

Thermal and temporal stability in magnetic vortices stabilized in large (micron-sized) ferromagnetic discs has been studied in the past. For example, *individual* permalloy discs with radii $r \sim 250$–500 nm and thicknesses $t \sim 40$–50 nm were studied experimentally in ref. 20 and 21 by means of Hall and torque magnetometry, respectively. In the former, the temperature dependence of the hysteresis curves at low temperatures was interpreted as a signature of thermal activation over an energy barrier for both vortex nucleation and annihilation. In the latter work, measurements performed at different sweeping rates at room temperature yielded an equivalent explanation for vortex annihilation whereas signatures of supercooling were found for vortex nucleation. Regarding the field-dependence of the energy barriers, $\alpha = 1$ was assumed in the former work whereas $\alpha = 3/2$ was used in the latter. These studies yielded values in the range $U_n^0/k_B \sim 10^3$–10^4 K and $U_a^0/k_B \sim 10^4$–10^5 K. Other experimental works have focused on large arrays of permalloy discs. The vortex annihilation process was investigated at temperatures close to room temperature in ref. 17 using an array of relatively large discs with $r \sim 1$ μm and $t \sim 32$ nm. Fitting together the temperature and field sweeping rate-dependence of the magnetic susceptibility, different values of $1 < \alpha < 2.5$ yielded energy barriers for vortex annihilation in the range $2 \times 10^5 < U_a^0/k_B < 5 \times 10^6$ K. Kakazei *et al.* measured the slow decay of the magnetization of a saturated dot array at magnetic fields close to the vortex nucleation field.[22] The energy barrier for vortex nucleation was approximated as $U_n = U_n^0 + a(H/H_n^0 - 1)^\alpha$ with $3.6 < \alpha < 4$. From these measurements, $U_n^0/k_B \sim 10^4$ K was estimated for discs having $r \sim 250$ nm and $t \sim 40$ nm. Melkov *et al.* estimated the relaxation rate to the VS by measuring the dot occupation number through ferromagnetic resonance in smaller discs with $r \sim 150$ nm and $t \sim 14$ nm.[18] From the relaxation rate, an energy barrier for vortex nucleation at zero field $U_n(H = 0)/k_B \sim 10^3$ K was found. Interestingly, the latter also enabled the experimental estimation of the field dependence of $U_n(H)$.

Here, we study the vortex mediated magnetization reversal in *individual ultra-small* soft-magnetic particles having radii of ~50 nm (t of few tens of nm). Cobalt nanoparticles grown by means of Focused Electron Beam Induced Deposition (FEBID) of Co have been used for this purpose. Our particles are substantially smaller than those analyzed in the abovementioned works. For this reason, they yield bi-stability of both the VS and the QSD configuration at zero applied field with the VS being the ground state. To demonstrate this, the stabilization of flux closure magnetic structures at room temperature has been verified by electron holography. Magnetization measurements have been performed by directly growing individual cobalt nanoparticles on the surface of different nano-Superconducting Quantum Interference Devices (nanoSQUIDs).[23,24] NanoSQUIDs based on low temperature superconductors have proved to be very efficient for the study of nanoscopic magnetic objects.[8,25] Our devices, on the other hand, are made of the high critical temperature and high critical field superconductor $YBa_2Cu_3O_7$ (YBCO), patterned by focused ion beam milling and based on submicron grain boundary Josephson junctions.[26,27] By measuring the magnetic flux (Φ) captured by the SQUID nanoloop while sweeping the external magnetic field, we are able to distinguish the nucleation and annihilation of a flux-closure (vortex) state. Such process has been observed at different temperatures allowing us to infer the magnitude of the energy barriers separating the QSD and the VS and their field-dependence. For this purpose, we fit simultaneously the temperature-dependent critical fields for vortex nucleation and annihilation over a broad temperature range between 300 mK up to 70 K.

1. NanoSQUID characteristics and measurement setup

Three nanoSQUID sensors (labeled SQ1, SQ2 and SQ3) were fabricated as described in ref. 15. A Scanning Electron Microscope (SEM) image of SQ1 can be seen in Fig. 1a after deposition of the cobalt nanoparticle. The nanoSQUIDs exhibit non-hysteretic current–voltage characteristics within the whole range of temperatures studied here ($0.3 \text{ K} < T < 70$ K). These devices reach maximum critical currents of $I_c \sim 550$–950 μA at low temperatures, decreasing to ~100–150 μA at 70 K. SQUIDs are operated in flux locked loop mode thanks to the possibility of coupling magnetic flux to the nanoloop through a constriction patterned nearby (indicated in Fig. 1a top). The mutual inductance between this constriction and the nanoSQUID loop is measured experimentally giving $M = 0.44\Phi_0$/mA, $0.48\Phi_0$/mA and $0.65\Phi_0$/mA for SQ1, SQ2 and SQ3,

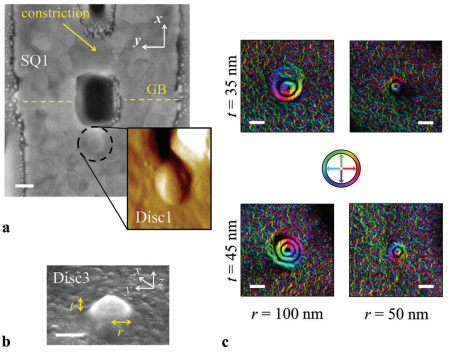

Fig. 1 (a) SEM image of Disc1 deposited on SQ1. The dashed circle highlights the position of the nanoparticle whereas dashed lines indicate the grain boundary (GB). The inset shows the corresponding AFM image of the particle. (b) SEM image of Disc3 approximated to a semi-sphere with semi-axis (r, r, t). (c) Electron holography images of few representative cobalt nanoparticles showing the presence of flux-closure ground states. The color scale in the middle represents the direction of the magnetic flux. Scale bar is 100 nm in all panels.

This journal is © The Royal Society of Chemistry 2020

Published on 07 January 2020. Downloaded by UNIVERSITAET TUEBINGEN on 6/21/2020 5:53:58 AM.

respectively (Φ_0 is the magnetic flux quantum). The temperature-dependence of M is also characterized experimentally for each device as described in ref. 15. These values allow us to convert the nanoSQUID output voltage into units of magnetic flux.

SQ1 and SQ2 are mounted in a ^{3}He refrigerator with base temperature of 0.3 K operated together with a split-coil superconducting vector magnet. SQ3 is mounted on a variable temperature insert with minimum temperature of 1.4 K operated with a superconducting magnet. This insert also includes a rotator coupled to the sample holder. These two approaches, *i.e.*, vector magnet and rotator, allow us to align the externally applied magnetic field parallel to the nanoSQUID substrate surface and perpendicular to the grain boundary's plane (x direction in Fig. 1a) with resolution better than 0.1°. Under such circumstances, the coupling of the external field to both, the nanoloop and the Josephson junctions, is minimized. As demonstrated in ref. 15 and 28, the devices are fully operative in external magnetic fields up to 1 T and temperatures up to 80 K.

2. Nanoparticle growth and electron holography measurements

The fabrication of polycrystalline cobalt nanoparticles is described in ref. 15 and briefly summarized here. We use a dual-beam system from FEI (model Helios 600). The working principle of FEBID is similar to chemical vapour deposition assisted by an electron beam. The latter allows imaging the region of interest prior to deposition. In this way, the final structure can be located at precise positions with a resolution of about ~10 nm. The precursor gas $Co_2(CO)_8$ is supplied close to the region of interest using a gas injection needle so that the $Co_2(CO)_8$ molecules decompose as the electron beam is scanned over the surface of the sample. An amorphous material containing carbon, oxygen and nanometric crystals of cobalt is obtained. The resulting cobalt purity (60 ± 10 at%) is determined *in situ* by energy dispersive X-ray spectroscopy and depends directly on the current used during deposition. The latter is kept at 25 pA to guarantee good spatial resolution. As it can be seen in Fig. 1b, the resulting particles are semi-spherical with semi-axis (r, r, t). As demonstrated in ref. 15, the effective magnetic thickness (t_{mag}) is lower than the geometrical thickness t. This is due to the formation of a ~20–25 nm-thick dead/paramagnetic cobalt layer in the first stage of the growth process as well as surface oxidation. t_{mag} can be estimated by nanoSQUID magnetometry. For this purpose we combine the measured nanoSQUID signal when the particle is in the saturated state and numerical simulations of the coupling factor between the nanoparticle and the SQUID nanoloop. We refer the reader to ref. 15 and 27 for more details about the calculation of the coupling factor.

To confirm the stabilization of flux-closure states we perform electron holography experiments using the dedicated Hitachi HF-3300 (I2TEM-Hitachi) transmission electron microscope. Electron holography is a high-sensitivity magnetic imaging technique that provides qualitative and quantitative magnetic information of isolated ferromagnetic nanostructures with nanometric resolution by retrieving the phase shift of the electron-beam plane wave after it passes through the sample and around it.[29–31] The spatial variation of the electron phase shift is given by the Aharonov–Bohm phase shift.[32] It is proportional to the sum of the 3D electrostatic potential, plus the magnetic vector potential parallel to the electron beam direction (z), respectively called the "electric phase shift" and the "magnetic phase shift". The later is proportional the projection of the in-plane component of the magnetic induction B_x and B_y. Subtracting the electric phase shift part from the total phase shift image allows mapping the local in-plane magnetization by imaging the projection of the magnetic flux lines.

For these experiments, we grow different cobalt nanoparticles with 50 nm < r < 250 nm and 10 nm < t < 45 nm. Particles are located around the perimeter of rectangular holes made on a 50 nm-thick SiN membrane. In Fig. 1c, we display magnetic flux line images for representative nanoparticles with $t \geq 35$ nm. Thinner nanoparticles produced noisy images or no magnetic signal due to the too weak magnetic induction of such thin material that electron holography cannot resolve. A circulation configuration of the magnetic lines around the nanoparticle center indicates a VS of the magnetization. This remanent state was observed both in as-prepared condition (magnetization state created during the FEBID deposition) and after saturating the nanoparticle with a strong perpendicular magnetic field (along z-direction). Therefore, electron holography experiments confirm that the VS is the ground state of the nanoparticles.

Finally, three cobalt nanoparticles (labeled Disc1, Disc2 and Disc3) have been deposited directly on the surface of the three YBCO nanoSQUIDs (SQ1, SQ2 and SQ3). Disc3 (Fig. 1b) is deposited at the constriction where the coupling to the nanoSQUID is maximized[15] whereas Disc1 and Disc2 are deposited on the opposite side of the nanoloop. A SEM and an Atomic Force Microscopy (AFM) image corresponding to Disc1 can be seen in Fig. 1a. We highlight that Disc1 is fabricated under the same growth conditions and is, therefore, nominally identical to the particle shown in the upper right panel of Fig. 1c. The external magnetic field is applied along the x direction. r and t are estimated from the SEM and AFM measurements whereas t_{mag} is estimated from the nanoSQUID measurements as described in ref. 15. The resulting values are given in Table 1.[33]

Table 1 Particle radius (r) and thickness (t) determined from the SEM and AFM images and estimated effective magnetic thickness (t_{mag})

	r (±5 nm)	t (±5 nm)	t_{mag} (nm)
Disc1	50	35	21 ± 5
Disc2	100	35	20 ± 3
Disc3	65	50	25 ± 4

Published on 07 January 2020. Downloaded by UNIVERSITAET TUEBINGEN on 6/21/2020 5:53:58 AM.

3. Magnetization measurements and numerical simulations

Hysteresis curves $\Phi(H)$ are obtained by sweeping the external bias magnetic field H and measuring the flux Φ threading the SQUID nanoloop. Two typical hysteresis curves obtained at T = 10 K for Disc1 and Disc3 can be seen in Fig. 2a (top panels). Here, we plot the magnetic flux coupled to the nanoSQUIDs in units of the flux quantum Φ_0. The apparent curvature (positive for Disc1 and negative for Disc3) is still under investigation. A similar phenomenon is observed in all devices studied so far and is attributed to the non-perfect alignment of the external magnetic field with respect to the Josephson junctions' plane.

We now analyze in more detail the hysteresis loop of Disc1. At large positive (negative) magnetic fields the stray field produced by the particle is maximum (minimum). This can be understood as the nanoparticle is in the QSD state, with most spins pointing along the external magnetic field (x direction) and, therefore, coupling the maximum (minimum) amount of flux to the nanoSQUID. As the magnitude of the external magnetic field $+H$ ($-H$) is reduced to zero, the hysteresis curve does not exhibit any step indicating that the QSD state is preserved at remanence. As the magnitude of the magnetic field is increased in the opposite direction, *i.e.*, $-H$ ($+H$), a flux closure (vortex) state is nucleated at H_n^- (H_n^+) as evidenced by the abrupt decrease of the stray field created by the nanoparticle. If the field $-H$ ($+H$) is further increased, the vortex will move perpendicularly to the external field[34] up to its final annihilation at H_a^- (H_a^+). The presence of a few minor steps subsequent to vortex nucleation can be attributed to the nucleation of intermediate states or, most likely, the presence of pinning sites that distort the vortex path. This interpretation is supported by the reduction of minor steps at larger temperatures (*cf.* section 4 and Fig. 4). A similar behavior is found in the case of Disc2 (see Fig. 6f in ref. 15 label #5) and Disc3, although the presence of intermediate steps is much more severe.

We highlight the differences between the hysteresis loops shown here and the canonical vortex-mediated magnetization reversal hysteresis loop.[34] In the latter, coercivity approaches zero with a large initial magnetic susceptibility at H = 0. This indicates that the particle is in the VS with the QSD state being prohibited. Usually, hysteretic lobes are found at high magnetic fields stemming from the vortex annihilation and nucleation. In contrast, our nanoparticles remain in the QSD state when sweeping the field through zero. This is a signature of bi-stability of the QSD and VS configurations at zero field and is a consequence of the exceptionally small size of these particles.

The critical dimensions for QSD or VS stabilization in semi-spherical particles can be calculated numerically. We use for this purpose the finite element micromagnetic simulation package Nmag,[35] which allows to solve the Landau–Lifshitz–Gilbert equation for the specific geometry under study. The use of a finite-element discretisation method is particularly important here due to the small size of the nanoparticles. In the simulations, we neglect any contribution from magneto-crystalline anisotropy due to the polycrystalline nature of Co-FEBID. We set different initial micromagnetic configurations at zero applied field, *i.e.*, in-plane and out-of-plane saturated states and a flux-closure vortex state. We then let the system relax and calculate the total energy of each resulting state. By varying the particle dimensions, we obtain the distinct stability regions plotted in Fig. 3 (shaded). These are similar to numerical and analytical results obtained for cylindrical discs.[36] Within region I, the VS is the ground state of the particle with the QSD configuration being unstable. Regions II and III correspond to an in-plane and out-of-plane QSD ground state, respectively (with the VS being unstable). Interestingly, I′ and II′ are regions of bi-stability. I′ corresponds to a vortex ground state and a metastable QSD configuration whereas the opposite occurs in region II′. Within the bi-stability regions, decreasing the bias field after saturating the magnetization does not promote the nucleation of a VS.[5] As a matter of fact, numerical simulations predict a square-shaped hysteresis loop for particles lying on regions I′ and II′.

For comparison, in Fig. 3 we plot the measured radius r and effective magnetic thickness t_{mag} corresponding to three

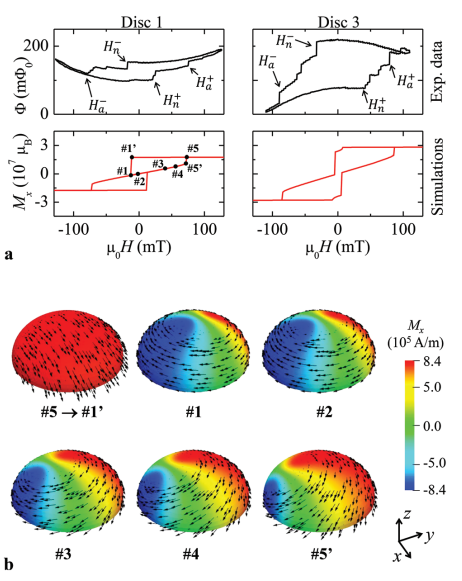

Fig. 2 Hysteresis loops of Co particles. (a) (top) Typical experimental hysteresis loops $\Phi(H)$ measured at T = 10 K and (bottom) numerical simulations $M_x(H)$ for Disc1 and Disc3. Top panels also show the definitions for the nucleation and annihilation fields. (b) Numerically simulated spatially-resolved magnetization for Disc1 at selected applied fields as indicated in panel a (bottom left). Color coding represents the magnetization along x (direction of the applied field) whereas arrows indicate the magnetization direction.

This journal is © The Royal Society of Chemistry 2020

Published on 07 January 2020. Downloaded by UNIVERSITAET TUEBINGEN on 6/21/2020 5:53:58 AM.

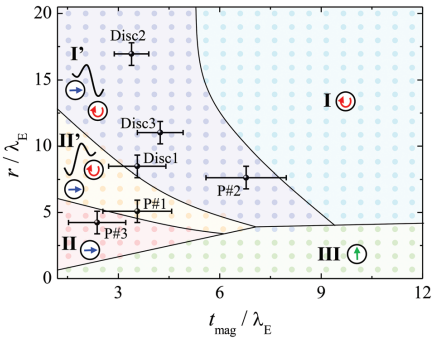

Fig. 3 Numerically calculated stability diagram for QSD and VS stabilization in semi-spherical particles (with an exchange length $\lambda_E \sim 5.9$ nm for Co-FEBID). Colored scatter indicate the points where the simulations were performed. These allow us to differentiate five stability regions (shaded). I and I′ are characterized by a vortex ground state (red curled arrow), II and II′ correspond to an in-plane ground state (blue horizontal arrow) and III corresponds to an out-of-plane ground state (green vertical arrow). Metastable configurations are also indicated schematically within each region. Solid lines are a guide to the eye. Experimental data corresponding to Disc1, Disc2, Disc3, P#1, P#2 and P#3 are shown. Particles studied by electron holography are not shown as their effective magnetic thicknesses cannot be determined.

Co-FEBID nanoparticles studied in ref. 15, *i.e.*, P#1, P#2 and P#3, and the nanoparticles studied here, *i.e.*, Disc1, Disc2 and Disc3. We highlight that P#1, P#2 and P#3 exhibited square-shaped hysteresis loops. Accordingly, these particles lye in regions II′, I′ and II, respectively. Notably, Disc1, Disc2 and Disc3 are all found in the bi-stability region I′. However, within this region, it is theoretically not possible to nucleate a VS by decreasing the bias field after saturating the magnetization. This is particularly striking in case of Disc1 that lies very close to the boundary with region II′. To the best of our knowledge, Disc1 is among the smallest nanoparticles in which a vortex has been observed to be nucleated and annihilated experimentally.[6,37,38]

Numerical simulations and experiments can come to an agreement by breaking the rotational symmetry of the nanoparticles. In this way, the experimentally measured hysteresis loops, *cf.* Fig. 2a (top panels), can be reproduced numerically by introducing a small uniaxial anisotropy parameter K_u (along the *x*-direction). The latter can have many different origins. For example, deviations from the perfect spherical shape yielding a preferred magnetization axis from magnetostatic origin. Another possibility is the existence of a net effective magnetocrystalline anisotropy (from the bulk or the substrate/surface interfaces) or magnetoelastic anisotropy. Numerical simulations are performed setting the saturation magnetization and exchange stiffness constant to $M_s = 0.6 \times 1.4$ MA m^{-1} and $A = 0.6 \times 25$ pJ m^{-1},[39] respectively. Here, the factor 0.6 reflects the reduced purity of FEBID cobalt.[40] For the anisotropy constant we choose $K_u \sim 2$ kJ m^{-3} as a reasonable value. This is estimated as $K_u = U_0/V_{mag}$ using the energy barriers (U_0) and magnetic volumes (V_{mag}) determined in ref. 15 for P#1 and P#2. To mimic the particular shape of the nanoparticles we use a semi-sphere with semi-axis (r, r, t_s). The resulting numerically calculated magnetization averaged along the *x*-direction M_x is shown in Fig. 2a (bottom panels) using $t_s = 36$ nm for Disc1 and $t_s = 27$ nm for Disc2. This simple model captures the main characteristic of the vortex-assisted magnetization reversal measured experimentally. Including few nm-sized pinned regions in the simulated nanoparticles yields the appearance of several steps ensuing vortex nucleation. These steps are similar to those observed experimentally but come at the cost of including too many degrees of freedom in the model.

4. Temperature-dependence of the vortex critical fields

In order to investigate the energy barriers involved in the processes of vortex nucleation and annihilation, we perform magnetization measurements at variable temperature. A total number of 30–50 hysteresis loops are measured at each temperature. Some representative loops obtained at given temperatures can be seen in Fig. 4 for Disc1 and Disc3. Data corresponding to Disc2 are shown in Fig. 6f from ref. 15 (with the label #5). In case of Disc1, the presence of minor steps subsequent to vortex nucleation is reduced as temperature is increased. These steps are attributed to the pinning and depin-

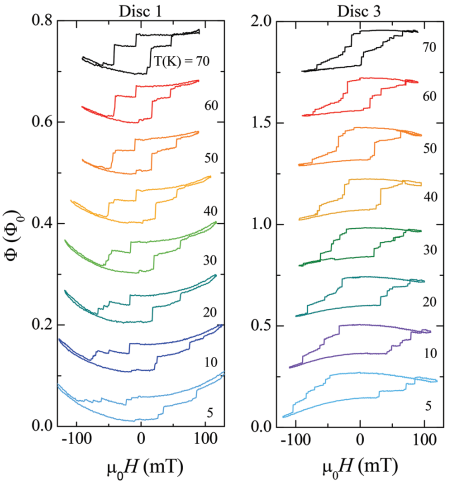

Fig. 4 Typical experimental hysteresis loops obtained at different temperatures for Disc1 and Disc3. Curves are vertically offset for clarity.

Published on 07 January 2020. Downloaded by UNIVERSITAET TUEBINGEN on 6/21/2020 5:53:58 AM.

ning of the vortex core as it moves through the nanoparticle driven by the magnetic bias field. Material defects, ubiquitous in Co-FEBID nanoparticles,[15,16] lose their pinning capacity at larger temperatures yielding the observed reduction of minor steps. We also observe that both $|H_n^{\pm}|$ and $|H_a^{\pm}|$ decrease as temperature is increased for all three nanoparticles. This is typically found for thermally assisted activation processes over an energy barrier. This can be better seen by analyzing the temperature dependence of the mean nucleation and annihilation fields defined as

$$H_n(T) = (\langle H_n^- \rangle - \langle H_n^+ \rangle)/2,$$
$$H_a(T) = (\langle H_a^+ \rangle - \langle H_a^- \rangle)/2. \quad (1)$$

Here, $\langle H_n^{\pm} \rangle$ and $\langle H_a^{\pm} \rangle$ are obtained after averaging the experimentally measured values of $H_n^{\pm}$ and $H_a^{\pm}$, respectively, over 30–50 hysteresis curves at each temperature. The resulting $H_{n/a}(T)$ curves for Disc1 and Disc3 can be seen in Fig. 5.

These data can be interpreted within the Néel-Brown model of magnetization reversal.[41,42] Here, we assume that an energy barrier exist for vortex nucleation (U_n) and annihilation (U_a). Near the vortex nucleation/annihilation critical fields, we approximate the field-dependence of these energy barriers as

$$U_{n/a} = U_0 \left(1 - \frac{H - H_{off}}{H^0_{n/a} - H_{off}}\right)^{\alpha}. \quad (2)$$

With our definition, U_0 is the energy barrier at the offset field $H = H_{off}$ such that $U_a(H_{off}) = U_n(H_{off}) = U_0$ (see Fig. 6b, point #3). $H^0_{a/n}$ is the nucleation/annihilation field at $T = 0$ K and α is a generalized exponent.

The temperature and field sweeping rate-dependence of $H_{a/n}$ can be obtained from the model of Kurkijärvi[43–45] giving

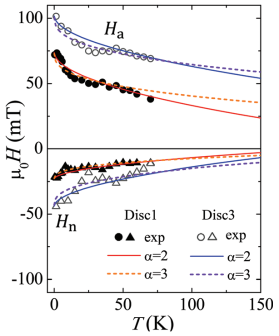

Fig. 5 Temperature dependence of the mean nucleation and annihilation fields calculated as defined in the text for Disc1 and Disc3. Dots are the experimental data. Lines are the fits to eqn (3) using the parameters shown in Table 2.

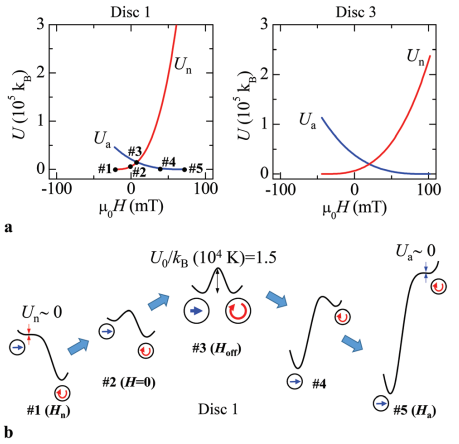

Fig. 6 (a) Field dependence of the energy barriers for vortex nucleation and annihilation calculated with eqn (2) and fitting parameters from Table 2 with α = 3 (solid lines). (b) Schematic representation of the energy landscape corresponding to Disc1 for different values of the magnetic field as indicated in panel a (left). Notice that these are the same field values at which spatially resolved maps of the magnetization are shown in Fig. 2b.

$$\mu_0 H_{n/a} = \mu_0 H_{off} + \mu_0 \left(H^0_{n/a} - H_{off}\right) \times \left\{1 - \left[\frac{k_B T}{U_0} \ln\left(\frac{\pm cT}{\nu}\right)\right]^{1/\alpha}\right\}, \quad (3)$$

where $\tau_0 = 10^{-10}$ s is an attempt time, k_B is the Boltzmann constant and ν is the magnetic field sweeping rate (ν = 4.5 mT s^{-1} and 8.3 mT s^{-1} for Disc1 and Disc3, respectively). Additionally, $c = (H^0_{n/a} - H_{off})k_B/\tau_0 \alpha U_0 \varepsilon^{\alpha-1}$ with $\varepsilon = 1 - H_{n/a}/H^0_{n/a}$.

The experimentally measured $H_a(T)$ and $H_n(T)$ curves are fitted simultaneously by eqn (3). The generalized exponent α can be, in principle, different for the processes of vortex nucleation and annihilation. In order to keep a low number of fitting parameters, we assume a single α value and we fix $H^0_{n/a}$ to the experimental fields measured at the minimum temperatures (given in Table 2). In this way, the only fitting parameters are H_{off}, U_0 and α. Simultaneous fitting is only possible for $\alpha \geq 2$. The resulting parameters obtained for α = 2 and α = 3 (solid

Table 2 Fitting parameters for Disc1 and Disc3

	$\mu_0 H^0_n$ (mT)	$\mu_0 H^0_a$ (mT)	$\mu_0 H_{off}$ (mT)	U_0/k_B ($\times 10^4$ K)	α
Disc1	−23	74	5	0.6	2
	−23	74	8	1.5	3
Disc3	−44	102	20	0.9	2
	−44	102	20	2.0	3

This journal is © The Royal Society of Chemistry 2020

Published on 07 January 2020. Downloaded by UNIVERSITAET TUEBINGEN on 6/21/2020 5:53:58 AM.

and dashed lines in Fig. 5, respectively) are summarized in Table 2.

The obtained energy barriers are in good agreement with values given in the literature for small size nanodiscs of permalloy, having an exchange length $\left(\lambda_E = \sqrt{2A/\mu_0 M_S^2} \sim 5\,\text{nm}\right)$ similar to that of Co-FEBID ($\lambda_E \sim 5.9$ nm). For example, Melkov *et al.* estimated $U_n(H = 0)/k_B \sim 4.7 \times 10^3$ K for permalloy discs with $r = 150$ nm and $t = 14$ nm.[18] The latter compares well with $U_n(H = 0)/k_B \sim 6 \times 10^3$ K obtained for Disc1 and $U_n(H = 0)/k_B \sim 6.5 \times 10^3$ K obtained for Disc3.

From these fitting parameters it is also possible to infer the nature of the ground state magnetization configuration at zero applied bias field (*cf.* point #2 in Fig. 6b). Positive H_{off} values indicate a vortex ground state in both particles at $H = 0$. This is confirmed by the electron holography experiments performed at room temperature, where flux-closure states were observed. The fact that nanoSQUID and electron holography measurements yield QSD and VS at zero bias field, respectively, is due to the different temperatures at which these experiments are performed. At room temperature, particles need only few milliseconds to relax towards the vortex ground state. However, this process becomes immeasurably long at low temperatures and the particle remains trapped in the QSD metastable state.

5. Field-dependence of the energy barriers

We can now calculate the field-dependence of the energy barriers for vortex nucleation and annihilation. For this purpose, we insert the fitting parameters corresponding to $\alpha = 3$ (*cf.* Table 2) into eqn (2) and plot the resulting $U_a(H)$ and $U_n(H)$ curves in Fig. 6a (solid lines). We highlight that eqn (2) is a good approximation only for field values close to the critical fields. However, this representation will help us to understand the processes of vortex nucleation and annihilation.

Let us focus on the results obtained for Disc1, assuming that the particle resides at $T = 0$ K. In order to facilitate understanding of the process, in Fig. 2b we plot a few space-resolved magnetization maps at selected field values numbered in panel a (bottom left). At large positive magnetic fields the cobalt nanoparticle is in the ground QSD state (#5 in Fig. 2b). If we decrease the field reaching the nucleation field (#1′), the energy barrier for vortex nucleation U_n becomes zero and the magnetic vortex nucleates (#1). This situation is schematically depicted in Fig. 6b point #1. If we now increase again the magnetic field, the vortex core will move along the y direction as shown in the series #1 → #2 → #3 in Fig. 2b. This translates into an increase of U_n while U_a decreases steadily up to the point at which the QSD and VS are degenerate [$U_0 = U_n(H_{off}) = U_a(H_{off}) = 1.5 \times 10^4 k_B$ K, *cf.* point #3 in Fig. 6b]. If we continue increasing the magnetic field, the particle will remain "trapped" in the metastable VS [*e.g.*, #4 in Fig. 2b and 6b]. Once the annihilation field is reached at #5′, the energy barrier for vortex annihilation U_a will equal zero so that the transition into the QSD state will take place (#5). The situation changes slightly at larger temperatures. Under these circumstances, the nanoparticle might gain enough thermal energy to overcome the energy barrier at field values prior to H_a. The same happens with the waiting time. If we repeat the measurements sweeping the external magnetic field at a much slower rate, the particle will have a larger probability of escaping the metastable VS before #5 is reached.

6. Conclusions

We have studied the occurrence of field-driven vortex nucleation and annihilation in *individual ultra-small* ferromagnetic particles by YBCO nanoSQUID magnetometry. The high sensitivity and broad operating field and temperature range of YBCO nanoSQUIDs has been key for this purpose. Based on the simultaneous analysis of the vortex nucleation and annihilation fields as a function of temperature, we demonstrate that particles are bi-stable at zero applied field, with the VS being the ground state. This has been also verified by electron holography experiments performed at room temperature. Interestingly, particles lie very close to the limit of QSD formation, being among the smallest nanoparticles in which a vortex has been observed to be nucleated and annihilated experimentally.[6,37,38]

YBCO nanoSQUID measurements also enable us to estimate the magnitude of the energy barriers separating the QSD and the VS and their field dependence. The latter has been approximated by a modified power-law around the critical field with generalized exponent $\alpha \geq 2$. This contrasts with most semiempirical models in which $\alpha = 3/2$, evidencing the need to further develop the theory of vortex energy barriers. In addition, details on the microscopic configuration prior to the field-driven vortex nucleation and annihilation processes remain obscure. This topic is of utmost importance in order to understand the thermal and temporal stability of noncollinear and other nontrivial spin textures, *e.g.*, vortices or skyrmions, confined in ultra-small ferromagnets. Controlling and manipulating magnetic units below the 100 nm range is paramount for their integration into nanoscopic spintronic and magnonic devices.[2,3,46]

Conflicts of interest

There are no conflicts to declare.

Acknowledgements

This work was partly funded through the Spanish MINECO (MAT2015-73914-JIN and MAT2015-64083-R), the Aragón Regional Government through project E09_17R (*Construyendo Europa desde Aragón*), the European Union Seventh Framework Program under Grant Agreement 312483-ESTEEM2 (Integrated Infrastructure Initiative–I3) and the COST action NANOCOHYBRI (Grant No. CA 16218). B. M. acknowledges funding by the German Academic Scholarship Foundation,

Published on 07 January 2020. Downloaded by UNIVERSITAET TUEBINGEN on 6/21/2020 5:53:58 AM.

and J. Lin acknowledges funding by the Chinese Research Council (CRC). E. S. acknowledges the French National Research Agency under the "*Investissement d'Avenir*" program reference no. ANR-10-EQPX-38-01. We acknowledge K. Guslienko for fruitful discussions and the use of Servicio General de Apoyo a la Investigación-SAI, Universidad de Zaragoza.

References

1 O. Fruchart and A. Thiaville, *C. R. Phys.*, 2005, **6**, 921–933.
2 V. S. Pribiag, I. N. Krivorotov, G. D. Fuchs, P. M. Braganca, O. Ozatay, J. C. Sankey, D. C. Ralph and R. A. Buhrman, *Nat. Phys.*, 2007, **3**, 498–503.
3 S. Wintz, V. Tiberkevich, M. Weigand, J. Raabe, J. Lindner, A. Erbe, A. Slavin and J. Fassbender, *Nat. Nanotechnol.*, 2016, **11**, 948–953.
4 D.-H. Kim, E. A. Rozhkova, I. V. Ulasov, S. D. Bader, T. Rajh, M. S. Lesniak and V. Novosad, *Nat. Mater.*, 2009, **9**, 165–171.
5 R. V. Verba, D. Navas, A. Hierro-Rodriguez, S. A. Bunyaev, B. A. Ivanov, K. Y. Guslienko and G. N. Kakazei, *Phys. Rev. Appl.*, 2018, **10**, 031002.
6 M. Goiriena-Goikoetxea, K. Y. Guslienko, M. Rouco, I. Orue, E. Berganza, M. Jaafar, A. Asenjo, M. L. Fernández-Gubieda, L. Fernández Barquín and A. García-Arribas, *Nanoscale*, 2017, **9**, 11269–11278.
7 K. L. Metlov and K. Y. Guslienko, *J. Magn. Magn. Mater.*, 2002, **242–245**, 1015–1017.
8 W. Wernsdorfer, K. Hasselbach, D. Mailly, B. Barbara, A. Benoit, L. Thomas and G. Suran, *J. Magn. Magn. Mater.*, 1995, **145**, 33–39.
9 T. Shinjo, T. Okuno, R. Hassdorf, K. Shigeto and T. Ono, *Science*, 2000, **289**, 930–932.
10 H. F. Ding, A. K. Schmid, D. Li, K. Y. Guslienko and S. D. Bader, *Phys. Rev. Lett.*, 2005, **94**, 157202.
11 J. Li, J. Shi and S. Tehrani, *Appl. Phys. Lett.*, 2001, **79**, 3821–3823.
12 H. Shima, V. Novosad, Y. Otani, K. Fukamichi, N. Kikuchi, O. Kitakamai and Y. Shimada, *J. Appl. Phys.*, 2002, **92**, 1473–1476.
13 R. H. Victora, *Phys. Rev. Lett.*, 1989, **63**, 457–460.
14 W. Wernsdorfer, B. Doudin, D. Mailly, K. Hasselbach, A. Benoit, J. Meier, J. P. Ansermet and B. Barbara, *Phys. Rev. Lett.*, 1996, **77**, 1873–1876.
15 M. J. Martínez-Pérez, B. Müller, D. Schwebius, D. Korinski, R. Kleiner, J. Sesé and D. Koelle, *Supercond. Sci. Technol.*, 2017, **30**, 024003.
16 M. J. Martínez-Pérez, J. Pablo-Navarro, B. Müller, R. Kleiner, C. Magén, D. Koelle, J. M. de Teresa and J. Sesé, *Nano Lett.*, 2018, **18**, 7674–7682.
17 J. A. J. Burgess, D. C. Fortin, J. E. Losby, D. Grombacher, J. P. Davis and M. R. Freeman, *Phys. Rev. B: Condens. Matter Mater. Phys.*, 2010, **82**, 144403.
18 G. A. Melkov, Y. Kobljanskyj, V. Novosad, A. N. Slavin and K. Y. Guslienko, *Phys. Rev. B: Condens. Matter Mater. Phys.*, 2013, **88**, 220407.
19 J. Ferré, Dynamics of the magnetization reversal: from continuous to patterned ferromagnetic films, in *Spin Dynamics in Confined Magnetic Structures*, Springer, Heidelberg, 2001.
20 G. Mihajlović, M. S. Patrick, J. E. Pearson, V. Novosad, S. D. Bader, M. Field, G. J. Sullivan and A. Hoffmann, *Appl. Phys. Lett.*, 2010, **96**, 112501.
21 J. P. Davis, D. Vick, J. A. J. Burgess, D. C. Fortin, P. Li, V. Sauer, W. K. Hiebert and M. R. Freeman, *New J. Phys.*, 2010, **12**, 093033.
22 G. N. Kakazei, M. Ilyn, O. Chubykalo-Fesenko, J. Gonzalez, A. A. Serga, A. V. Chumak, P. A. Beck, B. Laegel, B. Hillebrands and K. Y. Guslienko, *Appl. Phys. Lett.*, 2011, **99**, 052512.
23 C. Granata and A. Vettoliere, *Phys. Rep.*, 2016, **614**, 1–69.
24 M. J. Martínez-Pérez and D. Koelle, *Phys. Sci. Rev.*, 2017, **2**, 20175001.
25 L. Embon, Y. Anahory, Ž. Jelić, E. O. Lachman, Y. Myasoedov, M. E. Huber, G. P. Mikitik, A. V. Silhanek, M. V. Milošević, A. Gurevich and E. Zeldov, *Nat. Commun.*, 2017, **8**, 85.
26 T. Schwarz, R. Wölbing, C. F. Reiche, B. Müller, M. J. Martínez-Pérez, T. Mühl, B. Büchner, R. Kleiner and D. Koelle, *Phys. Rev. Appl.*, 2015, **3**, 044011.
27 J. Nagel, K. B. Konovalenko, M. Kemmler, M. Turad, R. Werner, E. Kleisz, S. Menzel, R. Klingeler, B. Büchner, R. Kleiner and D. Koelle, *Supercond. Sci. Technol.*, 2011, **24**, 015015.
28 T. Schwarz, J. Nagel, R. Wölbing, M. Kemmler, R. Kleiner and D. Koelle, *ACS Nano*, 2013, **7**, 844–850.
29 D. Reyes, N. Biziere, B. Warot-Fonrose, T. Wade and C. Gatel, *Nano Lett.*, 2016, **16**, 1230–1236.
30 L. A. Rodríguez, C. Bran, D. Reyes, E. Berganza, M. Vázquez, C. Gatel, E. Snoeck and A. Asenjo, *ACS Nano*, 2016, **10**, 9669–9678.
31 E. Snoeck, R. E. Dunin-Borkowski, F. Dumestre, P. Renaud, C. Amiens, B. Chaudret and P. Zurcher, *Appl. Phys. Lett.*, 2003, **82**, 88–90.
32 Y. Aharonov and D. Bohm, *Phys. Rev.*, 1959, **115**, 485–491.
33 Disc1 and Disc2 correspond to particles #4 and #5 in ref. 10, respectively. There, the estimation of t_{mag} was done assuming that the particles are cylindrical yielding lower values of the magnetic thickness, *i.e.*, 11 and 10 nm, respectively.
34 K. Y. Guslienko, V. Novosad, Y. Otani, H. Shima and K. Fukamichi, *Phys. Rev. B: Condens. Matter Mater. Phys.*, 2001, **65**, 024414.
35 T. Fischbacher, M. Franchin, G. Bordignon and H. Fangohr, *IEEE Trans. Magn.*, 2007, **43**, 2896–2898.
36 K. L. Metlov and Y. Lee, *Appl. Phys. Lett.*, 2008, **92**, 112506.
37 J. Mejía-López, D. Altbir, P. Landeros, J. Escrig, A. H. Romero, I. V. Roshchin, C.-P. Li, M. R. Fitzsimmons,

 This journal is © The Royal Society of Chemistry 2020

Published on 07 January 2020. Downloaded by UNIVERSITAET TUEBINGEN on 6/21/2020 5:53:58 AM.

X. Batlle and I. K. Schuller, *Phys. Rev. B: Condens. Matter Mater. Phys.*, 2010, **81**, 184417.
38 R. K. Dumas, K. Liu, C.-P. Li, I. V. Roshchin and I. K. Schuller, *Appl. Phys. Lett.*, 2007, **91**, 202501.
39 M. Grimsditch, E. E. Fullerton and R. L. Stamps, *Phys. Rev. B: Condens. Matter Mater. Phys.*, 1997, **56**, 2617–2622.
40 D. Wolf, L. A. Rodriguez, A. Béché, E. Javon, L. Serrano, C. Magen, C. Gatel, A. Lubk, H. Lichte, S. Bals, G. V. Tendeloo, A. Fernández-Pacheco, J. M. D. Teresa and E. Snoeck, *Chem. Mater.*, 2015, **27**, 6771–6778.
41 L. Néel, *Ann. Geophys.*, 1949, **5**, 99–136.
42 W. F. Brown, *Phys. Rev.*, 1963, **130**, 1677–1686.
43 J. Kurkijärvi, *Phys. Rev. B: Solid State*, 1972, **6**, 832–835.
44 A. Garg, *Phys. Rev. B: Condens. Matter Mater. Phys.*, 1995, **51**, 15592–15595.
45 L. Gunther and B. Barbara, *Phys. Rev. B: Condens. Matter Mater. Phys.*, 1994, **49**, 3926–3933.
46 K. Schultheiss, R. Verba, F. Wehrmann, K. Wagner, L. Körber, T. Hula, T. Hache, A. Kákay, A. A. Awad, V. Tiberkevich, A. N. Slavin, J. Fassbender and H. Schultheiss, *Phys. Rev. Lett.*, 2019, **122**, 097202.

Publication 3

Reproduced with permission from J.X Lin et al., Nanoscale 12, 5658-5668 (2020). © 2020 The Royal Society of Chemistry.

Nanoscale

PAPER

View Article Online
View Journal | View Issue

Published on 19 February 2020. Downloaded by UNIVERSITAET TUEBINGEN on 6/20/2020 2:56:29 PM.

Check for updates

Cite this: *Nanoscale*, 2020, **12**, 5658

$YBa_2Cu_3O_7$ nano superconducting quantum interference devices on MgO bicrystal substrates

Jianxin Lin,[a] Benedikt Müller,[a] Julian Linek,[a] Max Karrer,[a] Malte Wenzel,[a] Maria José Martínez-Pérez,[b,c] Reinhold Kleiner[a] and Dieter Koelle[*a]

We report on nanopatterned $YBa_2Cu_3O_{7-\delta}$ (YBCO) direct current superconducting quantum interference devices (SQUIDs) based on grain boundary Josephson junctions. The nanoSQUIDs are fabricated by epitaxial growth of 120 nm-thick films of the high-transition temperature cuprate superconductor YBCO *via* pulsed laser deposition on MgO bicrystal substrates with 24° misorientation angle, followed by sputtering of d_{Au} = 65 nm thick Au. Nanopatterning is performed by Ga focused ion beam (FIB) milling. The SQUID performance is comparable to devices on $SrTiO_3$ (STO), as demonstrated by electric transport and noise measurements at 4.2 K. MgO has orders of magnitude smaller dielectric permittivity than STO; *i.e.*, one may avoid Au as a resistively shunting layer to reduce the intrinsic thermal flux noise of the nanoSQUIDs. However, we find that the Au layer is important for avoiding degradation during FIB milling. Hence, we compare devices with different d_{Au} produced by thinning the Au layer *via* Ar ion milling after FIB patterning. We find that the reduction of d_{Au} yields an increase in junction resistance, however at the expense of a reduction of the critical current and increase in SQUID inductance. This results in an estimated thermal flux noise that is almost independent of d_{Au}. However, for two devices on MgO with 65 nm-thick Au, we find an order of magnitude lower low-frequency excess noise as compared to nanoSQUIDs on STO or those on MgO with reduced d_{Au}. For one of those devices we obtain with bias-reversal readout ultra-low flux noise of ~175 $n\Phi_0$ $Hz^{-1/2}$ down to ~10 Hz.

Received 12th December 2019,
Accepted 19th February 2020

DOI: 10.1039/c9nr10506a

rsc.li/nanoscale

Superconducting quantum interference devices (SQUIDs) are the most sensitive magnetic flux detectors known so far. SQUIDs are capable of measuring a wide range of physical parameters with unequaled sensitivity, which makes them suitable for a large variety of applications, *e.g.* in metrology, geophysics or medical diagnostics.[1–5] During the last decade, research on strongly miniaturized SQUIDs – microSQUIDs or nanoSQUIDs – has gained much interest, mainly with the aim of improving the spatial resolution for scanning SQUID microscopy[6–8] and for measuring the magnetic moments of very small spin systems.[9–13]

The miniaturization of the SQUID loop reduces the SQUID inductance L and hence the spectral density of flux noise S_Φ of the SQUID in the thermal white noise limit.[14,15] Impressively low rms flux noise $S_\Phi^{1/2}$ down to ~50 $n\Phi_0$ $Hz^{-1/2}$ (Φ_0 is the magnetic flux quantum) has been obtained at the temperature T = 4.2 K for Pb[16] and Nb[17] nanoSQUIDs and for nanoSQUIDs based on the cuprate superconductor $YBa_2Cu_3O_7$ (YBCO).[18] For the detection of the magnetization reversal of magnetic nanoparticles (MNPs) at ~10 nm distance from the SQUID loop, such low rms flux noise values translate into a spin sensitivity $S_\mu^{1/2} = S_\Phi^{1/2}/\phi_\mu$ that can be below ~1 μ_B $Hz^{-1/2}$.[16] Here, μ_B is the Bohr magneton, and ϕ_μ is the coupling factor, *i.e.*, the flux Φ coupled to the SQUID by the stray field of a magnetic dipole divided by its moment μ.

The vast majority of micro and nanoSQUIDs is based on conventional metallic superconductors (*e.g.*, Al, Pb, Nb) with two Josephson junctions (JJs) intersecting the dc SQUID loop. Typically the JJs are made from Dayem bridges, *i.e.*, narrow constrictions (cJJs) in single layer devices[19–22] which are patterned either by electron beam lithography and subsequent ion milling or directly by focused ion beam (FIB) milling with Ga ions. For studies on MNPs, their placement close to one of the cJJs yields optimum coupling, as ϕ_μ increases with decreasing width of the constriction.[23,24] The advantages of cJJs are their relatively easy fabrication and weak sensitivity to magnetic fields. Drawbacks of cJJs are (i) the difficulty to control their electric properties, as those are very sensitive to the precise geometry of the constriction (including edge damage effects), (ii) the need to use very thin films, often with thicknesses well below the London penetration depth λ_L, which

[a]*Physikalisches Institut – Experimentalphysik II and Center for Quantum Science (CQ) in LISA*[+]*, University of Tübingen, Auf der Morgenstelle 14, 72076 Tübingen, Germany. E-mail: koelle@uni-tuebingen.de*
[b]*Instituto de Ciencia de Materiales de Aragón and Departamento de Física de la Materia Condensada, CSIC-Universidad de Zaragoza, 50009 Zaragoza, Spain*
[c]*Fundación ARAID, Avda. de Ranillas, 50018 Zaragoza, Spain*

This journal is © The Royal Society of Chemistry 2020

Published on 19 February 2020. Downloaded by UNIVERSITAET TUEBINGEN on 6/20/2020 2:56:29 PM.

comes with a large kinetic inductance contribution, and (iii) the appearance of thermal hysteresis in the current I *vs.* voltage V curve (IVCs). Attempts to improve the cJJ technology are, *e.g.*, the use of thick electrodes connected by thin constrictions (variable thickness nanobridges),[25] high-resolution patterning by Ne FIB,[26] or the development of *in situ* tailored weak links and nanoSQUIDs *via* current-induced atom migration.[27,28] Alternative JJ technologies use proximized JJs, *e.g.* with carbon nanotubes[29] or metals.[30] Also a more conventional sandwich-type trilayer superconductor–insultor–superconductor (SIS) or superconductor–normal conductor–superconductor (SNS) Nb technology has been successfully developed for the creation of sub-micron JJs, yielding low-noise nanoSQUIDs.[17,31–34]

As compared to conventional superconductors, the cuprate superconductor YBCO offers nanoSQUID operation up to much higher temperature and magnetic field, due to the high transition temperature $T_c \approx 90$ K and huge upper critical field B_{c2} of at least tens of Tesla. Due to the peculiar properties of the cuprate superconductors – in particular their very small coherence length and sensitivity to defects of sizes down to the atomic scale – the reliable fabrication of JJs and SQUIDs with reproducible properties is challenging.[35] Also, due to the requirement of epitaxial growth of YBCO films on lattice matched substrates, the fabrication of low-noise multilayer devices, as used with SIS or SNS JJs is challenging.[36] Hence, in most cases YBCO SQUIDs are fabricated as single layer devices, and most commonly used JJ types are grain boundary (GB) Josephson junctions (GBJJs).[37]

YBCO nanoSQUIDs have been less intensively developed and studied so far.[13] Devices with cJJs have been produced either by direct Ga FIB milling[38] or by electron beam lithography combined with Ar ion milling.[39] In both studies, the YBCO was covered with Au serving as a protection layer during milling; this however reduces the JJ resistance and hence the voltage-to-flux transfer function, which makes it difficult to detect and exploit the intrinsic SQUID sensitivity by conventional single-stage readout.[40] In Arpaia *et al.*[39] an rms flux noise below $\sim 1\ \mu\Phi_0\ \mathrm{Hz}^{-1/2}$ has been achieved. To overcome the problem of low JJ resistance, very recently SQUIDs with ultrathin YBCO films without Au on top have been reported with improved rms flux noise down to $<450\ n\Phi_0\ \mathrm{Hz}^{-1/2}$.[41] Very recently, the same group reported on a promising new type of cJJ, the grooved Dayem bridge, which reduces the detrimental large inductance of commonly used cJJs.[42] However, it still remains to be shown whether ultra-low flux noise nanoSQUIDs can be realized with this technique. For a recent review on transport and noise properties of YBCO nanowires and nanowire-based SQUIDs, see Trabaldo *et al.*[43] Another promising JJ technique for YBCO nanoSQUIDs is the fabrication of JJ barriers by irradiating the YBCO film with a focused He ion beam (He FIB).[44] This technique has been demonstrated to produce YBCO dc SQUIDs[45] and sub-micron wide JJs.[46] Moreover, low-noise YBCO dc SQUIDs produced by He FIB irradiation with rms flux noise down to $<500\ n\Phi_0\ \mathrm{Hz}^{-1/2}$ have been demonstrated.[47] However, this technique so far is restricted to the use of YBCO films with maximum film thickness d of ~50 nm, *i.e.*, well below $\lambda_L \approx 250$ nm for YBCO films,[48] which comes with a significant kinetic inductance contribution.

The use of YBCO bicrystal GBJJs,[35,37] *i.e.*, devices grown on bicrystal substrates, has produced probably the best performance of YBCO nanoSQUIDs so far, with rms flux noise down to $<50\ n\Phi_0\ \mathrm{Hz}^{-1/2}$ at 4.2 K.[18] Those devices are fabricated by YBCO film growth on $SrTiO_3$ (STO) bicrystal substrates with [001]-tilt GB and 24° misorientation angle, and they are covered *in situ* with a Au layer. The Au layer provides a resistive shunt for the YBCO GBJJs, which is required to obtain non-hysteretic IVCs at 4.2 K. Nanopatterning is done by Ga FIB milling. It has been demonstrated that this process provides sub-micron wide GBJJs without suppression of the critical current density j_0 down to JJ widths of ~80 nm.[49] Operation of such YBCO nanoSQUIDs up to magnetic fields $B = 3$ T (ref. 50) and $T = 80$ K (ref. 51) has been demonstrated. Such devices have been successfully used for studies of magnetization reversal of individual Fe and Co nanowires[18,52] and Co MNPs.[51]

For a dc SQUID described by the resistively and capacitively shunted junction model, the thermal white noise $S_{\Phi,w}$ in the limit of small thermal fluctuations scales as $S_{\Phi,w} \propto k_B TL/I_0R$.[14,15] Here, I_0 is the noise-free critical current per junction, R is the resistance per junction and k_B is the Boltzmann constant. So, to reduce the flux noise, one would like to have an as large as possible characteristic voltage $V_c \equiv I_0R$. However, due to the need of the Au layer on top of YBCO as a resistive shunt, obviously V_c is reduced. At $T = 4.2$ K, we typically obtain $V_c \approx$ 0.1–1 mV for YBCO GBJJs on STO bicrystals with 24° misorientation angle, if they are covered with ~60 nm thick Au.[24,49] For comparison, similar GBJJs without Au shunt yield V_c values at 4.2 K up to several mV.[37]

The hysteresis in the IVCs of unshunted YBCO GBJJs on STO at 4.2 K has been attributed to the significant contribution of stray capacitance from the STO substrate due to its very high dielectric permittivity $\varepsilon \sim 10^4$.[53] Therefore, it seems to be highly promising to use an alternative bicrystal substrate material with lower ε. If such a material comes also with smaller microwave losses than in STO, its use could also be promising for microwave applications. Currently, the only commercially available option is the use of MgO bicrystals, with $\varepsilon \sim 10$ for MgO. Despite its large 9% lattice mismatch with YBCO, single-crystal MgO is still a popular substrate for the growth of high-quality YBCO thin films due to its low dielectric loss, its thermal expansion coefficient being similar to that of YBCO, and low cost. Various studies revealed the appearance of 45° in-plane misoriented YBCO grains, depending on surface topology and surface contamination.[54–56] Such an in-plane misorientation can cause significantly reduced critical current density of the YBCO films and deterioration of SQUID performance. However, with properly adjusted surface treatment, surface milling and film growth processes, YBCO GBJJs based on milled steps in single crystal MgO substrates, so-called step-edge junctions (SEJJs), have been steadily improved until today.[57,58] Also, various reports have been published on cuprate GBJJs fabricated on MgO bicrystals.[37,59,60] However to

Published on 19 February 2020. Downloaded by UNIVERSITAET TUEBINGEN on 6/20/2020 2:56:29 PM.

the best of our knowledge, a viable process for the fabrication of submicron-wide YBCO GBJJs, neither on MgO bicrystals nor on MgO step edges, and their implementation in micro- or nanoSQUIDs has been achieved so far.

In this paper, we report on the development of a submicron YBCO GBJJ technology based on MgO bicrystal substrates and nanopatterning by Ga FIB milling. We achieved single in-plane orientation within each of the two grains and fabricated several devices with the same layout as for YBCO nanoSQUIDs on STO bicrystals. We demonstrate successful Ga FIB patterning without detrimental charging effects, that are a much more severe issue with MgO substrates as compared to STO, and without degradation of V_c. We present our attempts to further enhance V_c by thinning or entirely removing the Au layer on top of YBCO and show the evolution of the electric transport and noise properties with variable Au thickness.

I. YBCO thin film growth and structural characterization

We grow *c*-axis oriented YBCO films epitaxially on lattice-matched substrates, such as (001) STO or (001) MgO, by pulsed laser deposition (PLD). Similar processes were used for growth on STO and MgO bicrystal substrates with symmetric (±12°) [001]-tilt boundary, *i.e.*, with a misorientation angle $2\theta = 24°$ ($\theta = 12°$) [*cf.* Fig. 1(a)]. For details of the growth process of our YBCO thin films on STO and of their structural and electric transport properties see *e.g.* ref. 50, 61, and 62.

As mentioned already above, for the growth of YBCO on MgO, due to the large lattice mismatch, one has to carefully characterize the crystal structure and optimize the deposition process, in particular to ensure single in-plane orientation of the films. The crystal structure of our YBCO films was investigated by X-ray diffraction (XRD), using a 4-circle PhilipsX'Pert diffractometer. By performing θ–2θ, ω and φ scans, we characterized the *c*-axis, out-of-plane and in-plane epitaxial growth, respectively. For the devices presented in this paper, we confirmed *c*-axis orientation of the YBCO films both on STO and MgO. From rocking curves of the (005) Bragg peak of the YBCO films we determined full width half maximum (FWHM) values of 0.13° for the film grown on STO (chip 2) at substrate temperature T_s = 780 °C and 0.16° for the film grown on MgO (chip 1) at T_s = 775 °C. To investigate the in-plane grain orientation, we performed (103)-plane XRD φ-scans for YBCO films deposited on MgO bicrystals. Fig. 1(b) and (c) shows such φ-scans for YBCO films deposited at T_s = 775 °C and 805 °C, respectively. For the film deposited at T_s = 775° [Fig. 1(b)], the XRD data yield peaks at 0° ± θ, 90° ± θ, 180° ± θ and 270° ± θ, reflecting the fourfold symmetry of the crystal lattice and rotation of the crystallographic axes by ±θ across the GB. This result shows that YBCO grows in single in-plane orientation with YBCO[100]//MgO[100] on both grains. For comparison, the YBCO film grown at T_s = 805° [Fig. 1(c)] yields additional peaks in the XRD φ-scans that are displaced by 45°. This indicates that at slightly higher T_s a mixed in-plane orientation

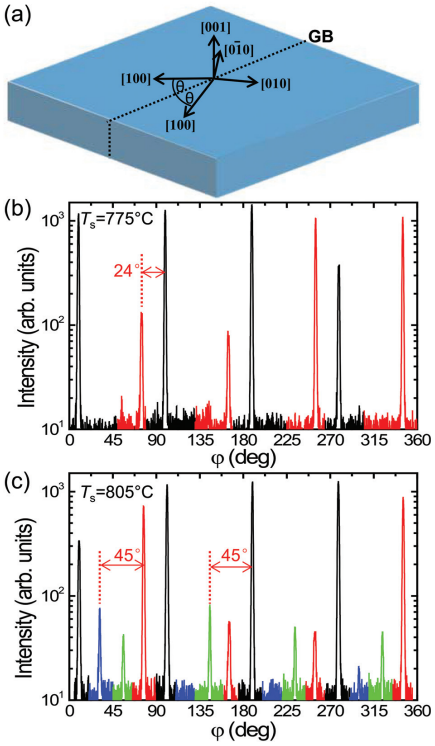

Fig. 1 On the orientation of YBCO films grown epitaxially on MgO bicrystal substrates: (a) Schematic view of the symmetric [001]-tilt MgO bicrystal substrate with crystallographic orientations. (b) and (c) YBCO (103) plane XRD φ-scans for films deposited at different substrate temperature T_s.

with 45° grain boundaries appears, *i.e.*, some grains also have the epitaxial relation YBCO[100]//MgO[110]. These results show that with optimized deposition parameters, we can grow *c*-axis oriented YBCO films with single in-plane orientation also on MgO bicrystals. Our YBCO films on both, MgO and STO substrates typically have $T_c \approx 90$ K.

II. Device fabrication and layout

For the fabrication of nanoSQUIDs, we first grow by PLD epitaxial YBCO films either on STO or MgO bicrystal substrates with 24° misorientation angle, as described in section 1. The *c*-axis-oriented YBCO films with single in-plane orientation on both halfs of the bicrystal substrates have a thickness $d \approx$ 120 nm; an optimization study[24] revealed optimum spin sensi-

This journal is © The Royal Society of Chemistry 2020

Published on 19 February 2020. Downloaded by UNIVERSITAET TUEBINGEN on 6/20/2020 2:56:29 PM.

tivity for this choice of d. After YBCO deposition, a d_{Au} = 65 nm thick Au film is deposited by electron-beam evaporation, *in situ*.

For the definition of coarse structures we use photolithography, followed by Ar ion milling (with 300 eV beam energy) to pattern 16 microbridges with 8 μm width, which are straddling the GB, *i.e.*, forming wide JJs. Those bridges are connected to large contact pads for wire bonding voltage and current leads for 4-point measurements. For some of the devices, we mount a shadow mask that covers almost the entire chip, leaving only one of the 8 μm wide bridges in the vicinity of the GB unprotected, and then use Ar ion milling to thin down the Au layer partially, or to entirely remove the Au layer.

Subsequently, single selected microbridges are patterned into nanoSQUIDs by FIB with 30 keV Ga ions in a dual beam FIB system. We note that charging effects during scanning electron microscopy (SEM) imaging and Ga FIB milling of devices on MgO are much more pronounced as compared to devices on STO. We attribute this to the fact that MgO is an insulator which has a high secondary electron yield.[63] In earlier attempts, we just connected the YBCO thin film structures with bonded aluminum wires in order to avoid charging effects: it turned out that this scheme works well for devices on bicrystal STO, but not on MgO. This prevented us from properly adjusting the Ga ion beam focus, *i.e.*, from high-resolution Ga FIB milling of devices on MgO. This problem has been solved by covering most of the chip surface with conducting carbon tape to provide improved electrical grounding of the YBCO thin film structures, which in turn significantly decreases the charging effect.

Fig. 2(a) presents a schematic view of the nanoSQUID chip layout on a bicrystal substrate. Fig. 2(b) shows a SEM image of a YBCO nanoSQUID (SQUID 5) on a MgO bicrystal (chip 1). At the position where the lithographically defined 8 μm wide YBCO bridge crosses the GB, the Ga FIB was used to narrow the bridge and mill a hole to form a dc SQUID. We note that after Ar ion milling, a groove in the substrate along the GB is easily visible in the SEM images. This is quite different to devices on STO bicrystals, where the GB is hardly visible and can only be located *via* some nano defects that align along the GB [*cf.* lower right inset in Fig. 3(a)]. In this respect, it is easier to fabricate nanoSQUIDs on bicrystal MgO as compared to bicrystal STO. The size of the SQUID hole is 220 nm × 380 nm, the widths of the two GBJJs intersecting the SQUID loop are W_{J1} = 260 nm and W_{J2} = 280 nm and their length is L_J = 380 nm. Furthermore, we use the Ga FIB to cut a slit perpendicular to the GB (from the right in Fig. 2(b)) towards the GB. With this process step, we define a constriction of width W_c

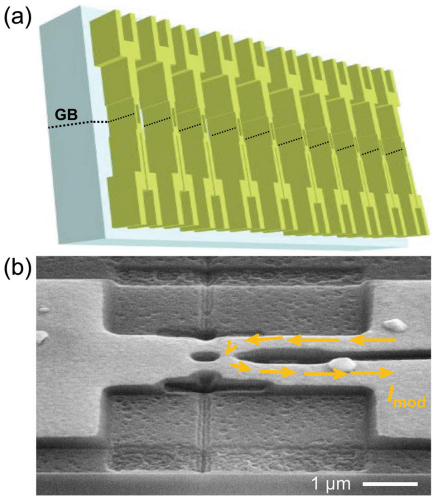

Fig. 2 (a) Schematic view of the chip layout. (b) SEM image of a YBCO nanoSQUID covered with Au (SQUID 5) on a MgO bicrystal substrate. The arrows indicate the flow of the modulation current I_{mod}.

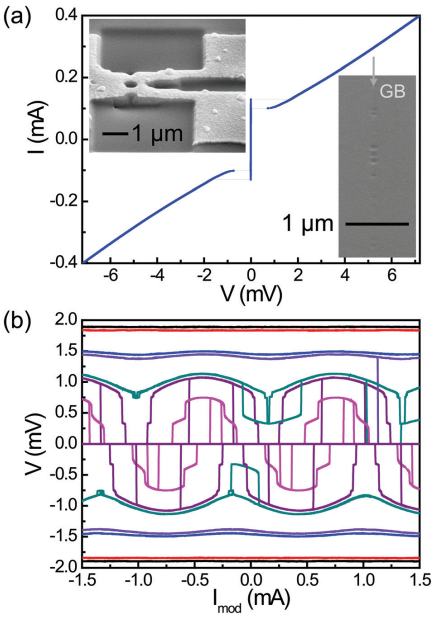

Fig. 3 Transport characteristics of SQUID S1 (on STO) with d_{Au} = 0. (a) Hysteristic IVC; I_{mod} was adjusted to obtain maximum critical current. Upper left inset: SEM image of the SQUID after FIB milling. Lower right inset: SEM image of nano defects aligned along the GB in STO bicrystal substrate at a location where YBCO has been removed by Ar ion milling. (b) $V(I_{mod})$ curves, measured with different bias currents; $|I_b|$ = 16.6… 110 μA (in 15.6 μA steps).

Published on 19 February 2020. Downloaded by UNIVERSITAET TUEBINGEN on 6/20/2020 2:56:29 PM.

Table 1 Summary of geometric and electric nanoSQUID parameters as defined in the text. Chip 1 and 3 are based on a MgO bicrystal substrate and chip 2 on a STO bicrystal substrate

Chip	Device	W_{J1} (nm)	W_{J2} (nm)	W_c (nm)	L_c (nm)	L_J (nm)	d_{Au} (nm)	$2I_0$ (μA)	$R/2$ (Ω)	V_c (mV)	M (pH)	L (pH)	β_L	Γ (10^{-3})	$S_{\Phi,w,calc}^{1/2}$ ($n\Phi_0$ $Hz^{-1/2}$)
3	SQUID 4	300	330	280	280	520	65	715	1.1	0.79	1.17	4.9	1.7	0.5	43
1	SQUID 5	260	280	220	380	480	65	378	1.5	0.57	1.30	6.2	1.1	0.9	51
1	SQUID 7	240	245	200	300	385	45	187	6.6	1.23	1.91	11	1.0	1.9	44
1	SQUID 10	200	210	210	250	375	20	127	14	1.77	3.51	16	1.0	2.8	44
1	SQUID 9	220	230	150	420	480	0	66	23	1.51	3.83	17	0.5	5.4	44
2	SQUID S1	180	220	200	250	400	0	130	22	2.86	1.76	17	1.1	2.7	37

and length L_c in the SQUID loop. By applying a modulation current I_{mod} through this constriction (indicated as arrows in Fig. 2(b)), we can modulate the magnetic flux Φ in the SQUID, to ensure operation at the optimum flux bias point and to enable SQUID readout in a flux-locked loop (FLL).[40]

We fabricated ten nanoSQUIDs on two MgO bicrystals (chip 1 and chip 3) and three nanoSQUIDs on a STO bicrystal (chip 2). The geometry of all devices discussed in this paper (*cf.* Table 1) is similar to the one shown in Fig. 2(b).

III. Results and discussion

For characterization of the device properties, electric transport and noise measurements are performed in an electrically and magnetically shielded environment at T = 4.2 K, *i.e.*, with the samples immersed in liquid helium. Usually, the nanoSQUIDs survive multiple cool downs and warm-ups; most importantly, one has to avoid water condensation on the chips, if they are removed from the He dewar after warm-up. If we store devices at room temperature, the critical current is reduced with time – typically by some tens of percent within one month. This degradation can be avoided by storing the nanoSQUIDs in liquid nitrogen.

We record IVCs with the modulation current I_{mod} (flux bias) adjusted to obtain the maximum critical current $I_{c,max}$ and minimum critical current $I_{c,min}$ of the SQUID. For all devices discussed below, we can neglect noise rounding of the IVCs, as the noise parameter $\Gamma \equiv 2\pi k_B T/I_0\Phi_0$ is very small ($\approx 10^{-3}$).[15] Hence, we set $I_{c,max} = 2I_0$. Moreover, from the linear part of the IVC in the voltage state, we determine the resistance of the SQUID $R_n = R/2$. Accordingly, from the IVCs we obtain $I_{c,max}R_n = I_0R = V_c$. We also record SQUID oscillations by measuring the critical current I_c of the SQUID *vs.* I_{mod}, and we measure $V(I_{mod})$ for various values of bias current I_b. From the SQUID oscillations, we determine the modulation period $I_{mod,0}$ and from this the mutual inductance $M = \Phi_0/I_{mod,0}$. From the modulation depth of I_c (I_{mod}) oscillations, we estimate the screening parameter $\beta_L \equiv 2I_0L/\Phi_0$ *via* the approximate relation $(I_{c,max} - I_{c,min})/I_{c,max} \approx 1(1 + \beta_L)$.[15] From the estimated β_L, together with the measured $I_{c,max}$ we determine L.

A. YBCO nanoSQUID on STO

For comparison, we first show electric transport data from a YBCO nanoSQUID fabricated on a symmetric $2\theta = 24°$ STO bicrystal substrate (SQUID S1 on chip 2). This device has also been fabricated with 65 nm thick Au on top of YBCO, and the Au layer has been removed by Ar ion milling prior to FIB nanopatterning. Fig. 3(a) shows an IVC (with flux bias adjusted to achieve maximum critical current $I_{c,max}$). Clearly, the IVC shows hysteristic behaviour, which we do not see for similar devices on STO that still have the Au layer on top.[18,49,50] The hysteresis in the IVC leads also to hysteresis and to switching steps in the $V(I_{mod})$ curves, as shown in Fig. 3(b). Obviously, one has to avoid such a hysteretic behavior if one wants to use conventional SQUD readout. Geometric and electrical parameters of SQUID S1 are listed in Table 1, together with parameters for YBCO nanoSQUIDs on MgO.

B. YBCO nanoSQUIDs on MgO

In the following, we present data for four YBCO nanoSQUIDs that have been fabricated on the same MgO bicrystal substrate (chip 1) and for one nanoSQUID on another MgO bicrystal substrate (chip 3). For three SQUIDs on chip 1, the Au layer was removed fully (SQUID 9) or partially (SQUID 7, SQUID 10) prior to FIB patterning. SQUID 5 on chip 1 and SQUID 4 on chip 3 was left with the 65 nm thick Au layer on top (*cf.* Table 1).

Before cutting into nanoSQUIDs, we measured 8 junctions on chip 1 with 8 μm width. Those measurements yielded critical currents I_c ranging from 2.9 to 3.6 mA, corresponding to critical current densities j_c ranging from 3.0 to 3.8 × 10^5 A cm^{-2}. These values are in the same range as obtained earlier for similar devices on STO bicrystals.[49]

Fig. 4(a) shows two nonhysteretic IVCs for SQUID 5, with flux bias adjusted to achieve maximum and minimum I_c. Fig. 4(b) shows the modulation of the critical current I_c (I_{mod}) for SQUID 5. The value of V_c = 0.57 mV, which we find for this shunted YBCO nanoSQUID on MgO, is well within the range of V_c values that have been obtained for shunted YBCO nanoSQUIDs of comparable geometry and size on STO bicrystals.[24,49] We note that prior to FIB patternig, the device (8 μm-wide GBJJ) had even a slightly smaller V_c = 0.50 mV. Moreover, SQUID 5 has $I_{c,max}$ = 378 μA, corresponding to j_c = 5.8 × 10^5 A cm^{-2}. The enhanced j_c after FIB nanopatterning follows the trend which we also observed earlier for similar devices on STO bicrystals.[49] This already demonstrates that our YBCO nanoSQUID fabrication technology has been successfully transferred to MgO bicrystals, for which we can

 This journal is © The Royal Society of Chemistry 2020

Published on 19 February 2020. Downloaded by UNIVERSITAET TUEBINGEN on 6/20/2020 2:56:29 PM.

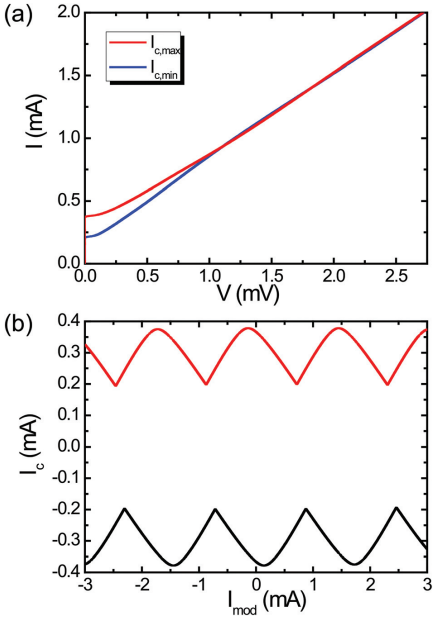

Fig. 4 Transport characteristics of SQUID 5 (on MgO) with d_{Au} = 65 nm. (a) Nonhysteretic IVCs measured with two values for I_{mod} to obtain maximum and minimum critical current. (b) Critical current I_c *vs.* I_{mod} for both bias current polarities.

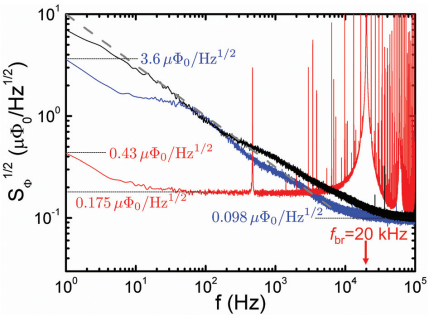

Fig. 5 Rms spectral density of flux noise $S_\Phi^{1/2}(f)$ measured in FLL mode on SQUID 5 with dc bias (blue) and bias reversal (red) and on SQUID 4 with dc bias (black), both on MgO with d_{Au} = 65 nm. The vertical arrow indicates the bias reversal frequency f_{br}. The dashed line corresponds to $S_\Phi \propto 1/f$.

expect at least similar performance as achieved up to now on STO.

To further characterize the performance of the shunted SQUID 5, we measured its intrinsic flux noise. Fig. 5 shows the rms spectral density of flux noise $S_\Phi^{1/2}(f)$ measured in FLL mode. The blue curve has been measured with dc bias and yields ultra-low thermal white noise $S_{\Phi,w}^{1/2} = 98\ n\Phi_0\ Hz^{-1/2}$, which is the second lowest value we ever measured for a high-T_c nanoSQUID. For frequencies $f \lesssim 10$ kHz, the flux noise increases with decreasing f. For comparison, the dashed line shows the ubiquitous $1/f$ noise, *i.e.*, $S_\Phi \propto 1/f$, which is typically observed for SQUIDs at low frequency. It is well known that the dominant source of $1/f$ noise comes from I_0 fluctuations in the JJs due to localized defects in the JJ barrier, and that this is particularly strong for high-T_c SQUIDs.[35] Very roughly, the blue curve follows the $1/f$ noise scaling; however clear deviations (in particular the bump-like feature around 100 Hz) are visible. This is probably not surprising, as only few defects may be present in the small (submicron-sized) JJs, which results in a superposition of a small number of Lorentzians.[18] More surprising is the fact that the overall level of this low-frequency excess noise is more than an order of magnitude lower than what we typically observe for our YBCO nanoSQUIDs on STO bicrystals.[18]

For comparison, Fig. 5 shows also the rms flux noise of SQUID 4, fabricated on a separate chip (also on MgO and with d_{Au} = 65 nm). The black curve has been measured with dc bias in FLL mode and shows a level of white noise and low-frequency excess noise, that is very similar to SQUID 5 on chip 1.

The reason for the significantly smaller low-frequency noise for the two devices on MgO is not clear yet. We can safely exclude a contribution to low-frequency excess noise due to thermally activated motion of Abrikosov vortices,[64] as the measurements (in this work and in ref. 18 on YBCO nanoSQUIDs on STO) were performed in magnetically shielded environment. It is known that ion milling of STO produces oxygen vacancies, which leads to an enhanced conductivity[65] and also to the formation of magnetic moments,[66] which can induce low-f excess noise due to fluctuating magnetic moments (spin noise).[18] However, the enhanced conductivity of oxygen-deficient STO is still quite low as compared to a conventional metal, and it should induce f-independent white Nyquist noise.[67] Moreover, magnetic moments can also be induced by the creation of oxygen defects in MgO.[68,69] However, a quantitative analysis of the possible strength of $1/f$ noise due to oxygen-vacancy-induced defects, both in STO and MgO, is not at hand. Therefore, we cannot claim that the observed reduction of low-f excess noise in our devices on MgO is due to reduced spin noise, as compared to devices on STO. The observed small low-frequency excess noise in the two YBCO nanoSQUIDs on MgO is a very encouraging result and deserves further studies to clarify the origin of a possibly systematically much lower $1/f$ noise of YBCO nanoSQUIDs on MgO bicrystals.

To remove the contribution of I_0 fluctuations to $1/f$ noise, we also performed measurements on SQUID 5 with bias reversal[40] (at frequency f_{br} = 20 kHz), shown as the red curve in

Published on 19 February 2020. Downloaded by UNIVERSITAET TUEBINGEN on 6/20/2020 2:56:29 PM.

Fig. 5.[70] We find a significant reduction of the low-frequency excess noise, with a slightly enhanced white noise level down to $f \sim 10$ Hz of $S_{\Phi,w}^{1/2} = 175\ n\Phi_0\ Hz^{-1/2}$. This result is again very encouraging, as it represents the lowest flux noise value at low frequencies which has been achieved with any high-T_c SQUID so far.[18] Even at $f = 1$ Hz, the rms flux noise is still below 0.5 $\mu\Phi_0\ Hz^{-1/2}$.

In an attempt to further improve nanoSQUID performance by increasing V_c, we investigated various ways to reduce the thickness of the Au shunt on top of YBCO or to entirely remove it. It turned out that fabrication without any Au on top of YBCO yields working devices, however, with up to an order of magnitude scattering in I_0 and R (albeit much smaller scatter in V_c) for nanoSQUIDs fabricated on the same chip. We also fabricated devices starting with YBCO/Au bilayers, and removed the Au layer after FIB milling (either by chemical wet etching or by Ar ion milling). However, this led to a full suppression of I_0. So far, only deposition of *in situ* Au on YBCO and thinning down or entire removal by Ar ion milling after prepatterning the bridges (*i.e.*, before Ga FIB patterning) produced devices with satisfactory results.

Fig. 6 shows $V(I_{mod})$ SQUID oscillations (at different I_b) of the four YBCO nanoSQUIDs on the same MgO bicrystal substrate (chip 1), with d_{Au} ranging from 65 nm to 0 (*cf.* Table 1). All four devices show non-hysteretic IVCs and continuous $V(I_{mod})$ oscillations, including SQUID 9 for which Au has been completely milled away (in contrast to SQUID S1 on the STO bicrystal discussed above, which shows hysteretic IVCs).

The evolution of electric transport parameters (*cf.* Table 1) with variation of d_{Au} is shown in Fig. 7. As expected, the resistance of the nanoSQUIDs increases strongly (by a factor of ~15) upon decreasing d_{Au}. For $d_{Au} = 0$ (SQUID 9) the value $R/2 = 23\ \Omega$ is quite comparable to $R/2 = 22\ \Omega$ for SQUID S1 on STO. Unfortunately, the envisioned improvement of SQUID performance *via* increasing R is counterbalanced by a concomitant decrease in I_0 (by a factor of ~6). Still, V_c increases slightly upon reducing d_{Au}, but only by a factor of 2 to 3. Moreover, with decreasing d_{Au} we find an increase in L and M (by a factor of ~3). This increase in inductances indicates degradation of not only the GBJJs but also of the entire YBCO film forming the SQUID loop. Most likely, this can be attributed to oxygen loss of YBCO during Ar ion milling caused by heating.

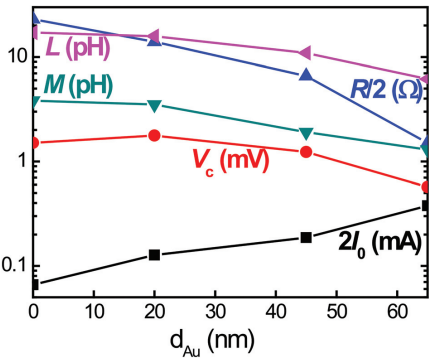

Fig. 7 Variation of SQUID parameters with Au layer thickness for SQUIDs on MgO (chip 1).

As all our devices are in the limit of weak thermal fluctuations, we can estimate the flux noise in the thermal white noise limit for $\Gamma\beta_L < 0.1$ as $S_{\Phi,w,calc} = 4(1 + \beta_L)\Phi_0 k_B TL/(I_0 R)$.[15] Corresponding values for all devices are listed in Table 1 and suggest slightly improved white flux noise for the nanoSQUIDs with reduced Au thickness. To check this, we performed noise measurements also on nanoSQUIDs 7 and 9 with reduced d_{Au}. The results are shown in Fig. 8. For comparison, we also include the noise data from SQUID 4 and 5 which were dis-

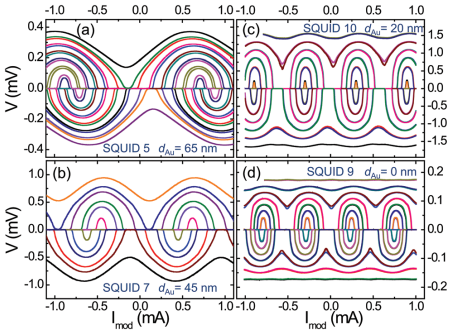

Fig. 6 $V(I_{mod})$ oscillations, measured with different bias currents for SQUIDs on MgO (chip 1). With decreasing d_{Au}, the oscillation period is decreasing, *i.e.*, M is increasing.

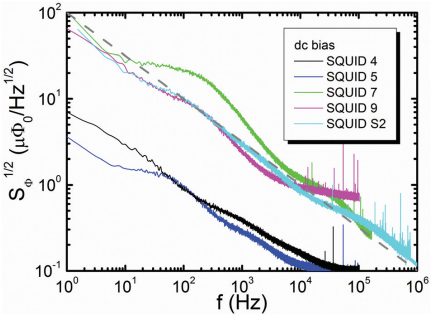

Fig. 8 Rms spectral density of flux noise $S_\Phi^{1/2}(f)$ of SQUID 4, 5, 7 and 9 (on MgO) measured in FLL mode with dc bias. For comparison, the spectrum from SQUID S2 on STO (SQUID-1 in ref. 18) is included. The dashed line corresponds to $S_\Phi \propto 1/f$.

This journal is © The Royal Society of Chemistry 2020

Published on 19 February 2020. Downloaded by UNIVERSITAET TUEBINGEN on 6/20/2020 2:56:29 PM.

cussed already above. In contrast to SQUID 4 and 5, the two other SQUIDs 7 and 9 show a much larger low-frequency excess noise. Unfortunately, this prevented us from reaching the white noise limit for SQUID 7 and 9 to compare experimental results with the theoretical prediction. Again, the bump-like features in the spectra for SQUID 7 and 9 are attributed to a superposition of a small number of Lorentzians. For comparison, in Fig. 8 we also include the noise spectrum of a YBCO nanoSQUID on a STO bicrystal substrate (denoted here as SQUID S2). This is the device for which we reported the so far lowest white noise (at 7 MHz) achieved for our YBCO nanoSQUIDs in ref. 18 (denoted there as SQUID-1). Obviously, the level of low-frequency excess noise of SQUID S2 is very comparable to the excess noise of SQUID 7 and 9.

IV. Conclusions

We have successfully developed a process for the fabrication of YBCO nanoSQUIDs on MgO bicrystal substrates. High-quality YBCO films can be grown epitaxially with single in-plane orientation on each of the two halfs of the substrate. With proper grounding, charging effects during Ga FIB milling can be avoided, which enables nanopatterning of devices with high spatial resolution.

We find that a 65 nm-thick Au layer on top of YBCO is important for the protection of devices during FIB milling. Such an Au layer has originally been used for YBCO nanoSQUIDs on STO bicrystals for resistively shunting the grain boundary Josephson junctions, as required for operation at low temperature (~4 K) without hysteresis in the *IV* characteristics. Due to the orders of magnitude smaller dielectric permittivity of MgO, as compared to STO, the Au shunt may be omitted for devices on MgO. This in turn offers the perspective to further increase the characteristic voltage $V_c = I_0R$ of the Josephson junctions *via* a substantial increase in R, with a concomitant significant improvement in the thermal white noise of the nanoSQUIDs. We produced several devices which had their Au layer either thinned down or entirely removed by Ar ion milling before FIB nanopatterning. We find that indeed R increases strongly by reducing the Au thickness. However, at the same time I_0 decreases and SQUID inductance L increases, which compensates the expected gain in SQUID sensitivity. An option for further improvement is the use of thinner Au on top of YBCO. FIB-patterned YBCO grain boundary junctions on STO, with d_{Au} = 20 nm on top, showed the tendency to develop hysteresis in the IVC.[49] This problem could be solved now with the process developed here for the fabrication of YBCO nanoSQUIDs on MgO bicrystals.

Still, we demonstrate low-noise performance of YBCO nanoSQUIDs on MgO, which is comparable to devices on STO. For two devices (on two separate chips) that have the full 65 nm Au thickness, we find an order of magnitude smaller low-frequency excess noise, as compared to devices with thinner Au or devices with full Au thickness on STO. The achieved ultra-low flux noise of ~175 $n\Phi_0$ $Hz^{-1/2}$ down to ~10 Hz for one device is highly promising, albeit the origin of the reduction in low-frequency noise has not yet been clarified; this needs further investigations.

We note that the use of MgO instead of STO substrates provides the opportunity to integrate the YBCO nanoSQUIDs into microwave circuits, due to the much lower microwave losses in MgO. This paves the way for new applications of such nanoSQUIDs, *e.g.*, for SQUID-based electron spin resonance[71–73] or for studies of magnon dynamics at characteristic timescales of nanoseconds or even below.[74,75] Furthermore, we note that by using an optimized process for removing the Au layer after FIB milling, as demonstrated very recently by Lam *et al.*,[76] and/or starting the fabrication process with a thinner Au layer on top of YBCO, it still seems possible to improve the sensitivity of such devices down to the level of single spin sensitivity.

Conflicts of interest

The authors declare no conflicts of interest.

Acknowledgements

J. Lin acknowledges funding by the China Scholarship Council. B. Müller acknowledges funding by the German Academic Scholarship Foundation. M. J. Martínez-Pérez acknowledges funding by the Spanish MICINN project MAT2015-73914-JIN. We gratefully acknowledge fruitful discussions and technical support by M. Turad and R. Löffler (LISA$^+$) and by C. Back. This work was supported by the COST action NANOCOHYBRI (CA16218).

References

1 *The SQUD Handbook Vol. I Fundamentals and Technology of SQUIDs and SQUID Systems*, ed. J. Clarke and A. I. Braginski, Wiley-VCH, Weinheim, 2004.
2 *The SQUD Handbook Vol. II Applications of SQUIDs and SQUID Systems*, ed. J. Clarke and A. I. Braginski, Wiley-VCH, Weinheim, 2006.
3 J. Gallop, SQUIDs: some limits to measurement, *Supercond. Sci. Technol.*, 2003, **16**, 1575–1582.
4 R. Kleiner, D. Koelle, F. Ludwig and J. Clarke, Superconducting QUantum interference devices: State-of-the-art and applications, *Proc. IEEE*, 2004, **92**, 1534–1548.
5 R. L. Fagaly, Superconducting quantum interference device instruments and applications, *Rev. Sci. Instrum.*, 2006, **77**, 101101.
6 J. R. Kirtley, SQUID microscopy for fundamental studies, *Physica C*, 2002, **368**, 55–65.
7 J. R. Kirtley, Prospects for imaging magnetic nanoparticles using a scanning SQUID microscope, *Supercond. Sci. Technol.*, 2009, **22**, 064008.

Published on 19 February 2020. Downloaded by UNIVERSITAET TUEBINGEN on 6/20/2020 2:56:29 PM.

8 D. Koelle, Magnetic sensors: A tip for better sensing, *Nat. Nanotechnol.*, 2013, **8**, 617–618.
9 W. Wernsdorfer, Classical and quantum magnetization reversal studied in nanometersized particles and clusters, *Adv. Chem. Phys.*, 2001, **118**, 99–190.
10 C. P. Foley and H. Hilgenkamp, Why NanoSQUIDs are important: an introduction to the focus issue, *Supercond. Sci. Technol.*, 2009, **22**, 064001.
11 W. Wernsdorfer, From micro- to nano-SQUIDs: applications to nanomagnetism, *Supercond. Sci. Technol.*, 2009, **22**, 064013.
12 C. Granata and A. Vettoliere, Nano superconducting quantum interference device: A powerful tool for nanoscale investigations, *Phys. Rep.*, 2016, **614**, 1–69.
13 M. J. Martínez-Pérez and D. Koelle, NanoSQUDs: Basics & recent advances, *Phys. Sci. Rev.*, 2017, **2**, 20175001.
14 C. D. Tesche and J. Clarke, DC SQUID: Noise and optimization, *J. Low Temp. Phys.*, 1977, **29**, 301–331.
15 B. Chesca, R. Kleiner and D. Koelle, SQUID Theory, in *The SQUD Handbook, Vol. I: Fundamentals and Technology of SQUIDs and SQUID systems*, ed. J. Clarke and A. I. Braginski, Wiley-VCH, Weinheim, 2004, ch. 2, pp. 29–92.
16 D. Vasyukov, Y. Anahory, L. Embon, D. Halbertal, J. Cuppens, L. Ne'eman, A. Finkler, Y. Segev, Y. Myasoedov, M. L. Rappaport, M. E. Huber and E. Zeldov, A scanning superconducting quantum interference device with single electron spin sensitivity, *Nat. Nanotechnol.*, 2013, **8**, 639–644.
17 M. Schmelz, A. Vettoliere, V. Zakosarenko, N. De Leo, M. Fretto, R. Stolz and C. Granata, 3D nanoSQUID based on tunnel nano-junctions with an energy sensitivity of 1.3 h at 4.2 K, *Appl. Phys. Lett.*, 2017, **111**, 032604.
18 T. Schwarz, R. Wölbing, C. F. Reiche, B. Müller, M. J. Martínez-Pérez, T. Mühl, B. Büchner, R. Kleiner and D. Koelle, Low-noise $YBa_2Cu_3O_7$ nano-SQUIDs for performing magnetization-reversal measurements on magnetic nanoparticles, *Phys. Rev. Appl.*, 2015, **3**, 044011.
19 K. Hasselbach, D. Mailly and J. R. Kirtley, Micro-superconducting quantum interference device characteristic, *J. Appl. Phys.*, 2002, **91**, 4432–4437.
20 S. K. H. Lam and D. L. Tilbrook, Development of a niobium nanosuperconducting quantum interference device for the detection of small spin populations, *Appl. Phys. Lett.*, 2003, **82**, 1078–1080.
21 A. G. P. Troeman, H. Derking, B. Borger, J. Pleikies, D. Veldhuis and H. Hilgenkamp, NanoSQUIDs based on niobium constrictions, *Nano Lett.*, 2007, **7**, 2152–2156.
22 L. Hao, J. C. Macfarlane, J. C. Gallop, D. Cox, J. Beyer, D. Drung and T. Schurig, Measurement and noise performance of nano-superconducting-quantum-interference devices fabricated by focused ion beam, *Appl. Phys. Lett.*, 2008, **92**, 192507.
23 V. Bouchiat, Detection of magnetic moments using a nano-SQUID: limits of resolution and sensitivity in near-field SQUID magnetometry, *Supercond. Sci. Technol.*, 2009, **22**, 064002.
24 R. Wölbing, T. Schwarz, B. Müller, J. Nagel, M. Kemmler, R. Kleiner and D. Koelle, Optimizing the spin sensitivity of grain boundary junction nanoSQUIDs – towards detection of small spin systems with single-spin resolution, *Supercond. Sci. Technol.*, 2014, **27**, 125007.
25 R. Vijay, J. D. Sau, M. L. Cohen and I. Siddiqi, Optimizing anharmonicity in nanoscale weak link Josephson junction oscillators, *Phys. Rev. Lett.*, 2009, **103**, 087003.
26 O. W. Kennedy, J. Burnett, J. C. Fenton, N. G. N. Constantino, P. A. Warburton, J. J. L. Morton and E. Dupont-Ferrier, Tunable Nb superconducting resonator based on a constriction nano-SQUID fabricated with a Ne focused ion beam, *Phys. Rev. Appl.*, 2019, **11**, 014006.
27 J. Lombardo, Z. L. Jelić, X. D. A. Baumans, J. E. Scheerder, J. P. Nacenta, V. V. Moshchalkov, J. Van de Vondel, R. B. G. Kramer, M. V. Milošević and A. V. Silhanek, In situ tailoring of superconducting junctions via electro-annealing, *Nanoscale*, 2018, **10**, 1987–1996.
28 W. Keijers, X. D. A. Baumans, R. Panghotra, J. Lombardo, V. S. Zharinov, R. B. G. Kramer, A. V. Silhanek and J. Van de Vondel, In situ tailoring of superconducting junctions via electro-annealing, *Nanoscale*, 2018, **10**, 21475–21482.
29 J.-P. Cleuziou, W. Wernsdorfer, V. Bouchiat, T. Ondarçuhu and M. Monthioux, Carbon nanotube superconducting quantum interference device, *Nat. Nanotechnol.*, 2006, **1**, 53–59.
30 F. Giazotto, J. T. Peltonen, M. Meschke and J. P. Pekola, Superconducting quantum interference proximity transistor, *Nat. Phys.*, 2010, **6**, 254–259.
31 J. Nagel, O. F. Kieler, T. Weimann, R. Wölbing, J. Kohlmann, A. B. Zorin, R. Kleiner, D. Koelle and M. Kemmler, Superconducting quantum interference devices with submicron Nb/HfTi/Nb junctions for investigation of small magnetic particles, *Appl. Phys. Lett.*, 2011, **99**, 032506.
32 R. Wölbing, J. Nagel, T. Schwarz, O. Kieler, T. Weimann, J. Kohlmann, A. B. Zorin, M. Kemmler, R. Kleiner and D. Koelle, Nb nano superconducting quantum interference devices with high spin sensitivity for operation in magnetic fields up to 0.5 T, *Appl. Phys. Lett.*, 2013, **102**, 192601.
33 M. J. Martínez-Pérez, D. Gella, B. Müller, V. Morosh, R. Wölbing, J. Sesé, O. Kieler, R. Kleiner and D. Koelle, Three-axis vector nano superconducting quantum interference device, *ACS Nano*, 2016, **10**, 8308–83151.
34 S. Bechstein, C. Köhn, D. Drung, J.-H. Storm, O. Kieler, V. Morosh and T. Schurig, Investigation of nanoSQUID designs for practical applications, *Supercond. Sci. Technol.*, 2017, **30**, 034007.
35 D. Koelle, R. Kleiner, F. Ludwig, E. Dantsker and J. Clarke, High-transition-temperature superconducting quantum interference devices, *Rev. Mod. Phys.*, 1999, **71**, 631–686.
36 F. Ludwig, D. Koelle, E. Dantsker, D. T. Nemeth, A. H. Miklich, J. Clarke and R. E. Thomson, Low noise $YBa_2Cu_3O_{7-x}$-$SrTiO_3$-$YBa_2Cu_3O_{7-x}$ multilayers for improved magnetometers, *Appl. Phys. Lett.*, 1995, **66**, 373–375.

 This journal is © The Royal Society of Chemistry 2020

Published on 19 February 2020. Downloaded by UNIVERSITAET TUEBINGEN on 6/20/2020 2:56:29 PM.

37 H. Hilgenkamp and J. Mannhart, Grain boundaries in high-T_c superconductors, *Rev. Mod. Phys.*, 2002, **74**, 485.
38 C. H. Wu, Y. T. Chou, W. C. Kuo, J. H. Chen, L. M. Wang, J. C. Chen, K. L. Chen, U. C. Sou, H. C. Yang and J. T. Jeng, Fabrication and characterization of high-T_c $YBa_2Cu_3O_{7-x}$ nanoSQUIDs made by focused ion beam milling, *Nanotechnology*, 2008, **19**, 315304.
39 R. Arpaia, M. Arzeo, S. Nawaz, S. Charpentier, F. Lombardi and T. Bauch, Ultra low noise $YBa_2Cu_3O_{7-\delta}$ nano superconducting quantum interference devices implementing nanowires, *Appl. Phys. Lett.*, 2014, **104**, 072603.
40 D. Drung and M. Mück, SQUID Electronics, in *The SQUD Handbook, Vol. I: Fundamentals and Technology of SQUIDs and SQUID Systems*, ed. J. Clarke and A. I. Braginski, Wiley-VCH, Weinheim, 2004, ch. 4, pp. 127–170.
41 R. Arpaia, M. Arzeo, R. Baghdadi, E. Trabaldo, F. Lombardi and T. Bauch, Improved noise performance of ultrathin YBCO Dayem bridge nanoSQUIDs, *Supercond. Sci. Technol.*, 2017, **30**, 014008.
42 E. Trabaldo, C. Pfeiffer, E. Andersson, R. Arpaia, A. Kalaboukhov, D. Winkler, F. Lombardi and T. Bauch, Grooved Dayem nanobridges as building blocks of high-performance $YBa_2Cu_3O_{7-\delta}$ SQUID magnetometers, *Nano Lett.*, 2019, **19**, 1902–1907.
43 E. Trabaldo, R. Arpaia, M. Arzeo, E. Andersson, D. Golubev, F. Lombardi and T. Bauch, Transport and noise properties of YBCO nanowire based nanoSQUIDs, *Supercond. Sci. Technol.*, 2019, **19**, 073001.
44 S. A. Cybart, E. Y. Cho, J. T. Wong, B. H. Wehlin, M. K. Ma, C. Huynh and R. C. Dynes, Nano Josephson superconducting tunnel junctions in $YBa_2Cu_3O_{7-\delta}$ directly patterned with a focused helium ion beam, *Nat. Nanotechnol.*, 2015, **10**, 598–602.
45 E. Y. Cho, M. K. Ma, C. Huynh, K. Pratt, D. N. Paulson, V. N. Glyantsev, R. C. Dynes and S. A. Cybart, $YBa_2Cu_3O_{7-\delta}$ superconducting quantum interference devices with metallic to insulating barriers written with a focused helium ion beam, *Appl. Phys. Lett.*, 2015, **106**, 252601.
46 E. Y. Cho, Y. W. Zhou, J. Y. Cho and S. A. Cybart, Superconducting nano Josephson junctions patterned with a focused helium ion beam, *Appl. Phys. Lett.*, 2018, **113**, 022604.
47 B. Müller, M. Karrer, F. Limberger, M. Becker, B. Schröppel, C. J. Burkhardt, R. Kleiner, E. Goldobin and D. Koelle, Josephson junctions and SQUIDs created by focused helium-ion-beam irradiation of $YBa_2Cu_3O_7$, *Phys. Rev. Appl.*, 2019, **11**, 044082.
48 L. Thiel, D. Rohner, M. Ganzhorn, P. Appel, E. Neu, B. Müller, R. Kleiner, D. Koelle and P. Maletinsky, Quantitative nanoscale vortex imaging using a cryogenic quantum magnetometer, *Nat. Nanotechnol.*, 2016, **11**, 677–681.
49 J. Nagel, K. B. Konovalenko, M. Kemmler, M. Turad, R. Werner, E. Kleisz, S. Menzel, R. Klingeler, B. Büchner, R. Kleiner and D. Koelle, Resistively shunted $YBa_2Cu_3O_7$ grain boundary junctions and low-noise SQUIDs patterned by a focused ion beam down to 80 nm linewidth, *Supercond. Sci. Technol.*, 2011, **24**, 015015.
50 T. Schwarz, J. Nagel, R. Wölbing, M. Kemmler, R. Kleiner and D. Koelle, Low-noise nano superconducting quantum interference device operating in tesla magnetic fields, *ACS Nano*, 2013, **7**, 844–850.
51 M. J. Martínez-Pérez, B. Müller, D. Schwebius, D. Korinski, R. Kleiner, J. Sesé and D. Koelle, NanoSQUID magnetometry of individual cobalt nanoparticles grown by focused electron beam induced deposition, *Supercond. Sci. Technol.*, 2017, **30**, 024003.
52 M. J. Martínez-Pérez, J. Pablo-Navarro, B. Müller, J. Stankievicz, R. Kleiner, C. Magén, D. Koelle, J. M. de Teresa and J. Sesé, NanoSQUID magnetometry on individual as-grown and annealed Co nanowires at variable temperature, *Nano Lett.*, 2018, **18**, 7674–7682.
53 A. Beck, A. Stenzel, O. M. Froehlich, R. Gerber, R. Gerdemann, L. Alff, B. Mayer, R. Gross, A. Marx, J. C. Villegier and H. Moriceau, Fabrication and superconducting transport properties of bicrystal grain boundary Josephson junctions on different substrates, *IEEE Trans. Appl. Supercond.*, 1995, **5**, 2192–2195.
54 H. Suzuki, Y. Fujiwara, Y. Hirotsu, T. Yamashita and T. Oikawa, In-plane orientations andgrain boundaries of $YBa_2Cu_3O_{7-x}$ thin films on (001)MgO substrates grown by metalorganic chemical vapor deposition, *Jpn. J. Appl. Phys.*, 1993, **32**, 1601–1611.
55 J. Du, S. Gnanarajan and A. Bendavid, Influence of MgO surface conditions on the in-plane crystal orientation and critical current density of epitaxial YBCO films, *Physica C*, 2004, **400**, 143–152.
56 J. Du, S. Gnanarajan and A. Bendavid, Characterization of MgO substrates for growth of epitaxial YBCO thin films, *Supercond. Sci. Technol.*, 2005, **18**, 1035–1041.
57 E. E. Mitchell and C. P. Foley, YBCO step-edge junctions with high I_cR_n, *Supercond. Sci. Technol.*, 2010, **23**, 065007.
58 E. E. Mitchell, K. E. Hannam, J. Lazar, K. E. Leslie, C. J. Lewis, A. Grancea, S. T. Keenan, S. K. H. Lam and C. P. Foley, 2D SQIF arrays using 20 000 YBCO high R_n Josephson junctions, *Supercond. Sci. Technol.*, 2016, **29**, 06LT01.
59 K. Lee and I. Iguchi, Josephson effects in $YBa_2Cu_3O_y$ grain boundary junctions on (100) MgO bicrystal substrates, *Appl. Phys. Lett.*, 1995, **66**, 769–771.
60 M. I. Faley, S. B. Mi, A. Petraru, C. L. Jia, U. Poppe and K. Urban, Multilayer buffer for high-temperature superconductor devices on MgO, *Appl. Phys. Lett.*, 2006, **89**, 082507.
61 R. Werner, C. Raisch, A. Ruosi, B. A. Davidson, P. Nagel, M. Merz, S. Schuppler, M. Glaser, J. Fujii, T. Chassé, R. Kleiner and D. Koelle, $YBa_2Cu_3O_7/La_{0.7}Ca_{0.3}MnO_3$ bilayers: Interface coupling and electric transport properties, *Phys. Rev. B*, 2010, **82**, 224509.
62 S. Scharinger, M. Turad, A. Stöhr, V. Leca, E. Goldobin, R. G. Mints, D. Koelle and R. Kleiner, Magnetic field dependence of the critical current in $YBa_2Cu_3O_{7-\delta}$/Au/Nb ramp-zigzag Josephson junctions, *Phys. Rev. B*, 2012, **86**, 144531.

Published on 19 February 2020. Downloaded by UNIVERSITAET TUEBINGEN on 6/20/2020 2:56:29 PM.

63 J. Cazaux, Charging in scanning electron microscopy "from inside and outside", *Scanning*, 2004, **26**, 181–203.
64 A. H. Miklich, D. Koelle, T. J. Shaw, F. Ludwig, D. T. Nemeth, E. Dantsker, J. Clarke, N. McN. Alford, T. W. Button and M. S. Colclough, Low frequency excess noise in $YBa_2Cu_3O_{7-x}$ dc superconducting quantum interference devices cooled in static magneticfields, *Appl. Phys. Lett.*, 1994, **64**, 3494–3496.
65 V. E. Henrich, G. Dresselhaus and H. J. Zeiger, Surface defects and the electronic structure of $SrTiO_3$ surfaces, *Phys. Rev. B*, 1978, **17**, 4908–4921.
66 I. R. Shein and A. L. Ivanosvkii, First principle prediction of vacancy-induced magnetism in non-magnetic perovskite $SrTiO_3$, *Phys. Lett. A*, 2007, **371**, 155–159.
67 J. R. Clem, Johnson noise from normal metal near a superconducting SQUID gradiometer circuit, *IEEE Trans. Magn.*, 1987, **23**, 1093–1096.
68 A. M. Ferrari and G. Pacchioni, Electronic structure of F and V centers on the MgO surface, *J. Phys. Chem.*, 1995, **99**, 17010–17018.
69 J. P. Singh and K. W. Chae, d^0 ferromagnetism of magnesium oxide, *Condens. Matter*, 2017, **2**, 36.
70 Due to technical problems, we could not perform bias reversal measurements on SQUID 4.
71 H. Toida, Y. Matsuzaki, K. Kakuyanagi, X. Zhu, W. J. Munro, K. Nemoto, H. Yamaguchi and S. Saito, Electron paramagnetic resonance spectroscopy using a direct current-SQUID magnetometer directly coupled to an electron spin ensemble, *Appl. Phys. Lett.*, 2016, **108**, 052601.
72 G. Yue, L. Chen, J. Barreda, V. Bevara, L. Hu, L. Wu, Z. Wang, P. Andrei, S. Bertaina and I. Chiorescu, Sensitive spin detection using an on-chip SQUID-waveguide resonator, *Appl. Phys. Lett.*, 2017, **111**, 202–601.
73 H. Toida, Y. Matsuzaki, K. Kakuyanagi, X. Zhu, W. J. Munro, H. Yamaguchi and S. Saito, Electron paramagnetic resonance spectroscopy using a single artificial atom, *Commun. Phys.*, 2018, **2**, 33.
74 S. Bonetti, X-ray imaging of spin currents and magnetisation dynamics at the nanoscale, *J. Phys.: Condens. Matter*, 2017, **29**, 133004.
75 F. Casola, T. van der Sar and A. Yacoby, Probing condensed matter physics with magnetometry based on nitrogen-vacancy centres in diamond, *Nat. Rev. Mater.*, 2018, **3**, 17088.
76 S. K. H. Lam, A. Bendavid and J. Du, Hot spot formation in focused-ion-beam-fabricated $YBa_2Cu_3O_{7-x}$ nanobridges with high critical current densities, *Nanotechnology*, 2019, **30**, 325301.

 This journal is © The Royal Society of Chemistry 2020

Publication 4

Nano SQUIDs from $YBa_2Cu_3O_7/SrTiO_3$ superlattices with bicrystal grain boundary Josephson junctions.
arXiv:2007.11064 [cond-mat.supr-con].

NanoSQUIDs from $YBa_2Cu_3O_7/SrTiO_3$ superlattices with bicrystal grain boundary Josephson junctions

Jianxin Lin,[1] Julian Linek,[1] Reinhold Kleiner,[1] and Dieter Koelle[1,*]

[1] *Physikalisches Institut, Center for Quantum Science (CQ) and LISA$^+$, University of Tübingen, Auf der Morgenstelle 14, 72076 Tübingen, Germany*

(Dated: July 23, 2020)

We report on the fabrication and characterization of nanopatterned dc SQUIDs with grain boundary Josephson junctions based on heteroepitaxially grown $YBa_2Cu_3O_7$ (YBCO)/ $SiTrO_3$ (STO) superlattices on STO bicrystal substrates. Nanopatterning is performed by Ga focused-ion-beam milling. The electric transport properties and thermal white flux noise of superlattice nanoSQUIDs are comparable to single layer YBCO devices on STO bicrystals. However, we find that the superlattice nanoSQUIDs have more than an order of magnitude smaller low-frequency excess flux noise, with root-mean-square spectral density $S_\Phi^{1/2} \sim 5 - 6\,\mu\Phi_0/\sqrt{\text{Hz}}$ at 1 Hz (Φ_0 is the magnetic flux quantum). We attribute this improvement to an improved microstructure at the grain boundaries forming the Josephson junctions in our YBCO nanoSQUDs.

PACS numbers: 85.25.CP, 85.25.Dq, 74.78.Na, 74.72.-h 74.25.F- 74.40.De

arXiv:2007.11046v1 [cond-mat.supr-con] 21 Jul 2020

I. INTRODUCTION

Strongly miniaturized direct current (dc) superconducting quantum interference devices (SQUIDs) with dimensions in the submicrometer range (nanoSQUIDs) are promising devices for the sensitive detection and investigation of small spin systems, as they can be used for direct detection of the magnetization reversal of individual magnetic nanoparticles (MNPs), nanotubes or nanowires[1–10] and for high-resolution scanning SQUID microscopy[11–20]. The vast majority of nanoSQUIDs developed during the last decade are based on metallic superconductors, for which their operation temperature is limited by their transition temperature T_c to below $\sim$ 10 K. Furthermore, metallic low-T_c superconductors typically have upper critical fields B_{c2} below 1 T, which also limits the magnetic field range in which nanoSQUIDs based on them can be operated[13,21]. As an alternative, the high-T_c cuprate superconductor $YBa_2Cu_3O_7$ (YBCO), with $T_c \sim 92$ K and B_{c2} well above 10 T offers the use of YBCO nanoSQUIDs for applications within a much wider range of temperature T and magnetic field B, as compared to nanoSQUIDs based on conventional metallic superconductors.

The fabrication of Josephson junctions (JJs) and SQUIDs based on cuprate superconductors is demanding, in particular due to the very small superconducting coherence length on the nanometer scale and concomitant high sensitivity of those materials to defects on the atomic scale. YBCO micro- and nanoSQUIDs are typically based on single layers of epitaxially grown films, that are eventually covered with a metallic layer (e.g. Au) for resistive shunting and protection during nanopatterning[7]. Josephson junctions in such single layer devices are based on constrictions (cJJs) with widths down to ~ 50 nm [22], that yield a root-mean-square (rms) spectral density of flux noise $S_\Phi^{1/2}$ in the thermal white noise limit down to $< 450\,\text{n}\Phi_0/\text{Hz}^{1/2}$ at $T = 18$ K (Φ_0 is the magnetic flux quantum)[23]. Another recently developed JJ type is based on creating Josephson barriers in YBCO thin films via focused ion beam (FIB) irradiation with a He ion beam[24]. Sub-micron wide He-FIB JJs[25] and nanoSQUIDs[26] have been realized, and a rms flux noise in the thermal white noise limit down to $< 500\,\text{n}\Phi_0/\text{Hz}^{1/2}$ has been achieved at $T = 4.2$ K [27]. Furthermore, grain boundary (GB) Josephson junctions (GBJJs), that are formed by epitaxial growth of YBCO on a bicrystal substrate[28], provide a well established approach for realizing YBCO nanoSQUIDs in single layer devices. The use of Ga FIB milling enables one to fabricate GBJJs down to 80 nm width[29], and operation of GBJJ based nanoSQUIDs up to $B = 3$ T [30] has been demonstrated. The optimization of the SQUID layouts[31] led to the demonstration of ultralow rms flux noise in the thermal white noise limit down to $\sim 45\,\text{n}\Phi_0/\text{Hz}^{1/2}$ at $T = 4.2$ K [32]. For a MNP placed in 10 nm-distance to a constriction in the SQUID loop, this corresponds to a spin sensitivity of $\sim 3\,\mu_\text{B}/\text{Hz}^{1/2}$ (μ_B is the Bohr magneton). Such YBCO nanoSQUIDs with bicrystal GBJJs have been used for the investigation of the magnetization reversal of Fe and Co nanowires[9,32] and Co MNPs[8,10], including e.g. the analysis of MNP switching fields over a wide T range from 300 mK up to 80 K.

A significant drawback for high-T_c cuprate SQUIDs in general is the very large amount of low-frequceny excess noise, typically scaling with frequency f as $S_\Phi \propto 1/f$ ($1/f$ noise)[33]. The dominant source of $1/f$ noise comes from critical current I_0 fluctations due to localized defects in the JJ barrier[34], which can be several orders of magnitude larger than for conventional Nb tunnel junctions[35–37]. For YBCO nanoSQUIDs with ultralow thermal white noise, this excess noise can dominate the spectral density of flux noise up to high frequencies in the MHz range[23,32]. An established procedure to suppress this $1/f$ noise contribution from I_0 fluctuations in dc SQUIDs is the application of bias reversal schemes

(including proper modulation of flux bias), which suppresses $1/f$ noise below the applied bias reversal frequency $f_{\rm br}$[38,39]. However, applying such schemes to YBCO nanoSQUIDs is a particular challenge for the SQUID readout electronics and nanoSQUID design, because very large $f_{\rm br}$ is required, and the required modulation of the flux bias points at $f_{\rm br}$ is difficult to achieve due to the small SQUID inductance L and concomitantly small mutual inductance M between a nanoSQUID and the flux modulation line.

We further note that the flux noise spectrum of YBCO nanoSQUIDs often shows a superposition of a few Lorentzians rather than a pure $1/f$ spectrum, which can be explained by the relatively small number of dominating defects in JJs with small size[23,32]. In addition we find excess $1/f$ noise in our GBJJ YBCO nanoSQUIDs, which has been attributed to the fluctuations of spins of unknown origin, most likely due to defects at the substrate/YBCO interface or at the edges of the nanopatterned structures[32]. Another open issue is the unclear origin of strong $1/f$ noise in YBCO nanoSQUIDs based on cJJs. For those devices, this excess noise has been also attributed to I_0 fluctuations, although, there is no barrier in such nanowires[23].

Obviously, the strong low-frequency excess noise in YBCO nanoSQUIDs has to be related to the defect structure in the GB barrier or in the YBCO films forming cJJs, together with possible contributions from the YBCO/substrate interface or damaged edges. Apart from optimizing thin film growth by introducing suitable buffer or cap layers[40–42], a possible solution to this problem may be the growth of multilayers (superlattices), involving epitaxially grown interlayers between YBCO films[43], to interrupt the growth of extended defects in YBCO. Such a multilayer or superlattice approach has been successfully used to significantly enhance the critical current density in YBCO films[44–47], in particular for thick films developed for high-current applications. Accordingly, the focus within this approch was on basic studies and on the improvement of pinning properties of YBCO films, often by deliberately introducing a high density of defects. Studies on $1/f$ flux noise in YBCO thin films and SQUIDs based on them, also indicated possible improvements via improved pinning properties[33]. However, so far, there is no information on the possible modification (improvement or deterioration) of $1/f$ noise from I_0 fluctuations in YBCO JJs and SQUIDs based on them, induced by the implementation of superlattice structures into the devices.

In this work, we report on the fabrication and properties of YBCO nanoSQUIDs that are based on a heteroepitaxial YBCO/STO superlattice, grown on a STO bicrystal substrate. The comparison with single layer YBCO devices of similar geometry shows, that the superlattice nanoSQUIDs yield comparable electric transport properties and comparable upper bounds to the flux noise in the thermal white noise limit. Regarding low-frequency excess noise, however, we find a strong reduction of the low-frequency noise in the superlattice nanoSQUIDs by more than one order of magnitude in rms flux noise at 1 Hz.

II. DEVICE FABRICATION AND LAYOUT

We first fabricated very thin c-axis oriented epitaxial single layer YBCO thin films by pulsed laser deposition (PLD) on (100)-oriented $SrTiO_3$ (STO) single crystal substrates. For films of thickness d_Y = 7, 17, 23 and 31 nm, we find T_c = 61, 81, 83 and 84 K, respectively (via inductive T_c measurements). Based on those results, we decided to fabricate multilayer (superlattice) devices with $d_Y \approx 30$ nm per YBCO layer, to ensure a high enough T_c.

We used PLD to grow an epitaxial YBCO/STO superlattice on a STO bicrystal substrate with a symmetric ($\pm 12°$) [001]-tilt grain boundary (GB), i.e., with a misorientation angle $2\theta = 24°$ ($\theta = 12°$). The multilayer consists of a stack of four c-axis oriented YBCO layers with $d_Y \approx 30$ nm thickness per layer, separated by three STO interlayers with 3 nm thickness per layer. The choice of the total YBCO thickness $d = 4d_Y \approx 120$ nm is based on an optimization study, that revealed optimum spin sensitivity for this choice of d.[31] For all layers, we used the same deposition parameters (substrate temperature T_s = 800 °C and oxygen partial pressure $p_{O_2} = 0.2$ mbar). For details of the growth process of our YBCO thin films on STO and of their structural and electric transport properties see e.g. Refs. [30, 48, and 49]. An in-situ evaporated 65-nm-thick Au layer on top of the YBCO/STO superlattice serves as a resistive shunt to provide nonhysteretic current-voltage characteristics (IVCs) of the grain boundary junctions formed in YBCO and as a protection layer during Ga FIB nanopatterning.[29,50]

For the characterization of the crystalline quality of the unpatterned YBCO/STO multilayer, we performed x-ray diffraction (XRD) using a 4-circle PhilipsX'Pert diffractometer. Fig. 1(a) shows a $\Theta - 2\Theta$ scan, indicating single phase c-axis oriented YBCO films. The ω scan (rocking curve), shown in the inset of Fig. 1(a), yields good alingment of the c-axis perpendicular to the substrate plane, with full-width-half-maximum (FWHM) $\sim 0.16°$. From the position of the YBCO (005) peak we extract a c-axis lattice constant of 11.69 Å, which is close to the value of fully oxygenated unstrained YBCO[51]. Fig. 1(b) shows a YBCO (103) φ-scan with diffraction peaks at $0° \pm (\theta)$, $90° \pm (\theta)$, $180° \pm (\theta)$ and $360° \pm (\theta)$, reflecting the fourfold symmetry of the crystal lattice and rotation of the crystallographic axes by $\pm\theta$ across the GB. No other peaks can be detected, which confirms in-plane epitaxial growth just according to the orientation of the STO bicrystal without misaligned grains.

After charactierization of the unpatterned YBCO/STO multilayer, we used photolithography and Ar ion milling to prepattern 16 microbridges straddling the grain boundary to create 8 μm wide

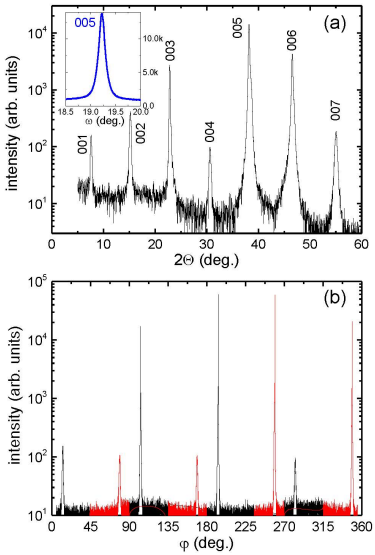

FIG. 1. XRD data of the unpatterned YBCO/STO superlattice on a STO bicrystal substrate. (a) $\Theta - 2\Theta$ scan, showing YBCO (00ℓ) Bragg peaks. Inset shows rocking curve of the (005) peak. (b) YBCO (103) plane XRD φ-scan. Black and red indicate diffraction peaks from the two grains of the bicrystal.

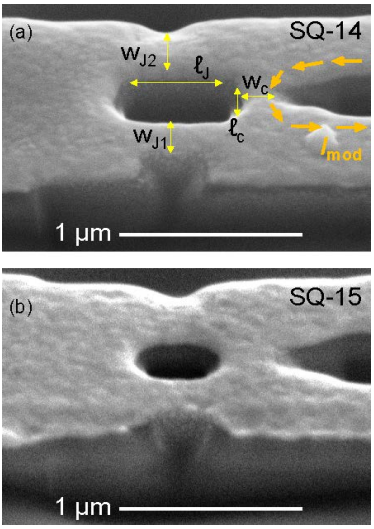

FIG. 2. SEM images of YBCO/STO superlattice nanoSQUIDs, covered with Au. The grain boundary (not visible) runs from top to bottom and intersects the SQUID hole to form two JJs ($\sim 250 - 320$ nm wide). Arrows in (a) indicate the geometric parameters as listed in Table I and the modulation current $I_{\rm mod}$ that is used to flux-bias the SQUID.

GBJJs; those will be referred to as JJ-1 to JJ-16.[28] Those bridges are connected to several-mm long and few-100 μm wide contact pads onto which Al wires are bonded as voltage and current leads for 4-point measurements.[50] Subsequently, YBCO nanoSQUIDs with similar sizes are nanopatterned into some of the 8 μm-wide GBJJs by FIB milling with 30-keV Ga ions in a dual-beam FIB system.

Fig. 2 shows scanning electron microscopy (SEM) images of two YBCO/STO multilayer nanoSQUIDs SQ-14 and SQ-15, nanopatterned into JJ-14 and JJ-15, respectively. At the position where the GB crosses the microbridge, the Ga FIB is used to define two sub-μm-wide GBJJs with width w_{Ji} $(i = 1, 2)$ and to mill the SQUID hole with size $\sim \ell_J \times \ell_c$. In addition, we use the Ga FIB to cut a slit perpendicular to the GB (from the right in Fig. 2) towards the GB, to produce a constriction with width w_c in the SQUID loop. By applying a modulation current $I_{\rm mod}$ through the constriction (indicated as arrows in Fig. 2(a)), the magnetic flux Φ in the SQUID can be modulated, to ensure SQUID operation at optimum flux bias and to perform SQUID readout in a flux-locked loop (FLL).[39] For measurements of magnetization reversal of individual MNPs, placing the MNP on top of the constriction also provides optimum coupling of signal to the nanoSQUID.[7,8]

On JJ-15 we determined from resistance vs T measurement $T_c = 87.2$ K, with a transition width $\Delta T_c \approx 0.8$ K. For SQ-15 (nanopatterned into JJ-15), we determined essentially unchanged T_c and ΔT_c after FIB patterning.

III. TRANSPORT AND NOISE PROPERTIES OF SUPERLATTICE JJS AND NANOSQUIDS

In this section, we present and discuss electric transport and noise properties measured in liquid Helium at $T = 4.2$ K in an electrically and magnetically shielded environment. We focus on two fabricated YBCO/STO superlattice nanoSQUIDs, SQ-14 and SQ-15, which were FIB-patterned from JJ-14 and JJ-15, respectively. For comparison we also show data for a single layer (SL) 120 nm-thick YBCO nanoSQUID (SQ-SL), also with a 65 nm-thick Au layer on top, with comparable lateral geometry. This SL nanoSQUID was FIB-patterned from the 8 μm-wide JJ-SL, also on a STO bicrystal substrate with misorientation angle $2\theta = 24°$.

The IVCs of JJ-14 and JJ-15, measured before FIB patterning, are shown in Fig. 3. Those were recorded in zero applied magnetic field ($H = 0$). The IVCs have

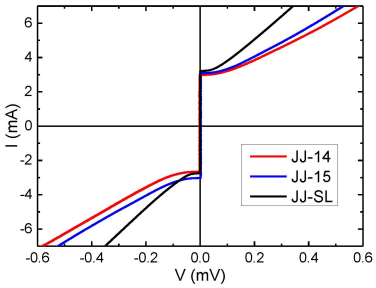

FIG. 3. IVCs (at $T = 4.2\,\mathrm{K}$ and $H = 0$) of 8-μm-wide GB-JJs in a YBCO/STO superlattice (JJ-14 and JJ-15) and in a single layer YBCO film (JJ-SL), all with Au on top.

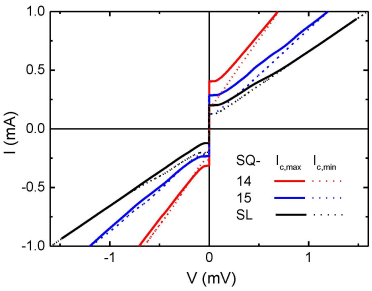

FIG. 4. IVCs of superlattice SQUIDs (SQ-14 and SQ-15) and single layer SQUID (SQ-SL). Solid (dashed) lines are recorded with I_{mod} adjusted to obtain maximum (minimum) critical current $I_{\mathrm{c,max}}$ for $I > 0$.

the typical shape described by the resistively and capacitively shunted junction (RCSJ) model,[52,53] without hysteresis. We note that the 8 μm-wide JJs are in the long junction limit, as also revealed by $I_{\mathrm{c}}(H)$ measurements (not shown). The $I_{\mathrm{c}}(H)$ curves show a slight asymmetry, which means that the maximum critical current $I_{\mathrm{c,max}}$ is not reached exactly at $H = 0$; this is the reason for the slight asymmetries in the IVCs (different critical current for opposite polarity). Hence, the $I_{\mathrm{c,max}}$ values quoted in Table I have been obtained from the maxima of the $I_{\mathrm{c}}(H)$ patterns. Values of $I_{\mathrm{c,max}}$ for both JJs are around 3 mA. Converting this into a critical current density j_{c}, by dividing by the JJ width (8 μm) and total YBCO film tickness (120 nm) yields $j_{\mathrm{c}} \approx 3 \times 10^5\,\mathrm{A/cm^2}$ (see also Table I). This is a typical value which we obtain for YBCO GBJJs of similar size, made from single layer films[29,50] and hence indicates, that the current flowing through the JJs is distributed across all four YBCO layers in the superlattice. This observation is also consistent with microstructural studies on YBCO/STO superlattices with 3 nm-thick STO layers, which showed discontinuities in the very thin STO layers[54].

With a measured resistance $R_{\mathrm{n}} \sim 0.1\,\Omega$ (which is dominated by the shunting Au layer[50]) for the two JJs, we obtain a characteristic voltage $V_{\mathrm{c}} = I_{\mathrm{c,max}} R_{\mathrm{n}} \sim 0.3\,\mathrm{mV}$ (see also Table I); this is at the lower end of the range of values of V_{c} that we observe for single layer YBCO nanoSQUIDs based on GBJJs on STO bicrystal substrates.[31] For comparison, the IVC of JJ-SL is also shown in Fig. 3; this device indeed has similar values for I_{c}, R_{n} and V_{c}; c.f. Table I. We note that values of $I_{\mathrm{c,max}}$ and R_{n} for the other 8 μm-wide JJs on the same chip with the YBCO/STO superlattice are very similar to JJ-14 and JJ-15.

Fig. 4 shows IVCs of superlattice nanoSQUIDs SQ-14 and SQ-15 and, for comparison, the IVC of the single layer nanoSQUID SQ-SL with comparable geometry. For those measurements, I_{mod} has been adjusted to yield maximum critical current $I_{\mathrm{c,max}}$ (solid lines) and minimum critical current $I_{\mathrm{c,min}}$ (dashed lines) on the positive branches.

Geometric and electrical parameters for all three SQUIDs are summarized in Table I, together with parameters from the JJs obtained before nanoSQUID patterning. Also after FIB nanopatterning, we find nonhysteretic RCSJ-type IVCs, with values for $I_{\mathrm{c,max}}$, R_{n} and V_{c} which are comparable to GBJJ nanoSQUIDs from single layer YBCO films with similar geometry.[50] We note that we observe for all nanoSQUIDs slightly larger j_{c} and V_{c} values, as compared to those obtained from the 8 μm-wide JJs. This is typical for all our YBCO nanoSQUIDs (see e.g. Ref. 29), and we attribute this to the fact, that the inhomogeneity of the GB (e.g. due to faceting[28]) is slightly reduced upon reducing the JJ width to the deep sub-μm regime.

Fig. 5 shows critical current I_{c} vs I_{mod} oscillations of all three nanoSQUIDs. From the modulation period $I_{\mathrm{mod,0}}$ we determine the mutual inductance $M = \Phi_0 / I_{\mathrm{mod,0}}$. Obviously, the mutual inductance for SQ-14 is more than a factor of two larger than for SQ-15, while SQ-SL has

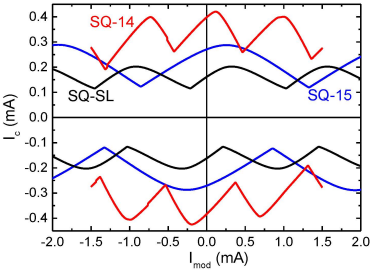

FIG. 5. Critical current I_{c} vs. I_{mod} of multilayer SQUIDs (SQ-14 and SQ-15) and single layer SQUID (SQ-SL) for both bias current polarities.

TABLE I. Summary of geometric and electric parameters of 8 μ-wide JJs and nanoSQUIDs as defined in the text. JJ-14 and JJ-15 are based on YBCO/STO superlattices, from which SQ-14 and SQ-15 was nanopatterned, respectively. JJ-SL is based on a single layer of YBCO, from which SQ-SL was nanopatterned. For all devices the total YBCO thickness is 120 nm and the Au layer on top is 65 nm thick.

device	w_{J1} (nm)	w_{J2} (nm)	w_c (nm)	ℓ_c (nm)	ℓ_J (nm)	$I_{c,max}$ (mA)	R_n (Ω)	V_c (mV)	j_c (10^5 A/cm^2)	$I_{c,min}$ (mA)	$I_{mod,0}$ (mA)	M (pH)	L (pH)	β_L
JJ-14						3.2	0.091	0.29	3.3					
JJ-15						3.3	0.098	0.32	3.4					
JJ-SL						3.4	0.07	0.23	3.5					
SQ-14	280	320	180	250	500	0.42	0.82	0.34	5.9	0.26	0.90	2.3	7.1	1.5
SQ-15	250	280	280	200	400	0.29	1.28	0.37	4.5	0.12	2.19	1.0	4.9	0.7
SQ-SL	280	290	300	350	400	0.20	1.68	0.34	3.0	0.12	1.24	1.7	12	1.2

a value of M inbetween. This observation is consistent with the different values for the constriction width w_c (cf. Table I and Fig. 2). We find that a narrower constriction yields a larger M. This is also supported by inductance calculations based on simulations of the supercurrrent density distribution in our nanoSQUIDs via the software 3D-MLSI, which solves the London equation in 2-dimensional current sheets[31,55,56]. A larger M is beneficial, as it relaxes requirements (maximum feedback and modulation currents) on the SQUID readout electronics for FLL operation and as it also improves the coupling between a MNP and a nanoSQUID, resulting in improved spin sensitivity.

To obtain a rough estimate of the inductance L of the nanoSQUIDs, we determine the screening parameter $\beta_L \equiv 2LI_0/\Phi_0$ from the modulation depth $\Delta I_c \equiv I_{c,max} - I_{c,min}$ of the $I_c(I_{mod})$ oscillations. Into the definition of β_L enters the noise free critical current I_0 of the JJs. In the case of negligible noise rounding, as applicable to our devices at 4.2 K (cf. Fig. 4), we can replace $2I_0$ by $I_{c,max}$. Then, by using the dependence $\Delta I_c/I_{c,max}(\beta_L)$ derived from numerical simulations for symmetric dc SQUIDs in the noise-free case, we determine β_L values as listed in Table I and which are close to the value $\beta_L \approx 1$ for optimum flux noise[57,58]. From the estimated values for β_L and the measured values for $I_{c,max}$ we then obtain the values for L as listed in Table I. For the superlattice nanoSQUIDs we obtain values of L below 10 pH. Achieving such a small inductance is important for obtaining very low values of flux noise for the nanoSQUIDs in the thermal white noise limit well below $S_\Phi^{1/2} = 1\,\mu\Phi_0/\mathrm{Hz}^{1/2}$.

We note that all $I_c(I_{mod})$ curves in Fig. 5 show a clear asymmetry. This is visible as a shift of the patterns along the I_{mod} axis in opposite direction for opposite current polarities and a skewness of the $I_c(I_{mod})$ curves, which can arise from asymmetries in the critical currents of the two JJs and from inductance asymmetry[57,58]. These observations are consistent with the slight asymmetry in the widths of the JJs, inducing a critical current asymmetry, and with the fact that the constrictions in the SQUIDs induce an inductance asymmetry.

Fig. 6 shows $V(I_{mod})$ oscillations of SQ-15, measured at different bias currents. The shift of those curves along the I_{mod} axis for opposite bias current polarity is consistent with the concomitant shift in the $I_c(I_{mod})$ pattern for SQ-15 shown in Fig. 5. Moreover, the maxima in $V(I_{mod})$ are slightly shifting along the I_{mod} axis with increasing bias current, which is consistent with a small inductance asymmetry, as discussed above. We only show here $V(I_{mod})$ oscillations for SQ-15; however, the same features are also present for SQ-14 and SQ-SL.

Finally, we discuss the flux noise of the superlattice YBCO nanoSQUIDs, which has been measured in FLL mode. Fig. 7(a) shows the rms spectral density of flux noise $S_\Phi^{1/2}(f)$ of SQ14 and SQ-15 measured with dc bias and with bias reversal at frequency $f_{br} = 20$ kHz. In the bias reversal mode, the contribution of critical current fluctuations to low-frequency excess noise is removed below f_{br}.[39] We note that we do not reach the thermal white noise regime even at the highest frequency of 100 kHz up to which we performed measurements. Hence the rms flux noise values $S_\Phi^{1/2}(100\,\mathrm{kHz}) = 244\,\mathrm{n}\Phi_0/\mathrm{Hz}^{1/2}$ for

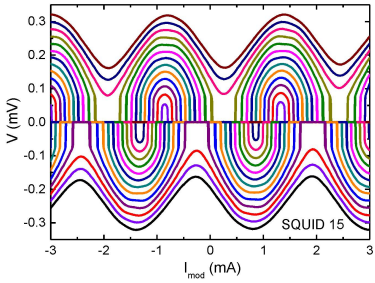

FIG. 6. Voltage-flux characteristics $V(I_{mod})$ of SQ-15 at different bias currents I_b from 133 to 360 μA in $\sim 19\,\mu$A steps (for both polarities).

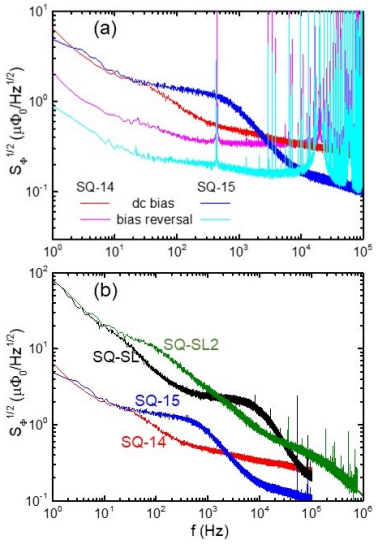

FIG. 7. Rms spectral density of flux noise $S_\Phi^{1/2}(f)$ measured in FLL mode: (a) data for SQ-14 and SQ-15, measured with dc bias and bias reversal ($f_{\rm br} = 20\,$kHz). (b) dc bias readout data of SQ-14, SQ-15, together with SQ-SL and SQ-SL2 on an expanded scale for $S_\Phi^{1/2}$ and f.

SQ-14 and $104\,{\rm n}\Phi_0/{\rm Hz}^{1/2}$ for SQ-15 (with dc bias readout) are upper bounds for the thermal white noise limit. Those are comparable to the best values for the flux noise at high frequencies obtained for YBCO nanoSQUIDs based on GBJJs in single layer devices.[32,50]

Most importantly, with dc bias readout we obtain at $f = 1\,$Hz values $S_\Phi^{1/2}(1\,{\rm Hz}) = 6.5\,\mu\Phi_0/{\rm Hz}^{1/2}$ for SQ-14 and $4.9\,\mu\Phi_0/{\rm Hz}^{1/2}$ for SQ-15. Those values are more than an order of magnitude lower than what we obtained so far for single layer YBCO nanoSQUIDs on STO bicrystal substrates[32], and they are comparable to the values for single layer YBCO nanoSQUIDs on MgO bicrystal substrates, as reported very recently.[50] To illustrate this observation, we show in 7(b) again the rms flux noise measured in dc bias mode for SQ-14 and SQ-15, now together with noise data for the single layer devices SQ-SL and SQ-SL2. The latter has also been fabricated on an STO bicrystal substrate with an Au layer on top. SQ-SL2 has been reported earlier to show the so far lowest flux noise of $\sim 45\,{\rm n}\Phi_0/{\rm Hz}^{1/2}$ in the thermal white noise limit (at very high frequency $> 7\,$MHz) for any of our YBCO nanoSQUIDs[32]. The flux noise at $f = 1\,$Hz for both single layer devices shown in Fig. 7(b) is $\sim 80\,\mu\Phi_0/{\rm Hz}^{1/2}$. This observation shows, that the use of YBCO/STO superlattices instead of YBCO single layer films can significantly reduce $1/f$ noise in YBCO nanoSQUIDs based on GBJJs.

The noise spectra for SQ-14 and SQ-15 in bias reversal mode yield a significant improvement of $S_\Phi^{1/2}(1\,{\rm Hz})$ over dc bias readout, for SQ-15 even below $1\,\mu\Phi_0/{\rm Hz}^{1/2}$ [cf. Fig. 7(a)]. This shows, that I_0 fluctutations in the GBJJ barriers are the major source of low-frequency excess noise in our devices, stemming from defects in the barriers. Hence, we conclude that the significantly reduced low-frequency excess noise in the YBCO/STO superlattice nanoSQUIDs is most likely due to an improved quality of the grain boundary, as compared to single layer YBCO nanoSQUIDs. Finally, we note that we still see low-frequency excess noise even with bias reversal readout. This issue has been addressed already in Ref. 32, where we attributed this to possible contributions from fluctuating spins in the substrate close to the STO/YBCO interface.

IV. CONCLUSIONS

We have fabricated YBCO dc nanoSQUIDs from a YBCO/STO superlattice, consisting of four 30 nm-thick individual YBCO layers, separated by 3 nm-thick STO layers. The superlattice is grown heteroepitaxially on a STO bicrystal substrate with 24° misorientation angle, and covered with 65 nm-thick Au on top, as a resistive shunt and for protection during Ga FIB milling. The characterization of crystalline film quality and measurement of the electric transport properties before and after Ga FIB nanopatterning shows that the superlattice devices have comparable quality as for single layer devices with the same total YBCO fillm thickness. Also the measured noise properties in the thermal withe noise limit are similar for single layer and superlattice devices. This is in strong constrast to the observed low-frequency excess noise: superlattice devices yield more than one order of magnitude lower noise at 1 Hz as compared to single layer devices.

Because the low-frequency excess noise is dominated by fluctuations of the critical current I_0 in the grain boundary Josephson junctions, we attribute the improved low-frequency noise performance of the superlattice nanoSQUIDs to an improved microstructure of the grain boundaries forming the Josephson junctions. However, so far we have no direct information on the microstructure at the grain boundaries in our superlattices. One possible reason for the improvement might be due to reduced facetting[28] of the grain boundaries. Certainly, a clarification of this issue, or of other possible modifications in the defect structure of the grain boundaries, that are induced by inserting STO interlayers in the YBCO films, is required in future studies.

In any case, the achieved improvement in low-frequency excess noise in YBCO nanoSQUIDs provides the opportunity to realize ultrasensitive devices for scanning SQUID microscopy and for the investigation of

magnetization reversal processes in individual magnetic nanosystems, by utilizing already achievable ultralow levels of white noise and expand those on the frequency scale down to well below the MHz range. Moreover, the superlattice approach may also be helpful to improve the low-frequency noise performance of other devices, e.g. sensitive SQUID magnetometers, that are based on grain boundaries. It remains to be shown, whether this superlattice approach could also improve the low-frequency excess noise in YBCO nanoSQUIDs based on nanowires (constriction junctions).

CONFLICTS OF INTEREST

The authors declare no conflicts of interest

ACKNOWLEDGMENTS

J. Lin acknowledges funding by the China Scholarship Council (CSC). We gratefully acknowledge fruitful discussions and technical support by M. Turad and R. Löffler (LISA$^+$) and by C. Back. This work was supported by the COST action NANOCOHYBRI (CA16218).

* koelle@uni-tuebingen.de

[1] W. Wernsdorfer, "Classical and quantum magnetization reversal studied in nanometersized particles and clusters," Adv. Chem. Phys. **118**, 99–190 (2001).

[2] M. Jamet, W. Wernsdorfer, C. Thirion, D. Mailly, V. Dupuis, P. Mélinon, and A. Pérez, "Magnetic anisotropy of a single cobalt nanocluster," Phys. Rev. Lett. **86**, 4676–4679 (2001).

[3] W. Wernsdorfer, "From micro- to nano-SQUIDs: applications to nanomagnetism," Supercond. Sci. Technol. **22**, 064013 (2009).

[4] L. Hao, C. Aßmann, J. C. Gallop, D. Cox, F. Ruede, O. Kazakova, P. Josephs-Franks, D. Drung, and Th. Schurig, "Detection of single magnetic nanobead with a nano-superconducting quantum interference device," Appl. Phys. Lett. **98**, 092504 (2011).

[5] A. Buchter, J. Nagel, D. Rüffer, F. Xue amd D. P. Weber, O. F. Kieler, T. Weimann, J. Kohlmann, A. B. Zorin, E. Russo-Averchi, R. Huber, P. Berberich, A. Fontcuberta i Morral, M. Kemmler, R. Kleiner, D. Koelle, D. Grundler, and M. Poggio, "Reversal mechanism of an individual Ni nanotube simultaneously studied by torque and SQUID magnetometry," Phys. Rev. Lett. **111**, 067202 (2013).

[6] C. Granata and A. Vettoliere, "Nano superconducting quantum interference device: A powerful tool for nanoscale investigations," Phys. Rep. **614**, 1–69 (2016).

[7] M. J. Martínez-Pérez and D. Koelle, "NanoSQUDs: Basics & recent advances," Phys. Sci. Rev. **2**, 20175001 (2017).

[8] M. J. Martínez-Pérez, B. Müller, D. Schwebius, D. Korinski, R. Kleiner, J. Sesé, and D. Koelle, "NanoSQUID magnetometry of individual cobalt nanoparticles grown by focused electron beam induced deposition," Supercond. Sci. Technol. – focus issue on NanoSQUIDs and their applications **30**, 024003 (2017).

[9] M. J. Martínez-Pérez, J. Pablo-Navarro, B. Müller, J. Stankievicz, R. Kleiner, C. Magén, D. Koelle, J. M. de Teresa, and J. Sesé, "NanoSQUID magnetometry on individual as-grown and annealed Co nanowires at variable temperature," Nano Lett. **18**, 7674–7682 (2018).

[10] M. J. Martínez-Pérez, B. Müller, J. Lin, L. A. Rodriguez, E. Snoeck, R. Kleiner, J. Sesé, and D. Koelle, "Magnetic vortex nucleation and annihilation in bi-stable ultra-small ferromagnetic particles," Nanoscale **12**, 2587–2595 (2020).

[11] J. R. Kirtley, M. B. Ketchen, K. G. Staviasz, J. Z. Sun, W. J. Gallagher, S. H. Blanton, and S. J. Wind, "High-resolution scanning SQUID microscope," Appl. Phys. Lett. **66**, 1138–1140 (1995).

[12] J. R. Kirtley, "Prospects for imaging magnetic nanoparticles using a scanning SQUID microscope," Supercond. Sci. Technol. **22**, 064008 (2009).

[13] D. Vasyukov, Y. Anahory, L. Embon, D. Halbertal, J. Cuppens, L. Ne'eman, A. Finkler, Y. Segev, Y. Myasoedov, M. L. Rappaport, M. E. Huber, and E. Zeldov, "A scanning superconducting quantum interference device with single electron spin sensitivity," Nature Nanotechnol. **8**, 639–644 (2013).

[14] D. Koelle, "Magnetic sensors: A tip for better sensing," Nature Nanotechnology **8**, 617–618 (2013).

[15] D. Hazra, J. R. Kirtley, and K. Hasselbach, "Nano-superconducting quantum interference devices with continuous read out at millikelvin temperatures," Appl. Phys. Lett. **103**, 093109 (2013).

[16] J. R. Kirtley, L. Paulius, A. J. Rosenberg, J. C. Palmstrom, C. M. Holland, E. M. Spanton, D. Schiessl, C. L. Jermain, J. Gibbons, Y.-K.-K. Fung, M. E. Huber, D. C. Ralph, M. B. Ketchen, G. W. Gibson Jr., and K. A. Moler, "Scanning SQUID susceptometers with sub-micron spatial resolution," Rev. Sci. Instr. **87**, 093702 (2016).

[17] P. Reith, X. R. Wang, and H. Hilgenkamp, "Analysing magnetism using scanning SQUID microscopy," Rev. Sci. Instr. **88**, 123706 (2017).

[18] M. Wyss, S. Gliga, D. Vasyukov, L. Ceccarelli, G. Romagnoli, J. Cui, A. Kleibert, R. L. Stamps, and M. Poggio, "Stray-field imaging of a chiral artificial spin ice during magnetization reversal," ACS Nano **13**, 13910–13916 (2019).

[19] Y. Anahory, H. R. Naren, E. O. Lachman, S. Buhbut Sinai, A. Uri, L. Embon, E. Yaakobi, Y. Myasoedov, M. E. Huber, R. Klajn, and E. Zeldov, "SQUID-on-tip with single-electron spin sensitivity for high-field and ultra-low temperature nanomagnetic imaging," Nanoscale **12**, 3174–3182 (2020).

[20] A. Uri, Y. Kim, K. Bagani, C. K. Lewandowski, S. Grover, N. Auerbach, E. O. Lachman, Y. Myasoedov, T. Taniguchi,

K. Watanabe, J. Smet, and E. Zeldov, "Nanoscale imaging of equilibrium quantum Hall edge currents and of the magnetic monopole response in graphene," Nature Phys. **16**, 164–170 (2020).

[21] R. Wölbing, J. Nagel, T. Schwarz, O. Kieler, T. Weimann, J. Kohlmann, A. B. Zorin, M. Kemmler, R. Kleiner, and D. Koelle, "Nb nano superconducting quantum interference devices with high spin sensitivity for operation in magnetic fields up to 0.5 T," Appl Phys. Lett. **102**, 192601 (2013).

[22] R. Arpaia, M. Arzeo, S. Nawaz, S. Charpentier, F. Lombardi, and T. Bauch, "Ultra low noise $YBa_2Cu_3O_{7-\delta}$ nano superconducting quantum interference devices implementing nanowires," App. Phys. Lett. **104**, 072603 (2014).

[23] R. Arpaia, M. Arzeo, R. Baghdadi, E. Trabaldo, F. Lombardi, and T. Bauch, "Improved noise performance of ultrathin YBCO Dayem bridge nanoSQUIDs," Supercond. Sci. Technol. **30**, 014008 (2017).

[24] S. A. Cybart, E. Y. Cho, J. T. Wong, B. H. Wehlin, M. K. Ma, C. Huynh, and R. C. Dynes, "Nano Josephson superconducting tunnel junctions in $YBa_2Cu_3O_{7-\delta}$ directly patterned with a focused helium ion beam," Nat. Nano **10**, 598–602 (2015).

[25] E. Y. Cho, Y. W. Zhou, J. Y. Cho, and S. A. Cybart, "Superconducting nano Josephson junctions patterned with a focused helium ion beam," Appl. Phys. Lett. **113**, 022604 (2018).

[26] H. Li, H. Cai, E. Y. Cho, S. J. McCoy, Y.-T. Wang, J. C. LeFebvre, Y. W. Zhou, and S. A. Cybarte, "High-transition-temperature nanoscale superconducting quantum interference devices directly written with a focused helium ion beam," Appl. Phys. Lett. **116**, 070601 (2020).

[27] B. Müller, M. Karrer, F. Limberger, M. Becker, B. Schröppel, C. J. Burkhardt, R. Kleiner, E. Goldobin, and D. Koelle, "Josephson junctions and SQUIDs created by focused helium-ion-beam irradiation of $YBa_2Cu_3O_7$," Phys. Rev. Appl. **11**, 044082 (2019).

[28] H. Hilgenkamp and J. Mannhart, "Grain boundaries in high-T_c superconductors," Rev. Mod. Phys. **74**, 485 (2002).

[29] J. Nagel, K. B. Konovalenko, M. Kemmler, M. Turad, R. Werner, E. Kleisz, S. Menzel, R. Klingeler, B. Büchner, R. Kleiner, and D. Koelle, "Resistively shunted $YBa_2Cu_3O_7$ grain boundary junctions and low-noise SQUIDs patterned by a focused ion beam down to 80 nm linewidth," Supercond. Sci. Technol. **24**, 015015 (2011).

[30] T. Schwarz, J. Nagel, R. Wölbing, M. Kemmler, R. Kleiner, and D. Koelle, "Low-noise nano superconducting quantum interference device operating in tesla magnetic fields," ACS Nano **7**, 844–850 (2013).

[31] R. Wölbing, T. Schwarz, B. Müller, J. Nagel, M. Kemmler, R. Kleiner, and D. Koelle, "Optimizing the spin sensitivity of grain boundary junction nanoSQUIDs – towards detection of small spin systems with single-spin resolution," Supercond. Sci. Technol. **27**, 125007 (2014).

[32] T. Schwarz, R. Wölbing, C. F. Reiche, B. Müller, M. J. Martínez-Pérez, T. Mühl, B. Büchner, R. Kleiner, and D. Koelle, "Low-noise $YBa_2Cu_3O_7$ nano-SQUIDs for performing magnetization-reversal measurements on magnetic nanoparticles," Phys. Rev. Appl. **3**, 044011 (2015).

[33] D. Koelle, R. Kleiner, F. Ludwig, E. Dantsker, and John Clarke, "High-transition-temperature superconducting quantum interference devices," Rev. Mod. Phys. **71**, 631–686 (1999).

[34] C. T. Rogers and R. A. Buhrman, "Composition of $1/f$ noise in metal-insulator-metal tunnel junctions," Phys. Rev. Lett. **53**, 1272–1275 (1984).

[35] V. Foglietti, W. J. Gallagher, M. B. Ketchen, A. W. Kleinsasser, R. H. Koch, S. I. Raider, and R. L. Sandstrom, "Low-frequency noise in low 1/f noise dc SQUIDs," Appl. Phys. Lett. **49**, 1393–1395 (1986).

[36] B. Savo, F. C. Wellstood, and J. Clarke, "Low-frequency excess noise in Nb-Al_2O_3-Nb Josephson tunnel junctions," Appl. Phys. Lett. **50**, 1757–1759 (1987).

[37] A. Marx and R. Gross, "Scaling behavior of $1/f$ noise in high-temperature superconductor Josephson junctions," Appl. Phys. Lett. **70**, 120 (1997).

[38] R. H. Koch, J. Clarke, W. M. Goubau, J. M. Martinis, C. M. Pegrum, and D. J. Van Harlingen, "Flicker $(1/f)$ noise in tunnel junction dc SQUIDs," J. Low Temp. Phys. **51**, 207–224 (1983).

[39] D. Drung and M. Mück, "SQUID Electronics," in *The SQUD Handbook*, Vol. I: Fundamentals and Technology of SQUIDs and SQUID Systems, edited by John Clarke and Alex I. Braginski (Wiley-VCH, Weinheim, 2004) Chap. 4, pp. 127–170.

[40] F. Ludwig, D. Koelle, E. Dantsker, D.T. Nemeth, A.H. Miklich, J. Clarke, and R.E. Thomson, "Low noise $YBa_2Cu_3O_{7-x}$-$SrTiO_3$-$YBa_2Cu_3O_{7-x}$ multilayers for improved magnetometers," Appl. Phys. Lett. **66**, 373–375 (1995).

[41] M. I. Faley, S. B. Mi, A. Petraru, C. L. Jia, U. Poppe, and K. Urban, "Multilayer buffer for high-temperature superconductor devices on MgO," Appl. Phys. Lett. **89**, 082507 (2006).

[42] M. I. Faley, J. Dammers, Y. V. Maslennikov, J. F. Schneiderman, D. Winkler, V. P. Koshelets, N. J. Shah, and R. E. Dunin-Borkowski, "High-T_c SQUID biomagnetometers," Supercond. Sci. Technol. **30**, 083001 (2017).

[43] J.-M. Triscone and O. Fischer, "Superlattices of high-temperature superconductors: Synthetically modulated structures, critical temperatures and vortex dynamics," Rep. Prog. Phys. **60**, 1673–1721 (1997).

[44] R. Gross, A. Gupta, E. Olsson, A. Segmüller, and G. Koren, "Critical current density of strained multilayer thin films of $Nd_{1.83}Ce_{0.17}CuO_x$/$YBa_2Cu_3O_{7-\delta}$," Appl. Phys. Lett. **57**, 203–205 (1990).

[45] S. R. Foltyn, H. Wang, L. Civale, Q. X. Jia, P. N. Arendt, B. Maiorov, Y. Li, M. P. Maley, and J. L. MacManus-Driscoll, "Overcoming the barrier to 1000 A/cm width superconducting coatings," Appl. Phys. Lett. **87**, 162505 (2005).

[46] A. V. Pan, S. Pysarenko, and S. X. Dou, "Drastic improvement of surface structure and current-carrying ability in $YBa_2Cu_3O_7$ films by introducing multilayered structure," Appl. Phys. Lett. **88**, 232506 (2006).

[47] S. R. Foltyn, L. Civale, J. L. MacManus-Driscoll, Q. X. Jia, B. Maiorov, H. Wang, and M. Maley, "Materials science challenges for high-temperature superconducting wire," Nature Mater. **6**, 631–642 (2007).

[48] R. Werner, C. Raisch, A. Ruosi, B. A. Davidson, P. Nagel, M. Merz, S. Schuppler, M. Glaser, J. Fujii, T. Chassé, R. Kleiner, and D. Koelle, "$YBa_2Cu_3O_7$/$La_{0.7}Ca_{0.3}MnO_3$ bilayers: Interface coupling and electric transport properties," Phys. Rev. B **82**, 224509 (2010).

[49] S. Scharinger, M. Turad, A. Stöhr, V. Leca, E. Goldobin, R. G. Mints, D. Koelle, and R. Kleiner, "Magnetic field dependence of the critical current in $YBa_2Cu_3O_{7-\delta}$/Au/Nb

ramp-zigzag Josephson junctions," Phys. Rev. B **86**, 144531 (2012).

[50] J. Lin, B. Müller, J. Linek, M. Karrer, M. Wenzel, M. J. Martínez-Pérez, R. Kleiner, and D. Koelle, "$YBa_2Cu_3O_7$ nano superconducting quantum interference devices on MgO bicrystal substrates," Nanoscale **12**, 5658–5668 (2020).

[51] J. D. Jorgensen, B. W. Veal, A. P. Paulikas, L. J. Nowicki, G. W. Crabtree, H. Claus, and W. K. Kwok, "Structural properties of oxygen-deficient $YBa_2Cu_3O{-}7-\delta$," Phys. Rev. B **41**, 1863–1877 (1990).

[52] W. C. Stewart, "Current-voltage characteristics of Josephson junctions," Appl. Phys. Lett. **12**, 277–280 (1968).

[53] D. E. McCumber, "Effect of ac impedance of dc voltage-current characteristics of Josephson junctions," J. Appl. Phys. **39**, 3113–3118 (1968).

[54] L. Ryen, E. Olsson, C. N. L. Edvardsson, and U. Helmersson, "Dislocations, strain, and defects in heteroepitaxial $YBa_2Cu_3O_{7-x}/SrTiO_3$ multilayers," Physica C **304**, 307–313 (1998).

[55] M. M. Khapaev, M. Y. Kupriyanov, E. Goldobin, and M. Siegel, "Current distribution simulation for superconducting multi-layered structures," Supercond. Sci. Technol. **16**, 24–27 (2003).

[56] J. Nagel, O. F. Kieler, T. Weimann, R. Wölbing, J. Kohlmann, A. B. Zorin, R. Kleiner, D. Koelle, and M. Kemmler, "Superconducting quantum interference devices with submicron Nb/HfTi/Nb junctions for investigation of small magnetic particles," Appl. Phys. Lett. **99**, 032506 (2011).

[57] C. D. Tesche and J. Clarke, "DC SQUID: Noise and optimization," J. Low Temp. Phys. **29**, 301–331 (1977).

[58] B. Chesca, R. Kleiner, and D. Koelle, "SQUID Theory," in *The SQUD Handbook*, Vol. I: Fundamentals and Technology of SQUIDs and SQUID systems, edited by John Clarke and Alex I. Braginski (Wiley-VCH, Weinheim, 2004) Chap. 2, pp. 29–92.